Condition Monitoring of Press-Pack IGBT Modules for High Voltage DC Transmission using Temperature Sensitive Mechanical Parameter

Bowen Gu

B.Sc., M.Sc.

A thesis submitted for the degree

of Doctor of Philosophy

July 2022

School of Engineering

Newcastle University

United Kingdom

Abstract

Power electronics is a technology that can efficiently transmit energy to the user, with power semiconductor devices playing a pivotal role as a key component in power conversion. The trend in power semiconductor devices is towards higher power ratings and higher power densities which all lead to higher heat generation inside the device.

High thermal stress generated during the operation results in failing power semiconductor devices. Insulated Gate Bipolar Transistors (IGBTs) are the most widely used power electronic switches for medium and high power conversion applications. IGBTs are mostly packaged using bond wires. Bond-wired IGBT modules for high power levels, however, do have reliability issues and often fail open circuit. In High Voltage DC Transmissions (HVDC) power modules that fail open must be avoided. For that reason, in HVDC press pack IGBT (PP IGBT) modules are used which are known to fail short-circuit. Although PP IGBTs reduce the risk of module failures by allowing electrical and thermal contact within the module through pressure, instead of through bonding wires they fail eventually over time.

Monitoring the health condition of PP IGBT modules is therefore essential and the aim of this work is to develop an on-line measurement technique that can provide an early warning of degrading PP IGBT modules for HVDC applications. This thesis compares different existing online health monitoring techniques and identifies where within a press-pack to monitor the health of the module. A new parameter, the collector groove lid deformation, is identified. The relationship between junction temperatures and deformation is shown. The new technique is called Temperature Sensitive Mechanical Parameter (TSMP) in analogy to the well-known Temperature Sensitive Electrical Parameter (TSEP).

Sensors suitable for measuring deformation are analyzed and compared, and an FBG-based (Fiber Bragg Grating) online monitoring system is proposed, which can monitor multiple series-connected PP IGBT modules in real time through a single optical fibre and can also determine the location of faulty modules and the approximate distribution of chips based on deformation variation. Experimental work is carried out on different

PP IGBT modules, and different test requirements are considered by modifying the internal structure of the modules. Practical and simulation work are presented and discussed to verify the effectiveness of the proposed health monitoring system for PP IGBTs.

Acknowledgement

The project requires the help of many individuals. I would like to express my sincere and foremost gratitude to my supervisor, Prof. Volker Pickert, for his guidance, encouragement and support. What I learned from him was not only the ability to solve technical problems but also the logical way of thinking. I also deeply thank to Dr. Haimeng Wu for his help, advice throughout the duration of the project. It was a valuable memory. Many thanks to Dr. Mohamed Dahidah, Dr. Bing Ji, Dr. Zhiqing Wang and Dr. Siyang Dai for providing help in the project. Their broad knowledge has been of great value for me.

I would like to thank the technical staff within the department. Special thanks to Gordon Marshall and James Richardson, for their help with the construction of the experiment setup and the assembly of the electronic hardware. They guaranteed a safe and smooth experimental process throughout the project. Many thanks to my colleagues and academic researchers in the School of Engineering for their considerable support during my work.

My heartfelt appreciation goes towards my parents, Feng Gu and Zhilan Wang, for their support and encouragement during my study. I would also like to express my uttermost thanks to my girlfriend, Mingzhu Cheng, for her love and company from my study to my life. Many thanks to my valuable friends in Newcastle University, Xiang Wang, Qing Li, Handong Li, Zhengyu Zhao, Hao Chen, Ruosen Qi, Bortecene and Ramin, their help and friendship we had I will never forget. At last, I would like to thank the additional support from industrial partner, Littelfuse-IXYS UK, for their kind donations of semiconductor and other components for the tests.

List of Figures

List of tables

List of abbreviations

ALSIC	Aluminum Silicon Carbide
CM	Condition Monitoring
CTE	Coefficient of Thermal Expansion
DCB	Direct Copper Bonded
EMI	Electromagnetic Interference
ESPI	Electronic Speckle Pattern Interferometry
FBG	Fibre Bragg Grating
FPI	Fabry Perot Interferometer
GF	Gauge Factor
HVAC	High Voltage Alternating Current
HVDC	High Voltage Direct Current
IGBT	Insulated Gate Bipolar Transistor
LCI	Low Coherence Interferometry
MOSFET	Metal-Oxide-Semiconductor Field-Effect transistor
MVD	Medium Voltage Drive
PDMS	Polydimethylsiloxane Elastomeric Structures
PETT	Plasma Extraction Transit Time
PP IGBT	Press Pack Insulated Gate Bipolar Transistor
RTD	Resistance Temperature Detector

SAM	Scanning Acoustic Microscope
SAWR	Surface Acoustic Wave Resonator
TSEP	Temperature Sensitive Electrical Parameter
TSMP	Temperature Sensitive Mechanical Parameter

List of symbols

dic/dt	Collector Current Changing Rate
Vce	Collector Emitter Voltage
$V_{GE\text{-}th}$	Gate-Emitter Threshold Voltage
t_{off}	Turn-Off Time
V_{on}	On-State Voltage
$V_{f\text{-}Ict}$	Forward Voltage under Low Current
q	Heat Flux
ρ	Material Density
C_p	Specific Heat Capacity
k	Thermal conductivity
q_c	Convection
h	Film Coefficient
E	Young's Modulus
σ	Stress
ε	Strain/Deformation
n_{eff}	Effective Refractive Index
Λ	Periodicity of Grating
λ_B	Bragg Central Wavelength
ρ_e	Photo-Elastic Coefficient

Contents

Chapter 1 Introduction

1.1 Background

Transporting electric energy over a large distance presents a challenge as high voltage AC (HVAC) transmission lines become too lossy over a long distance [1]. To deal with the losses, high voltage DC (HVDC) transmission lines can be installed [2]. Several HVDC lines have been installed worldwide. For example, in the UK an HVDC line connects the city of Hunterston in Scotland with Flintshire in Wales. The total cable length is around 422km, and it transmits 2,200MW of power at a DC voltage of 600KV [3][4]. The longest HVDC transmission line in the world is in China, with an operational DC voltage of 1,100KV and a length of 3,293km from Changji to Guquan. This line can transmit 12GW of electricity [5].

In order to achieve these high voltages, semiconductor devices are required to convert AC voltages to DC voltages and vice versa. There are two types of converter topologies: multi-level converters and standard converters. The structure of multi-level converters requires the use of several bond-wired power modules. Bond-wired power modules can handle a maximum voltage of 6.5kV. The FZ500R65KE3 power module from Infineon, for example, can operate at this voltage level [6]. By adding and controlling these power modules in specific sequences, different voltage levels can be achieved. There are commonly three multi-level converter types: diode clamped, capacitor clamped and cascade converters. Multi-level converters have the advantages of producing low output voltage distortion, reducing electromagnetic interference (EMI) and drawing input currents with low distortion [7].

The main disadvantage of multi-level converters, however, is their use of bond-wired power modules that tend to create an open circuit in the case of a power failure [8]. In many applications power modules that fail open are seen as a benefit, as this decouples the input from the output. For example, if a device such as a home battery charger fails open circuit, it electrically disconnects the high voltage AC supply from the low battery voltage. In terms of supplying a large amount of energy to suburbs, towns and industrial areas, an open circuit results in a blackout. In order to avoid this, press-pack semiconductors are used. They do not have bond wires, and in the case of a failure, they fail by short circuit [9]. Press-pack semiconductors are not commonly used in multi-level

converters. They are used in a string arrangement, meaning that many press-pack semiconductors are connected in series to gain the maximum HVDC. This requires that all the devices be turned on and off simultaneously.

1.2 PP IGBT application

The press-pack insulated gate bipolar transistor (PP IGBT) concept was first proposed by the Fuji Electric Corporation of Japan in 1993 [10], and since then, PP IGBTs have been continuously improved. PP IGBTs offer various advantages, such as low thermal resistance, double-sided heat dissipation, short-circuit failure and high current rating capabilities, making them ideal for HVDC transmission [10][11]. At present, PP IGBTs are mainly manufactured by companies including Littelfuse-IXYS UK, ABB, Fuji Electric, Dynex and Toshiba. PP IGBT devices are constructed by connecting multiple IGBT chips and multiple diode chips in parallel. Due to the relative ease of scaling these devices, PP IGBTs have experienced a rapid growth in market share [12].

1.2.1 Medium voltage drive

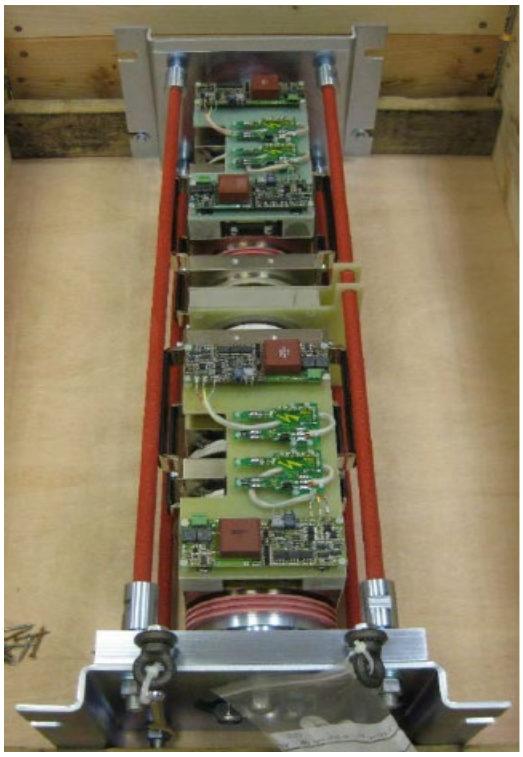

Figure 1.1 Medium voltage drives for marine application using PP IGBT [13]

Medium voltage drives (MVD) (sometimes called variable frequency drives) are variable speed drives that control the torque and speed of AC motors. In such drives, voltage in the range of 2,300V to 4,160V is considered medium voltage [14].

PP IGBTs are ideal components for medium voltage converters since they offer higher power potential and thermal cycling capability [15]. Medium voltage drives using PP IGBTs can be found in steel mills, pumps, marine applications and wind generation. Figure 1.1 shows a variable frequency marine drive using PP IGBTs [16].

1.2.2 Pulsed power application

Pulsed power is a niche market that started in the 1960s [17]. Originally, pulsed power generators were used for nuclear fission and military applications. Pulsed power produces a very high peak power output in a short burst. This burst can be repeated depending on the application. Today, pulsed generators are employed in a wide range of industrial applications. PP IGBTs have been used in a great number of pulsed generators due to their ideal performance and high-power ability. For example, pulsed generators using PP IGBTs can be found in medical, water treatment, food processing and exhaust gas treatment applications [18]. Figure 1.2 shows a 5-terminal pulsed power switch application using PP IGBTs.

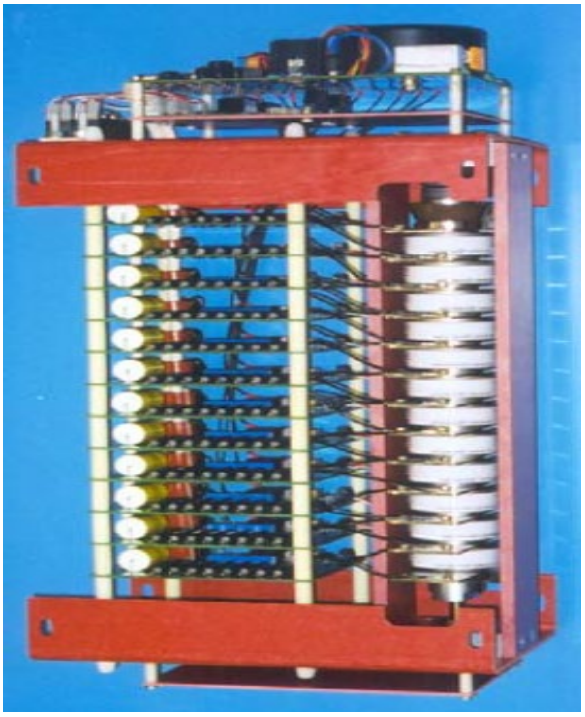

Figure 1.2 5-terminal pulsed power switch application using PP IGBTs [13]

1.2.3 HVDC

The early introduction of the AC transformer, which allows for longer distance and low-loss high voltage AC transmission, has historically made HVAC the dominant transmission technique [19].

However, HVDC systems, which outperform HVAC systems in terms of long distance transmission, are becoming increasingly essential for energy transmission. The use of HVDC transmission started in the 1960s when thyristor valves became more widely available.

As a result, fifty to forty years ago, HVDC transmission lines were thyristor-based. The development of the IGBT in the 1980s paved the way for further HVDC market innovation in the late 1990s [20][21][22] since IGBT has the advantages of low driving voltage, high blocking voltage range and low saturation voltage, the normal frequency range of IGBT is from 1k to 500k and the voltage can up to 6500V. With the development of PP IGBT technology, it was now possible to turn the device on and off with much greater control capability and a reduction in voltage and current distortions [23]. Figure 1.3 shows the basic schematic of an HVDC converter using PP IGBTs.

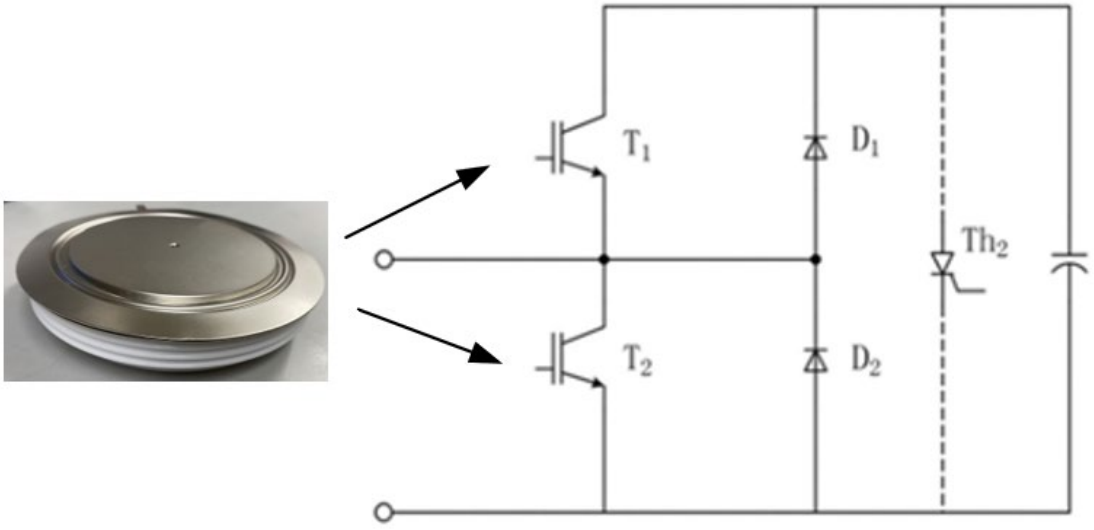

Figure 1.3 HVDC converter station using PP IGBTs [24]

1.3 Failure modes of PP IGBTs

As PP IGBTs become more widely used, their reliability is of particular concern in certain applications, such as marine applications, in which maintenance costs are high and access is limited. Due to the internal layout of the module, the temperature deviation of the chips and contact pressure differences lead to an unbalanced current distribution for each IGBT chip, resulting in reliability issues. Therefore, an understanding of the failure modes of PP IGBT modules is critical.

Several studies in the literature list failure modes of PP IGBT modules. For example, [25] reports a failure due to fretting friction and the metallization of the molybdenum plate, caused by a mismatch in the coefficient of thermal expansion (CTE) of the molybdenum plate and the silicon chip. [26] highlights gate oxide breakdown and the re-metallization of IGBT chips as failure modes. Another proposed failure mode involves the cracking of the chip surface caused by overvoltage between the collector and the emitter [27]. Collector lid warpage failure caused by the thermal gradient in the lid is reported in [28]. The detailed failure modes summary is shown in section 2.3.2.

Each of these failure modes poses a challenge for the reliable operation of PP IGBTs. It is therefore essential to monitor the condition of PP IGBTs. The work presented in this thesis focuses on the online condition monitoring (CM) of PP IGBTs.

1.4 Motivation

As different failure modes cause reliability issues in PP IGBTs, CM methods must be applied. CM is the process of monitoring a device parameter that is linked with the degradation and failure of the device.

Not many CM techniques have been applied to PP IGBTs, in part due to their compact structure, which limits the ability to add sensors inside the package, but also because PP IGBTs are multi-chip devices. In such devices, it is challenging to distinguish which of the chips or areas has failed or is going to fail. In [29], the plasma-extraction transit-time (PETT) method was applied to detect chip temperature, the oscillation voltage, frequency and duration were different based on different chip temperature. Temperature sensitive electric parameter (TSEP) methods have also been applied to detect failing modules, such as monitoring dic/dt [30] and Vce(T) [31], this kind of TESPs is related to junction temperature, however, the average temperature within each module were obtained not the

junction temperature of each chip. In [32], the sequential Vce(T) method was proposed for the measurement of junction temperature distribution with a separated gate controller.

All of the methods proposed thus far either require a bespoke additional circuit for each PP IGBT or are suitable for offline detection only. In HVDC applications hundreds of PP IGBTs are connected in series. Adding a circuit for each PP IGBT becomes expensive and increases complexity, therefore adding to reliability issues.

Therefore, it is necessary to develop an online CM method for PP IGBTs that is reliable, easy to implement, scalable and low in cost. This thesis introduces such a method is making use by detecting deformations at specific locations on the PP IGBT. The measured deformation is shown to be linked to temperature rise, which in turn is linked to degradation within the PP IGBT. As such, the proposed technique operates similarly to TSEP methods, in which temperature rise is seen as an indicator of a failing power module. However, the proposed method collects information not from an electrical parameter but from a mechanical parameter and is therefore called a temperature sensitive mechanical parameter (TSMP) method.

1.5 Aims and objectives

The main aim of this research is to monitor the health condition of PP IGBTs.

The specific objectives of this research are as follows:

- to evaluate existing CM techniques applied to classical bond-wire modules
- to assess existing CM techniques applied to press packs
- to build a high-fidelity PP IGBT model for use in FE simulations using ANSYS
- to investigate the effect of thermo-mechanical coupling on PP IGBT conditions
- to explore the relationship between deformation on the collector lid groove and the temperature of PP IGBTs
- to determine the area of faulty chips by examining the different degree of deformation on the lid groove
- to find suitable techniques that measure the deformation of press-pack lids
- to determine the relationship between lid deformation and the temperature profile produced by IGBT chips

- to build and test a lab-scaled prototype using the selected new technique and to demonstrate the operation principle
- to collect experimental results to validate simulated results

1.6 Contribution to knowledge

Based on the knowledge gathered, the research makes following contributions:

- proposes a new indicator called the temperature sensitive mechanical parameter (TSMP) to monitor the health condition of PP IGBTs
- demonstrates the relationship between the new indicator and the faulty chip area
- shows a clear relation between press-pack lid deformation and chip temperature
- applies the fibre Bragg grating (FBG) technique to press packs for the first time to measure the deformation of the lid as a TSMP
- constructs and tests a bespoke testing prototype with integrated FBG sensors and an interrogator able to conduct operations at different chip temperature profiles
- establishes an early warning system for failing PP IGBTs connected in series that identifies the location of failing module and failing IGBT chips

1.7 Thesis structure

The organization and contents of the thesis are briefly described here.

Chapter 1: The focus of this chapter is to explain the research as a whole and to detail the objectives and methodology of the thesis.

Chapter 2: This chapter presents the literature review in four sections. The first section briefly covers the requirements for and importance of CM. The second part focuses on reviewing the failure modes and CM technology for conventional IGBT modules. The chapter then reviews the failure modes and CM methods for PP IGBT modules. The last part is a chapter summary.

Chapter 3: This chapter presents a detailed FE simulation of a PP IGBT module. By building different models and varying model parameters, an investigation of the relationship between the deformation and health of a PP IGBT module is carried out.

Chapter 4: In this chapter deformation detection methods for micro-range deformations are discussed. By comparing the pros and cons of each sensor, a suitable method that can be applied to PP IGBTs is determined.

Chapter 5: This chapter describes the application of FBG sensors to a press-pack stack, introduces the setup for the test rig and shows the test results for a single PP IGBT. It also presents the test results for the application of FBG sensors to two PP IGBTs connected in series and demonstrates the detection of faulty modules. Finally, the results with water cooling effect are shown as the basis for the early warning system.

Chapter 6: A summary of the research is provided in this chapter along with recommendations, conclusions and a discussion of possible future research.

1.8 Publications

Publications related to the research:

B, Gu, Wu, H., Pickert, V., Dai, S., Wang, Z., Li, G., Ding, S. and Ji, B. "Condition monitoring of press-pack IGBT devices using Deformation Detection Approach," 2020 IET Power Electronics, Machines and Drives Conference (PEMD), December 2020, online conference, p355-360.

B, Gu, Wu, H., Pickert, V., Ji, B, Dai, S. and Wang, Z. "Deformation analysis of Press-pack IGBT using thermal mechanical coupling method, " International Joint Conference on Energy, Electrical and Power Engineering CoEEPE 2021, online conference, vol 899. Springer, Singapore.

Journal paper to be submitted.

Other publications:

H. Wu, B. Gu, X. Wang, V. Pickert and B. Ji, "Design and control of a bidirectional wireless charging system using GaN devices," 2019 IEEE Applied Power Electronics Conference and Exposition (APEC), 2019, pp. 864-869, doi: 10.1109/APEC.2019.8721909.

H. Wu, X. Wang, B. Gu and V. Pickert, "Investigation of a GaN-based Bidirectional Wireless Power Converter using resonant inductive coupling," 2019 IEEE Wireless Power Transfer Conference (WPTC), 2019, pp. 263-268, doi: 10.1109/WPTC45513.2019.9055539.

X. Deng, H. Wu, B. Gu, G. Atkinson, B. Mecrow and V. Pickert, "Present and Future of Fault Tolerant Drives Applied to Transport Applications," CIPS 2020; 11th International Conference on Integrated Power Electronics Systems, 2020, pp. 1-8.

Chapter 2 Literature Review

2.1 Introduction

Condition monitoring (CM) is the process or technique used to monitor the operational characteristics of a device by detecting changes in parameters and trends that can be used to predict maintenance needs before a severe failure [33]. CM can be applied to a variety of components, including transformers [34][35] and electric machines [25][36] but also semiconductor power devices [37][38][39]. Although engineers have made extensive efforts to improve the reliability of semiconductor power devices, some industry surveys show that when power electronic equipment fails, the power semiconductor devices are still the most fragile components. A survey presented in [40] shows that IGBT power modules are the most used power semiconductor devices in the converters, at 42% [40].

Many CM technologies have been applied to power modules over the past ten years. However, the main challenges are an insufficient relationship between the detected parameter and failures within multi-chip power modules.

Most published papers on CM for power modules describe the use of thermal models to determine the junction temperature of the chip. This is because most degradations in power modules cause an increase in junction temperature. Although this project focuses on detecting the health condition of PP IGBT modules, the failure modes and detection methods of traditional packaged IGBT modules must be understood first.

2.2 Overview of condition monitoring methods for conventional power modules

2.2.1 Structure of conventional IGBT power modules

The first bond wired IGBT power modules appeared in 1980 [41][42]. Due to continuous technological advancement, significant innovations have been made in both materials and packaging structures, allowing for the current widespread use of IGBT power modules. Interestingly, due to changes in both packaging and materials over the years, failure mechanisms and failure modes have also changed.

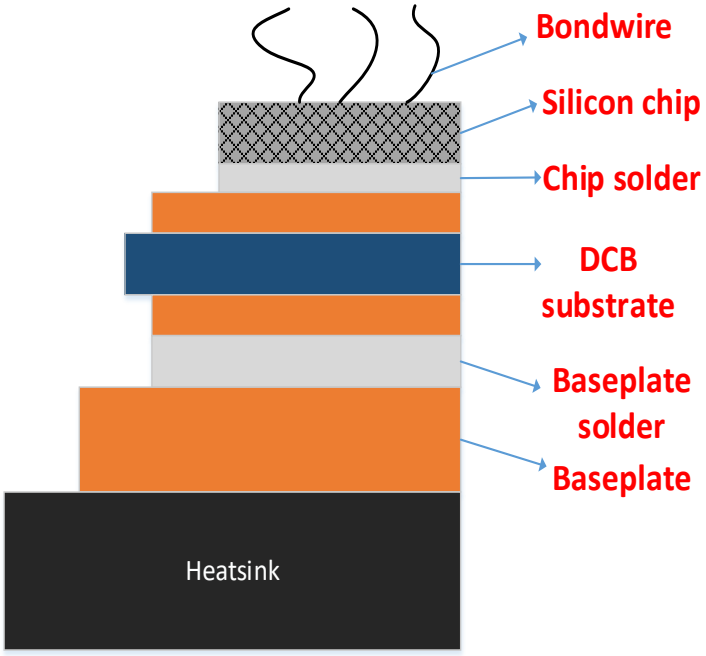

Figure 2.1 Schematic of conventional IGBT module

The typical structure of a bond wire IGBT is shown in Figure 2.1. The Figure shows that bond wires are placed on top of the silicon chip to electrically connect the chip to the direct copper bonded (DCB) or terminal connection points. The bottom side of the chip is soldered to the DCB substrate; the DCB is a copper–ceramic–copper sandwich that has good electrical insulation and good thermal conductivity. The DCB is soldered to the baseplate, which is made mainly from copper or aluminium silicon carbide (AL Sic). The bottom of the baseplate is mounted to the heatsink. A layer of thermal paste is used in between the two to increase heat flux conductivity.

IGBT power modules have a housing made mostly of plastic. Silicone gel is injected inside the module for the mechanical protection of the bond wires and electrical isolation of the DCB copper tracks. Figure 2.2 provides a cross-section view of a typical bond wire IGBT module [43].

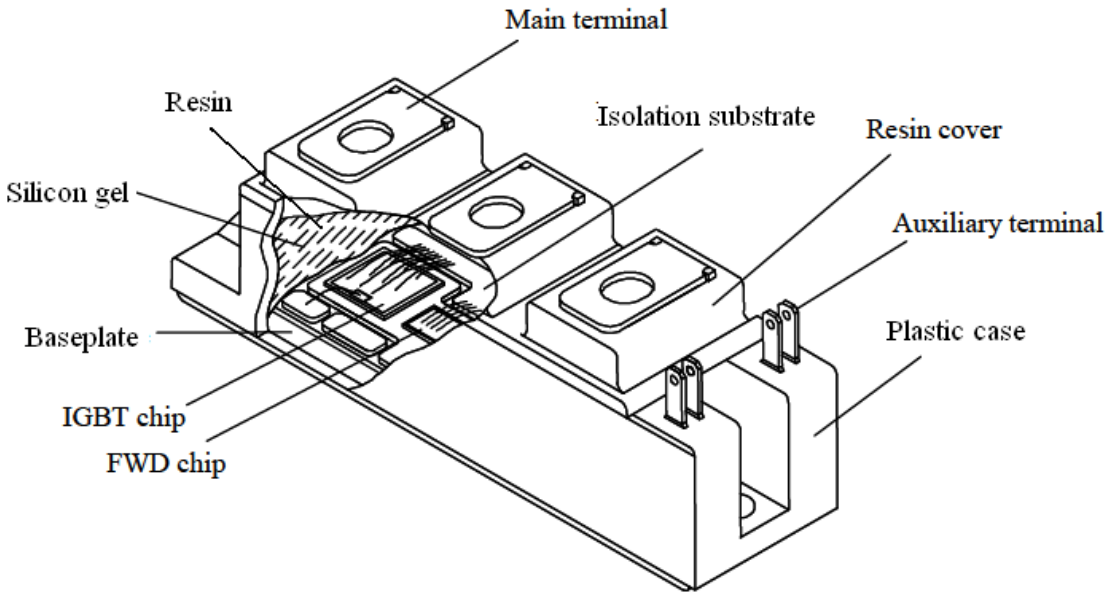

Figure 2.2 Cross-section view of a conventional IGBT module [43]

There are many advantages using this packaging, such as low cost, mature technology, and easy assembly. However, the traditional IGBT module packaging has some shortcomings like the mismatch in the coefficient of thermal expansion (CTE) between the different materials for example. This is leading to mechanical stress at the boundaries of each material. Cracks in the solder and bond wire lift-offs are some of the fatigue appearances caused by thermal stress [44].

2.2.2 Condition monitoring method for conventional IGBT modules

The reliability of power IGBT modules has long been a hot topic of research in the field of power electronics. Many failure mechanisms and failure modes have been reported. Failures can be random and sudden or progress slowly due to wear-out. Failure mechanisms can include conditions such as temperature, current and voltage, humidity, and mechanical vibration [45][46]. These mechanisms normally lead to wear-out. Cosmic rays, on the other hand, are a known mechanism for sudden failure, and CM techniques are unable to detect this type of event. This study focuses on wear-out failure modes because they can be monitored by CM. The wear-out failure modes of conventional IGBT modules are summarized in Table 2-1; these are divided into chip-related failures and package-related failures.

Table 2-1 Failure modes summary of conventional IGBT modules

Components	Driving force
Chips	Gate oxides break down Chip fracture or crack. [47][8][48][49]
	Secondary break-down, Time dependent dielectric break-down [50][51][52]
Package	Bond wire fatigue [53][54]
	Chip reconstruction [55]
	Solder joint cracks [56]

Three different methods can be used to monitor wear-out failures in IGBT devices in order to obtain their operational conditions and in-service usage: 1) the use of expandable devices such as the fuse which is the hardware redundancy method; 2) the model-driven method; and 3) the data-driven method also known as signal-based method [57]. The hardware redundancy method uses a precognition unit that provides warning signals for the IGBT chip-related failure mechanism [58].

The precognition unit is made by scaling down the design so that it experiences the same operating conditions as the chip but fails faster, thus providing an early warning of the actual chip failure. The model-driven method, also known as the life prognosis method, is used to determine the health of an IGBT module by collecting specific data from the module online for input into a damage model and then determining how much damage has occurred [59]. The data-driven approach aims to determine the health condition of the IGBT module from statistics based on the module's historical data by collecting online important parameters that can identify performance degradation to indicate impending failures [60].

Amongst these methods, data-driven methods are the most commonly used to monitor the wear-out of IGBT modules. The prognostic cell method is rarely reported on in relation to power module (IGBT, MOSFET) applications, and this method does not

indicate package related faults [61].

Moreover, although model-driven methods can calculate IGBT module life consumption online, the failure models built are mostly empirical models based on experimental results that are often inaccurate. It is also difficult to build failure models that are applicable to multiple failure modes due to the complexity of the failure process of IGBT modules [62]. By contrast, a large amount of literature has been reported on the use of data-driven methods to monitor conventional IGBT modules, which can provide a good reference for the CM of PP IGBT modules. Thus, this section mainly reviews the data-driven methods.

There are two common techniques to capture data in data-driven methods. The first technique is to capture a voltage or current parameter that is associated with the internal condition of the IGBT module. For example, by tracing collector current and gate source voltage, gate oxide degradation can be detected. Another approach involves linking the junction temperature with the voltage and current values measured at the module terminals.

The junction temperature is a preferred parameter, as it is a good indicator of the health condition of the power modules. For example, the on-state voltage of the IGBT chip has a linear relation with the junction temperature of the chip. Electric parameters that have a relationship to the junction temperature are called temperature sensitive electrical parameters (TSEPs).

TSEP methods are the most widely researched methods for determining the health condition of a device [63][64]. In order to measure these parameters, additional circuitry is required to measure the parameters in a safe and efficient way. The second technique for collecting data involves adding sensors either internally within the power module or externally. For example, the bond wire lift-off can be observed by measuring strain gauges to detect the mechanical stress within an IGBT module.

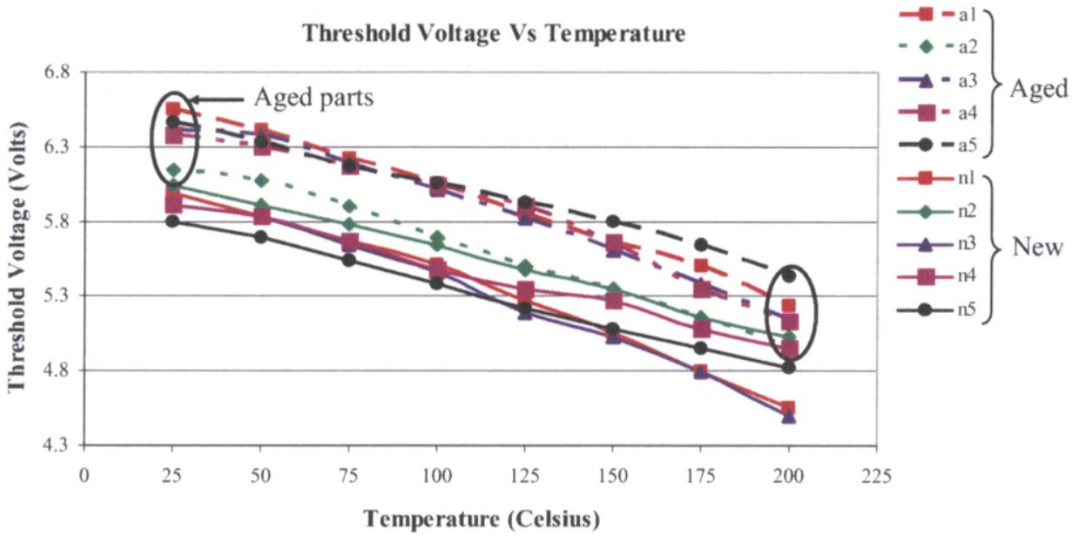

Figure 2.3 Relationship between junction temperature and threshold voltage [65]

Thus, there are different detection methods available to identify different failure modes. Notably, some of these can only be conducted in the laboratory, such as those that use a strain gauge, whereas others can be used for in-field operations, such as TSEP methods. The following section provides a few examples of data-driven methods.

Gate oxide breakdown can be determined by measuring the gate-emitter threshold voltage $V_{GE\text{-}th}$ and collector current [66][67]. $V_{GE\text{-}th}$ is the lowest gate voltage that allows IGBTs to turn on and the collector current to flow. The relationship between the threshold voltage and the junction temperature under different gate oxidations was determined in [65], while Figure 2.3 shows the observed threshold voltage among devices of aged and new has a negative coefficient with junction temperature. This was because the bandgap of the silicon decreases with the increase of the temperature, which means the higher temperature leads to easier conduction of IGBT [65].

The leakage current is defined as the current flowing through the collector when the gate is short-circuited, and a rated voltage is applied to the collector and the emitter. In [68] it was concluded that the leakage current and the junction temperature show an exponential relationship, in which the leakage current rises sharply after the temperature reaches a certain value (Figure 2.4). Thus, one TSEP involves measuring the leakage current to determine the junction temperature.

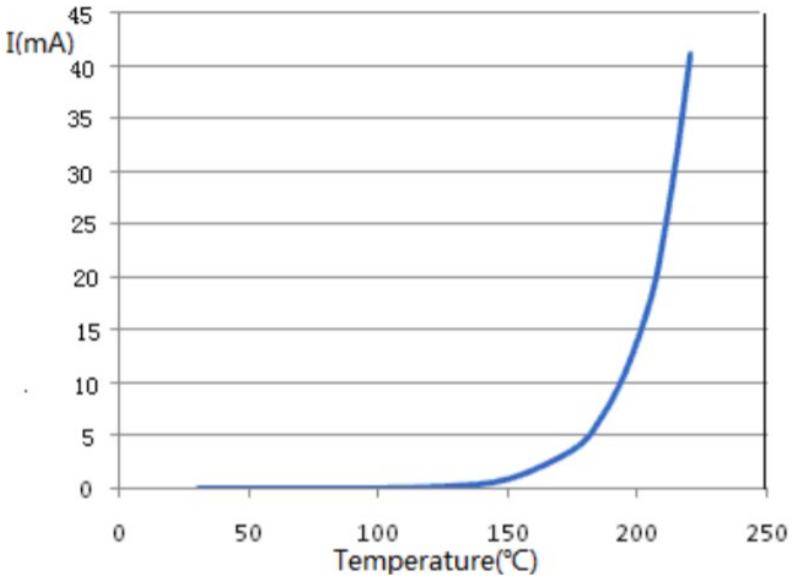

Figure 2.4 Relationship between leakage current and junction temperature [68]

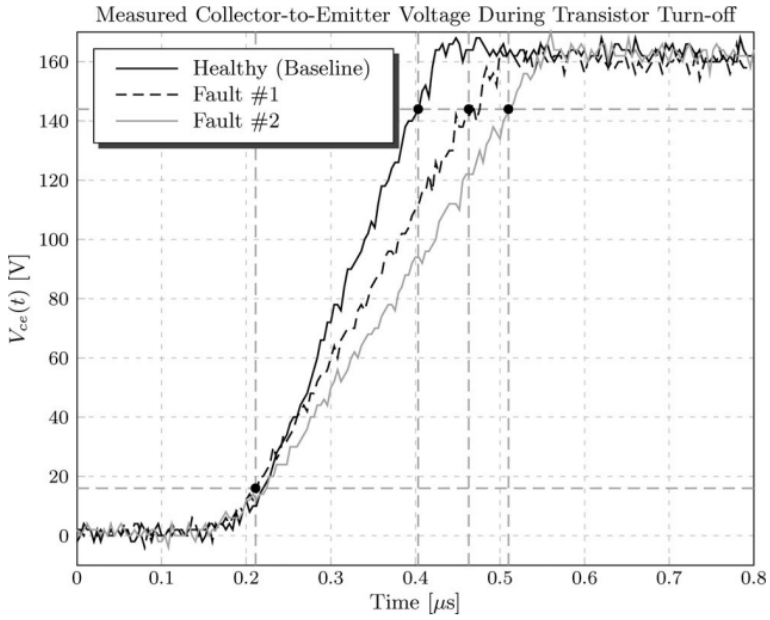

Figure 2.5 Relationship between turn-off time and health condition of the chip [69]

A detection method for latch-up failure was investigated in [69], this failure mode is caused by the activation of the parasitic thyristor within IGBT structure when continue on-state current breach a certain value. The study recorded the voltage turn-off time t_{off} comparison between different latch-up scenarios and healthy module, as shown in Figure 2.5, as the device gradually fails, the turn-off time increases accordingly. Another study investigated the use of on-state voltage V_{CE} as a TSEP, this is used off-line when IGBT is not in use [70]. By plotting the constant small collector currents in (mA range) versus on-state voltage, the impact of junction temperature change can be

observed, the relationship between the on-state collector-emitter voltage drop and junction temperature is negative, as seen in Figure 2.6.

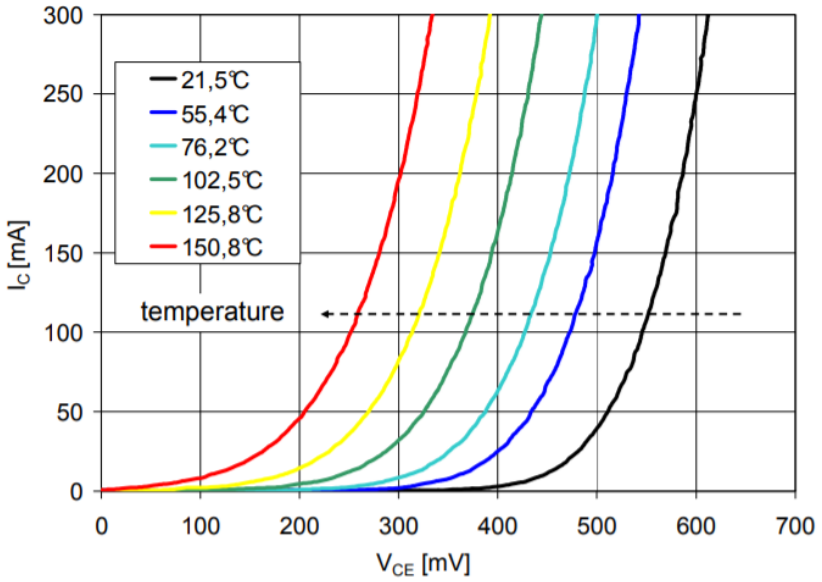

Figure 2.6 Relationship between on-state voltage and small collector current [70]

Bond wire lift-off can be detected via externally embedded sensors. For example, in [71], an integrated detection resistor and a sub-circuit were added to determine the state of the device, allowing bond wire lift-off to be observed in a single chip structure and a parallel connected IGBT module. In [72], another sensing technology was applied to detect the bond wire lift-off. In this method, a resister is connected in parallel with the emitter bonding wire, and the resistance voltage drop is used to diagnose the bond wire status in the module.

For detecting solder joint cracks, [71] proposed using a scanning acoustic microscope (SAM) image to record the condition of the solder joint as well as the DCB solder layer. The SAM uses ultrasonic sound waves to measure the surface of the object, and when cracks occur, the reflected waves produce a different frequency signature compared to the frequencies when there are no cracks.

Resistance temperature detectors (RTDs) were used in [73] and compared with the TSEP method. The RTDs were soldered on the four edges of the chip, while for TSEP the forward voltage under low current ($V_{f\text{-}Ict}$) was used. Figure. 2.7 shows the difference between the two methods. In this particular case the two techniques show a surprisingly good overlap.

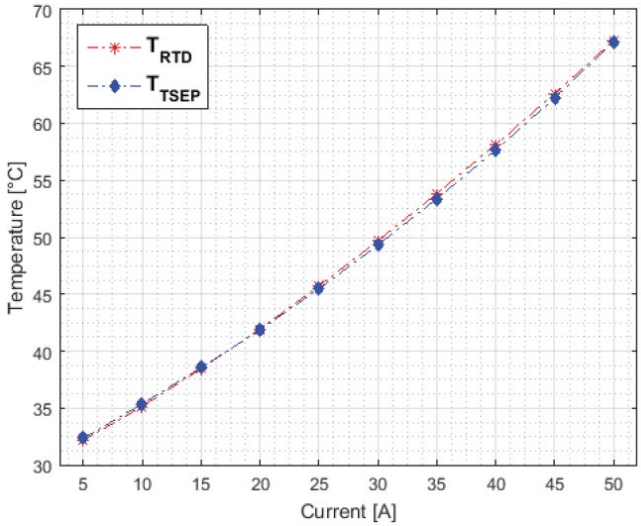

Figure 2.7 Comparison between TSEP method and RTD embedded sensor method [73]

2.3 Condition monitoring for PP IGBT modules

2.3.1 Press-pack IGBT module structures

The most fundamental difference between a PP IGBT module and a traditional IGBT module is the lack of bond-wires in PP IGBT modules. To provide electrical contact between the chip and terminals the IGBT chip is effectively mechanically clamped between two plates [74].

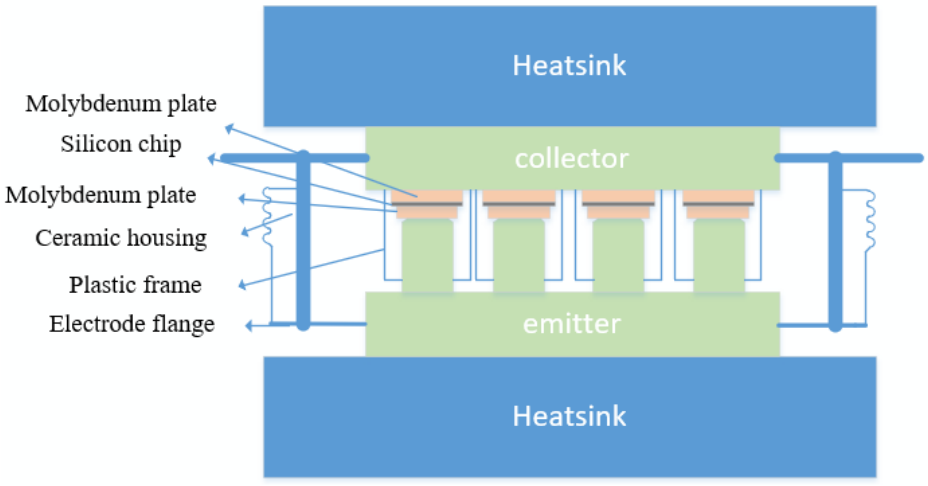

Figure 2.8 Classic press pack structure

Press-pack technology was first introduced to power semiconductor devices, including diodes, GTOs and other thyristors; before the advent of high power IGBTs, only these three power electronic devices were available for high power applications. Later, with

their increasing power capabilities, IGBTs found their way into PP IGBTs [28].

The classic PP IGBT structure, shown in Figure 2.8 [26], comprises five layers: two molybdenum plates, two metal lids and a die in the middle. Each side of the die connects to a metal lid via a molybdenum plate in order to supply thermal and electrical contact. The metal lid is made of copper with a thin layer of nickel on the surface on both sides. The lid provides electrical contact, heat transfer and pressure. The molybdenum plates on both sides of the die provide pressure balance due to their CTE value that is similar to that of the silicon chip. The CTE values of these materials are listed in Table 2-2. The gate distribution board is connected to the die through a spring-loaded pin, and the entire construction is placed in a ceramic capsule [27]. The ceramic capsule provides a hermetic seal and strong protection for the module.

Table 2-2 CTE value of PP IGBT modules

Material	Silicon	Molybdenum	copper
CTE (1/°C)	4.8^-6	4.9^-6	1.71^-5

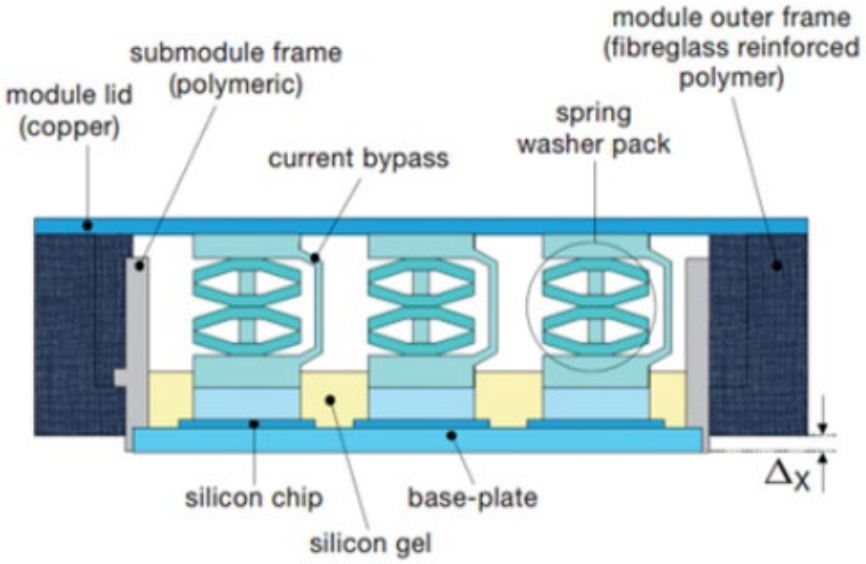

Figure 2.9 View of ABB PP IGBT with spring contacts [75]

An alternative PP IGBT structure called StakPak (protected trademark of ABB) is shown in Figure 2.9. The use of disc springs permits the incorporation of a mechanism that limits the force on individual chips to a predetermined value [75]. An important feature of this mechanical construction is that the sensitivity to non-uniform pressure distribution is greatly reduced [76].

There are several obvious advantages to press-pack technology compared with classic packaging. First, PP IGBTs are much more power dense compared to solder-based packaging. This is because the clamping of the chip not only provides good electrical contact but also good thermal contact. Second, bond wire failing modes do not exist, and therefore PP IGBTs have higher a reliability compared to classical power modules. Third, the chip is cooled on both sides, reducing thermal stress [77]. Fourth, the current distribution within a PP IGBT is more homogenous compared to its counterpart. Finally, PP IGBT power modules can be easily connected in series, so that in the case of a failure they short circuit, giving them an advantage in applications such as HVDC transmissions [9].

2.3.2 Condition monitoring method for PP IGBT modules

Similar to the traditional IGBT module, it is necessary to understand the failure mechanism and failure mode of the PP IGBTs before introducing CM techniques. The failure mechanisms and failure modes of PP IGBTs are different compared to traditional modules due not only to differences in structure but also to the pressure variable that is introduced into the PP IGBT. As with traditionally packaged IGBT modules, the failure mode of press packs can be differentiated at the chip level and the packaged level.

As summarized in [26], there are several possible failure modes for PP IGBTs, which at the chip level are similar to traditional IGBT modules, such as gate oxide breakdown and re-metallization of the chip. However, the causes of these failures are different. For example, in PP IGBTs the gate oxide breaks down mostly due to non-uniform pressure distribution. Re-metallization of the chip occurs through the application of a clamping force that is either too large or too small, too large clamping force may cause the chip crack and too small force may leading the high thermal resistance between the die and the heatsink, then both of these may leading the high temperature occurs in the die level causing the metal contact window on the die melting and re-metallized.

Another failure mechanism at the chip level is chip fracture or cracking or sliding wear on the surface [27]. This failure is caused by an overvoltage drop between the collector and emitter and local short circuits within the module. Figure 2.10 shows a failed IGBT chip with sliding wear on the surface.

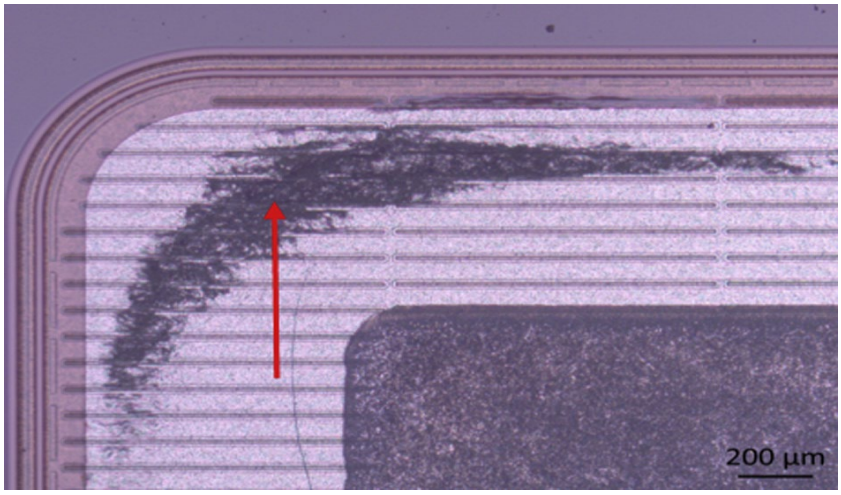

Figure 2.10 Sliding wear surface of the IGBT chip [13]

Figure 2.11 Failed Mo plate and IGBT chips [13]

Failure modes unique to PP IGBT modules include failures associated with the molybdenum plates. For example, [25] proposed that the fretting friction and metallization of the Mo plate is caused by a CTE mismatch between the Mo plate and silicon chip. The difference in CTE not only causes mechanical stress but also increases the thermal contact resistance between the Mo plate and the silicon chip. Figure 2.11 shows a failed IGBT chip and metallization of the Mo plate.

In terms of the failure modes at the PP IGBT package level, [28] reports collector electrode warpage failures caused by the thermal gradient in the lid leading to lateral expansion. Figure 2.12 illustrates collector lid warpage. Collector lid groove expansion was reported in [52], caused by over clamping, over temperature and short circuiting.

Table 2-3 summarizes the current failure modes, failure mechanisms and their causes

for PP IGBT modules. Comparing these failure modes with those of conventional IGBT modules, the main differences are the failure of molybdenum plates and failures at the module level.

Table 2-3 Failure modes and failure mechanisms of PP IGBT modules

Components	Driving force	Causes
Chips	Gate oxides break down	Non-uniform pressure distribution [59]
	Chip fracture or crack. Deformation	Over current Short circuit High switching frequency Over voltage drop Mismatch in CTE Thermal contact resistance increases Over clamping force Less clamping force Mechanical damage [59][70][64][61]
	Metallization of chip. Chip fracture or crack. Deformation. Ablation between chip and Mo plate	
Mo plates	Deformation. Metallization of Mo plate and Si chip. Sliding wear of the surface. Ablation between Mo plate and silver shim	Short circuit Mismatch in CTE Thermal contact resistance increases Over clamping force Less clamping force Mechanical damage [61][66][67]
Package	Collector electrode warpage Collector lid groove expand	Thermal gradient in the lid with lateral expansion Over clamping force Less clamping force Chip crack or burnout Hermetic seal infringement [59]

Figure 2.12 Collector electrode warpage [13]

A limited number of studies on CM methods for PP IGBT modules can be found in the literature. Most of the research on CM of PP IGBTs has focused on changes in internal physical variables affected by external forces, such as mechanical and thermal stress. To understand these changes, physical models are often designed and simulated using finite element analysis.

For example, [58] developed a 3D finite element model (FEM) PP IGBT model to numerically simulate the mechanical clamping conditions of the static thermal distribution of IGBT chips. In [59], a Computational Fluid Dynamics (CFD) simulation was carried out, focusing on the coolant channel design for the PP IGBT heatsink to minimize temperature propagation. Another study investigated the influence of clamping force on electrical contact resistance and thermal contact resistance [60]. To validate simulation results, various tests have been conducted. Power cycling tests have revealed two possible failure modes: damage to the gate oxide and micro erosion between the die and the molybdenum plate [61]. Yet another study investigated the influence of the pressure between the chip layer and the molybdenum plate, where very high mechanical pressure can result in mechanical damage to the chip, but mechanical pressure that is too low can cause a sudden rise in the chip junction temperature [62]. Overall, the clamping force is one of the most important parameters affecting the reliability of PP IGBTs, and this phenomenon has been studied widely [63][64][65][66][67].

All of the above studies used physical models to determine CM methods. CM

techniques that do not rely on the use of models have been described in [71], which applied the plasma-extraction transit-time (PETT) method to detect the junction temperature. It was found that the junction temperature is not the only factor affecting the oscillation of PETT, as the different signals interact with each other and are complex to identify. In addition, the module structure needs to be changed to achieve control of the PETT output within the EMC range. TSEP methods were studied using dic/dt [72] and Vce(T) [73][74]; however, as with classical multi-chip power modules, only the virtual average temperature can be determined, making it more difficult to identify the failure of a single chip. One study proposes the sequential Vce(T) method for the measurement of junction temperature distribution using a separated gate controller [75]. This method can obtain the junction temperature distribution inside the PP IGBT module by measuring the individual chip in different cycles. However, this method requires a new module layout to reconstruct the gate board, and the junction temperature can only be measured offline.

2.4 Summary

In summary, the most popular CM methods for classical bond wired power modules are TSEP methods. These work well for single-chip devices. In multi-chip devices, TSEPs not work well, as one measured electrical parameter represents all chips. Thus, clearly identifiable degradation is difficult to detect. This also applies to PP IGBTs, leaving the use of embedded sensors as the only valuable CM method for PP IGBTs. However, implanting sensors to determine temperature is not practical due to limited internal space.

Chapter 3 FE simulation of PP IGBT modules

The previous Chapter listed the various failure modes that can occur within press packs. As with standard bonded power modules, the IGBT temperature rises in a failing press pack. Any increase in temperature leads to internal mechanical pressure within the power module, which ultimately results in mechanical stress and deformation. It is therefore important to understand where stress and deformation takes place in a PPIGBT module. This Chapter presents simulation results for two different press-pack modules.

The first PP IGBT investigated is the IXYS T0800EB45G (Littelfuse-IXYS UK) with a rated collector–emitter voltage of 4,500V and collector current of 800A. The second PP IGBT is the Toshiba ST2000GXH32, which has a rated collector-emitter voltage of 4,500V and collector current of 2,000A. Simulation results for the second PP IGBT modules are shown in Appendix A. A cross-sectional image of the Toshiba module is shown in Figure 3.1, illustrating the collector lid, emitter lid, ceramic housing, internal pillar and upper and lower molybdenum plates. Figure 3.1 does not show components such as the gate spring pins and the resin-frame, which can be ignored due to the frame's low temperature dependencies.

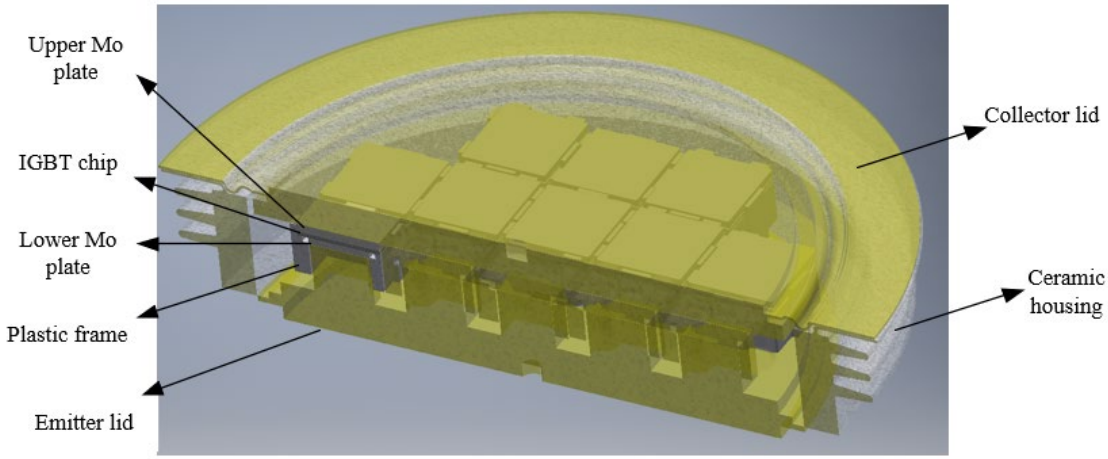

Figure 3.1 Cross-section schematic of the IXYS PP IGBT

3.1 Simulation of deformation using ANSYS software

In this project, the finite element (FE) method was used for simulation analysis. This method involves dividing the continuous object of analysis into finite parts using an imaginary grid, and then combining the parts to reform the whole. In the FE analysis

method, an approximate function is used to express grid displacement, and the relationship between an external influence and the displacement of each node is established through physical principles and laws or other analytical methods. The research described in this thesis used ANSYS as the FE analysis software. The advantages of ANSYS include its powerful functions, convenient operation and friendly interface, especially for multi-physics coupling simulations, making it suitable for PP IGBT multi-physics coupling analysis.

In practical applications, the current temperature and stress are coupled together inside the PP IGBT. Therefore, the core of the coupled simulation should be modelling both solid heat transfer and solid mechanics. Modelling both solid heat transfer and solid mechanics will provide the thermal expansions and contractions of each FE piece, resulting in the observation of expansions and contractions for the entire component. Thus, the displacements and deformations at any point within the PP IGBT can be observed.

In order to observe deformation, the power loss of the chips must be calculated based on the device data sheet and chip size. Inputting calculated power loss to the chips results in heat, which results in deformation. Another factor that adds to deformation is the clamping force. The clamping force depends on the application and is often dictated by the semiconductor manufacturer. ANSYS uses both input parameters to calculate thermomechanical performance within the PP IGBT.

It must be noted that due to the complexity of the PP IGBT, the model takes into account the CTEs of the different materials, the individual thermal time constants that are driven by the material properties and dimensions of those materials, the local mechanical stress interaction between the different materials, and the appearance of local frictions resulting in tiny gaps that change the local thermal impedance. Poor contact between layers of different materials leads to an increase in thermal resistance, which leads to the additional accumulation of heat and the further uneven distribution of expansion and deformation.

In the simulation, the physical principles and laws used internally to calculate the deformation are described in the following equation. The temperature calculation is derived from the power loss of the chip and the cooling capacity of the heat sink. Equations (3.1) and (3.2) explains the relationship between the temperature and power

loss. The deformation is then calculated by (3.4). These parameters are set in the material properties mentioned previously.

As shown in (3.1) and (3.2), where ρ is the density, $C_p$is the specific heat capacity, $k$is the thermal conductivity, and q is the heat flux, $T$is temperature function with position x and time t. The temperature is the crucial parameter in the physical model since it affects the mechanical and electrical performance.

$$\frac{\partial}{\partial t}T(x,t) - \alpha \Delta T(x,t) = \frac{q}{C_p \rho} \tag{3.1}$$

$$\alpha = \frac{k}{C_p \rho} \tag{3.2}$$

Despite describing the internal heat flux, thermal convection must be considered to reflect the cooling with the ambient temperature. Based on (3.3) convection q_c is defined by the film coefficient h, the surface area A, and the difference between surface temperature $T_{surface}$ and ambient temperature $T_{ambient}$.

$$q_c = hA\left(T_{surface} - T_{ambient}\right) \tag{3.3}$$

To analysis the mechanical deformation (3.4) is used that describes the principle of the strain generation. E is Young's Modulus, $\sigma$is stress and $\varepsilon$is strain.

$$\sigma = E\varepsilon \; \varepsilon = \alpha \Delta T \tag{3.4}$$

3.2 FE model setup

For the FE simulation the static thermal and structure platform provided by ANSYS was used, with the friction model applied to address surface roughness between the different materials.

Figure 3.2 shows the 3D model with a multi-zone mesh, which provides a balance between accuracy of results and computation speed. In the simulation, all elements of the PP IGBT were stacked layers of materials that showed a uniform, isotropic and elastoplastic mechanical response and followed isotropic flow rules.

To analyse the relationship between deformation and the static strain of the thermal and mechanical stress, the thermal heat generated by the power consumption of the semiconductor chips and the pressure exerted by the external fixture were used as the two key variables. In this work, the simulation included several restraints. The device was assumed to operate in a normally-on state, and the average current injected into the

chip was used as the source of thermal strain. At the same time, a convective heat transfer coefficient was set between the outside of the device and the heat sink. The outer edge of the heat sink was maintained at room temperature. In addition, the pressure applied by the external clamping fixture was set on the top of the collector heatsink and kept uniform, while a fixed support was set on the bottom of the emitter heatsink.

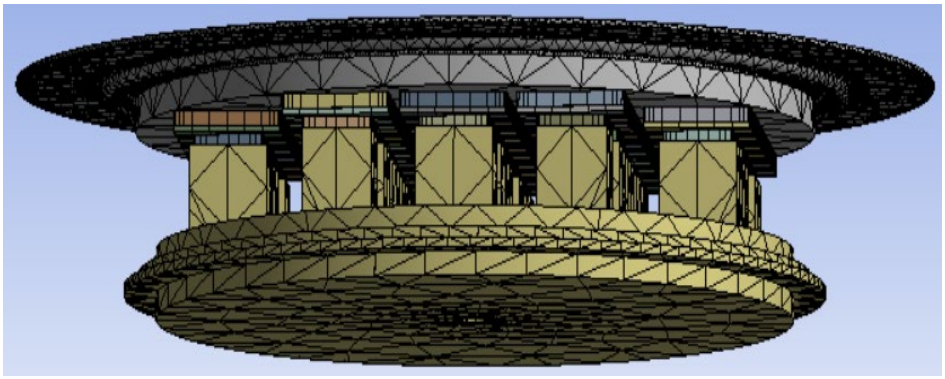

Figure 3.2 3D finite element (FE) model of a PP IGBT with a multi-zone mesh

3.2.1 Geometry data for PP IGBT

In order to create an FE module and to simulate it as discussed in the previous sections two data sets are requires: geometry of the model and material data. Pressure, current distribution, and performance of electric, thermal and deformation are all related, so it is essential to have an accurate geometric model and the correct material data.

Table 3-1 Material and dimensions of the components inside the module

Component	Thickness (mm)	Surface area (mm^2)
Si chip	0.5	201.2
Collector Mo plate	0.51	210.25
Emitter Mo plate	0.55	96
Pillar	6.5	90.25
Collector pole	6.7	5675
Emitter pole	6.7	5675

Table 3-1 shows the dimensions of the main components inside the PP IGBT module. Detailed schematic diagram of the PP IGBT module is presented in Figure 3.3, the diameter of the whole collector lid is 124mm and the diameter of the projection on the lid in contact with the heat sink is 85.1mm and the height of the collector groove is around 0.8 mm. These data provide the information for selecting the suitable sensors in the later use.

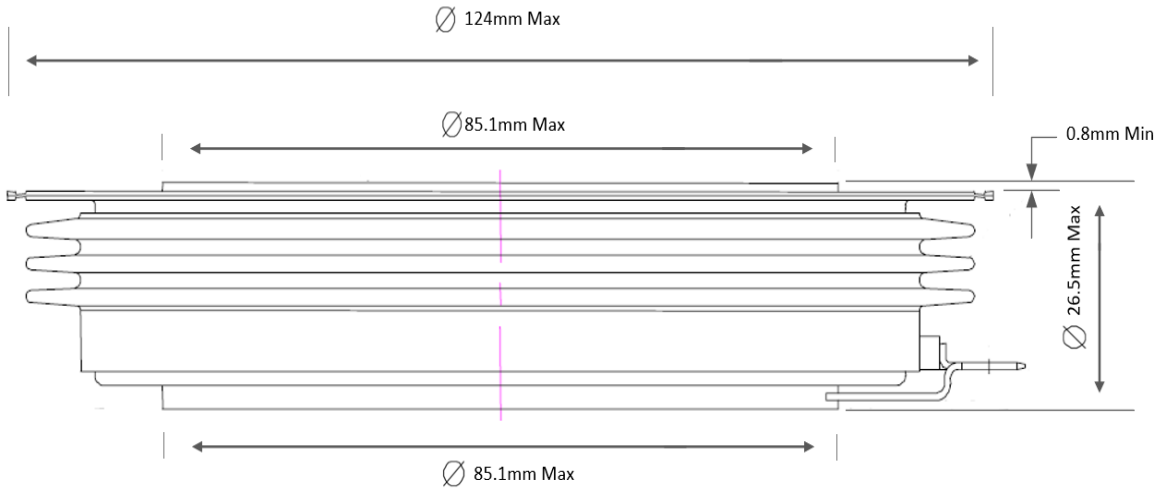

Figure 3.3 Detailed schematic diagram of PP IGBT module

3.2.2 Material data for PP IGBT

Despite designing an accurate geometrical model, material data must be exact too for FE simulation. Thermal and mechanical parameters have been entered into the model and Table 3-2 shows all relevant information for the FE analysis. The data shown were either given by Littelfuse-IXYS UK, found in the literature or were available from the library of ANSYS.

It is worse noting that thermal conductivity of silicon is relatively small when operating between 20℃-125℃. Also, for aluminium and copper, the thermal conductivity can be considered as constant when operating between -50℃ to+150℃. Therefore, in this thesis the thermal and mechanical parameters remain unchanged during the simulation. Based on the above equations, pre-set material properties and the actual size of the geometry model, ANSYS is able to calculate deformation at any point within the PP IGBT.

Table 3-2 Material properties used for the FE model

Material	Young's module (GPa)	Poisson's ratio	Material density (kg/m^3)	Coefficient of thermal conductivity [W/(m*K)]	Coefficient of thermal expansion α (1/°C)
Silicon	162	0.23	2330	148	4.8E-6
Molybdenum	320	0.28	10220	130	4.9E-06
Copper	129	0.34	8933	385	1.71E-05

3.3 FE simulation using evenly distributed IGBT power

Figure 3.4 shows the basic simulation procedure. The 3D geometry of the PP IGBT model was developed in Inventor using all information about the geometry and material data. The 3D model was then transferred to the ANSYS platform. The heatsink block was built using Designer in ANSYS and attached to the PP IGBT model. Once all the information had been inputted, the thermal simulation was conducted through a static thermal analysis in ANSYS. The results of this step were transferred to the ANSYS static structure to simulate the mechanical parameters of such a deformation.

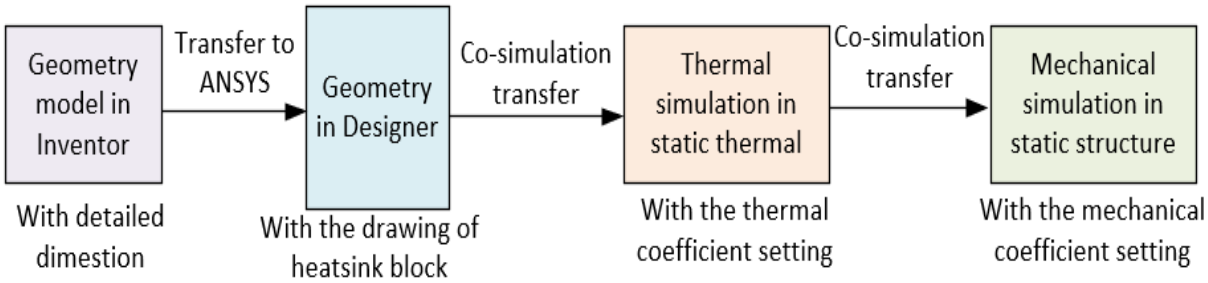

Figure 3.4 Simulation flowchart of modelling and thermal and mechanical analysis

The procedures illustrated in the flowchart in Figure 3.4 were able to detect deformation based on heat stress and mechanical clamp pressure. The module structure and material properties remained unchanged during the simulation.

In the first simulation, it was assumed that all IGBTs in the press pack produced the same power. Adding sensors to PP IGBTs is difficult; the only accessible points for adding sensors are the module's lids and ceramic housing of a PP IGBT module. Strictly speaking, the ceramic housing of a PP IGBT is mechanically decoupled from wear-out failures. As such, studying the ceramic housing would not be beneficial. The two lids, however, are thermo-mechanically coupled. The lid is normally flat with a small cone in the centre and a groove which appears close to the end of the lid. This groove is common in PP IGBTs, as it acts as a spring when pressing the lid into the ceramic housing.

As the groove acts like a spring, it was therefore predicted that the groove itself would be exposed to deformation. Assuming a constant total heat power of 1.6kW (1/4 max power dissipation), Figure 3.5(a) shows the simulation results of the deformation in the collector lid. As all the IGBTs grew hotter, the temperature produced heat that led to the expansion of the lid. As seen in Figure 3.5(a), the maximum deformation occurred in the inner lining of the groove. A maximum deformation of 56.58µm was recorded at one point on the inner lining. This can be compared with the lowest deformation of 39.43µm, which appeared at the outer ring of the lid. Figure 3.5(a) shows that the groove in the lid was the only part of the module that showed consistent stress and therefore deformed along the entire length of the groove.

Therefore, this work focused on detecting the deformation of the lid groove as a function of IGBT heat loss and mechanical clamp pressure. The results demonstrated that the deformation of the groove is a good indictor to detect overheated IGBT chips. Because of the ease of detection and the fact that the deformation of the lid groove changed with the alteration of the junction temperature of the chips, this new parameter was chosen as a health conditioning indicator for PP IGBT modules and is referred to as a TSMP. Most publications have ignored the deformation of the collector lid groove, with most studies treating the lid as a solid unit in simulations. Figure 3.5(b) shows a close-up of the groove.

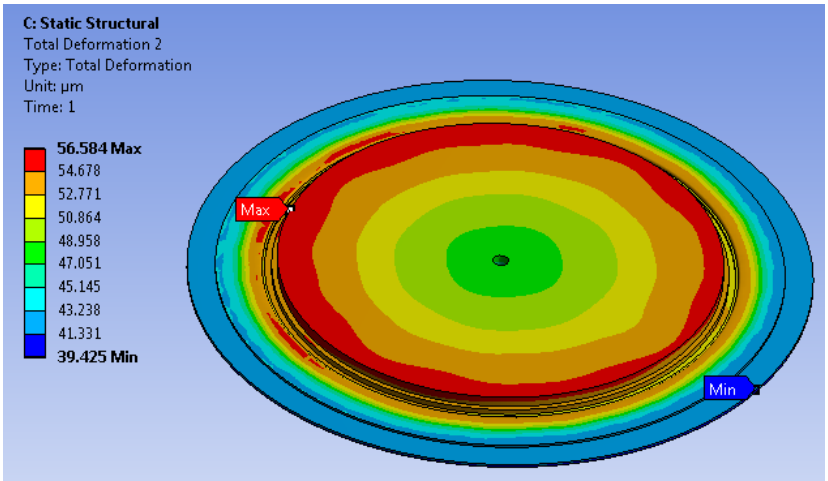

(a)

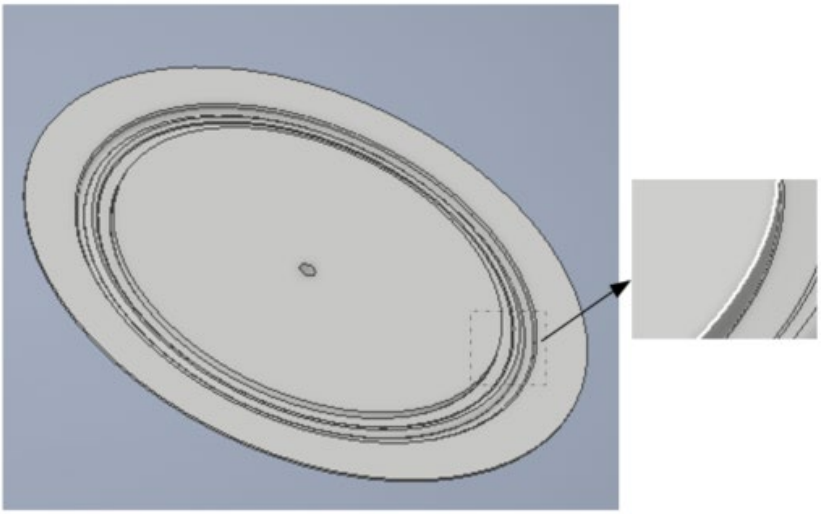

(b)

Figure 3.5 Collector lid groove deformation results (a) Deformation results of the collector lid and (b) detailed schematic of collector lid

In the second simulation, different boundary conditions were set to investigate the influence of heat stress and pressure on deformation. Based on the characteristics of the steady-state operation, each of the 14 IGBT chips and 7 diodes were given the same constant heat loss. The rated current of the press pack was 800A.

This resulted in a heat loss of 600pW/µm^3 for each IGBT and 200pW/µm^3 for each diode (1/3 of rated current effect). With the rated clamping force of 30kN applied to the top heatsink, the temperature distribution across all chips and the deformation distributions along the groove were simulated, as shown in Figure 3.6(a) and (b). The results shown in Figure 3.6 were based on settled power dissipation.

As indicated in Figure 3.6(a), the highest chip temperature was 80°C when the module reached thermal steady state. IGBT chips situated at the outer orbit had on average a lower temperature compared to the IGBT chips placed closer to the centre of the PP IGBT. The highest chip temperatures could be observed at the corners of chips, especially when several IGBT chips were situated close together. The deformation along the groove varied from 39.748µm to 36.968µm. The difference between the maximum and minimum deformations was 2.780µm. The deformation on the groove was more consistent in the direction perpendicular to the tangent plane because the internal pressure and thermal stress were more uniform. This represents the deformation of the device under the rated current and pressure in a healthy state.

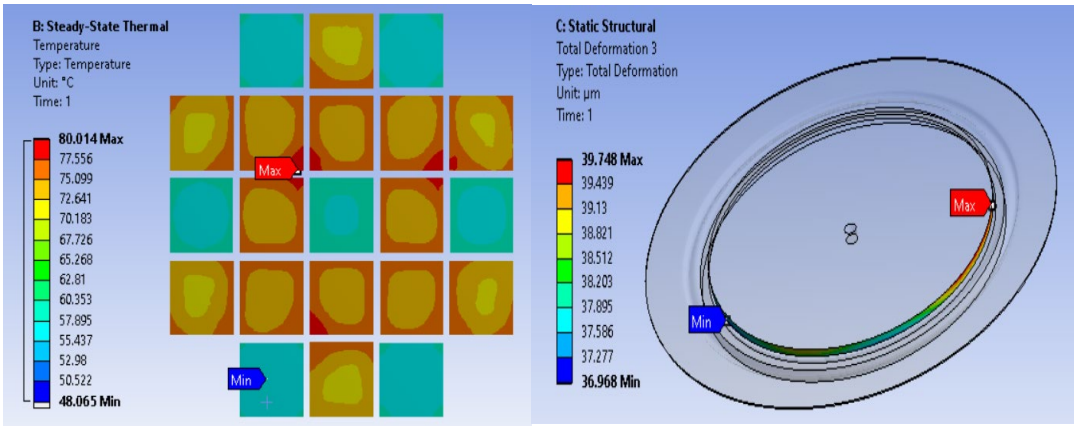

(a) (b)

Figure 3.6 Simulation results (a)Temperature distribution across chip surface and (b) deformation against lid groove at 80°C

Figures 3.7(a) and (b) show the deformation distribution results and the thermal distribution of the chips based on high current dissipation. Heat losses of 1000pW/µm^3 for each IGBT and 700pW/µm^3 for each diode were allocated. As shown in the figures, the temperatures across all chips were much higher than in the previous simulation. The maximum temperature observed was 149°C. The maximum deformation increased from 70.331µm to 73.809µm. The position of the maximum and minimum deformations was the same as in the rated case.

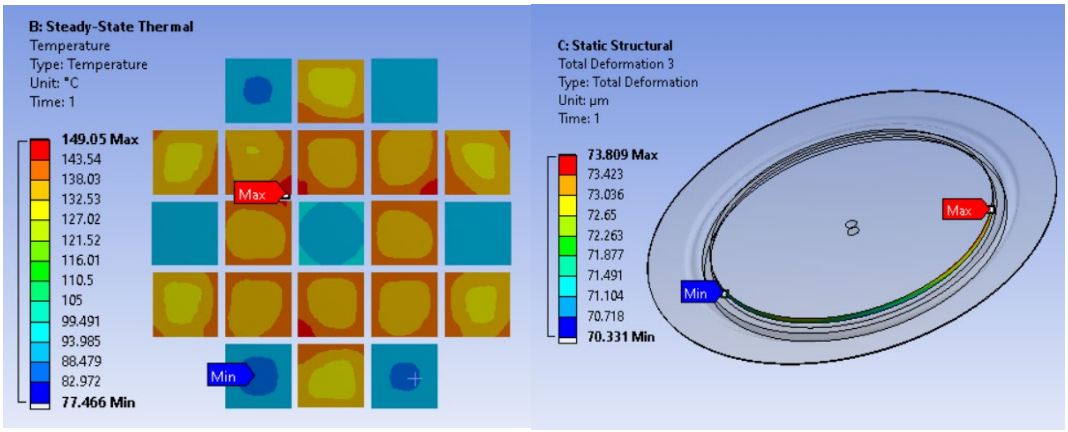

(a) (b)

Figure 3.7 Simulation results (a)Temperature distribution across chip surface and (b) deformation against lid groove at 149°C

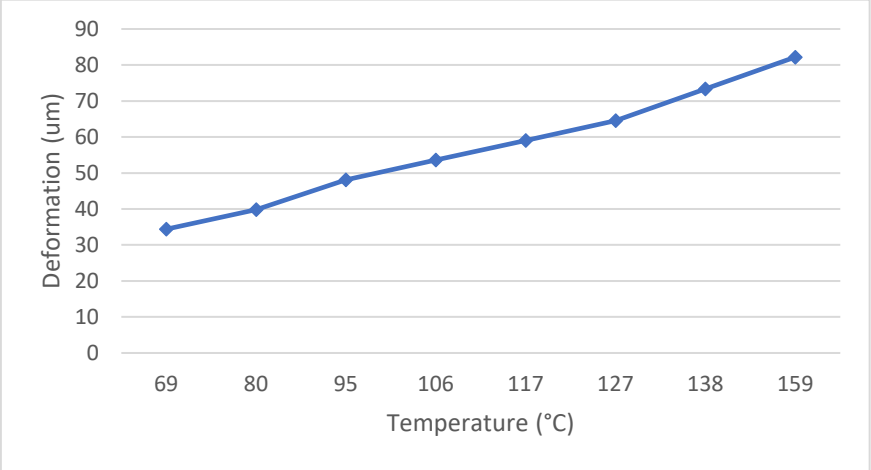

Figure 3.8 Relationship between the maximum temperature of the chip and the maximum groove deformation

In order to study the relationship between groove deformation and thermal stress in a healthy state, the simulation was conducted by keeping the external clamping force constant and altering the power consumption of the chips. Figure 3.8 shows the relationship between the maximum temperature of the chip and the maximum groove deformation caused by varying the power consumption. It is evident that as the power consumption increases, the chip temperature rises accordingly, and as a result, the deformation of the groove increases nearly linearly.

3.3.1 Press-pack simulation varying clamping force

To further investigate the relationship between the groove deformation and the clamping force, a varying clamping force was applied. Figure 3.9 shows how the deformation changed as the clamping force was increased. The power dissipation was kept constant, a heat loss of 800pW/µm^3 was allocated for each IGBT and a heat loss of 300pW/µm^3 was allocated for each diode. As the clamping force increased from 5 to 40kN, the total deformation of the groove (blue curve) decreased. The drop (45µm to 39µm), however, was relatively small. Equation (3.5) expresses the basic total deformation composition, which consists of deformation in three directions. The deformation of the lid along the X-axis was barely noticeable (orange curve).

$$U_{total} = \sqrt{{U_x}^2 + {U_y}^2 + {U_z}^2} \tag{3.5}$$

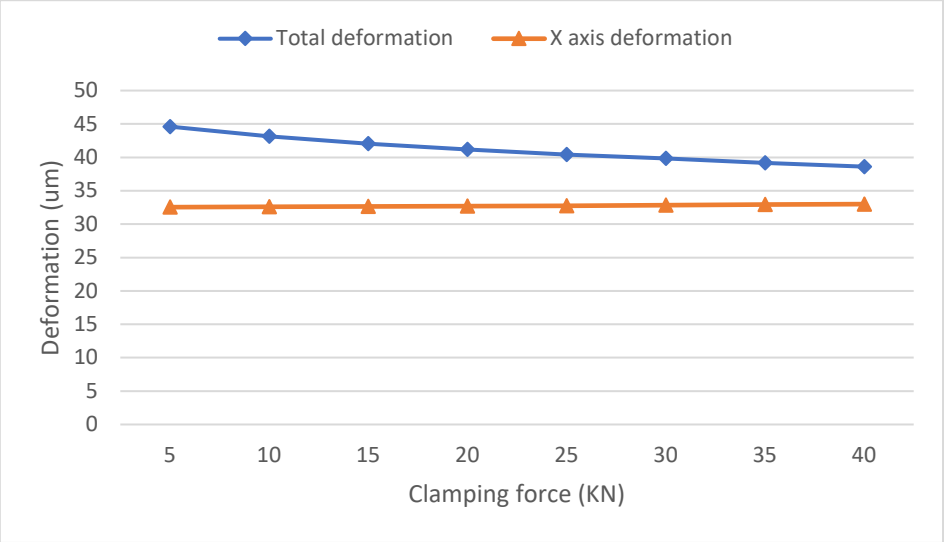

Figure 3.9 Relationship between the clamping force and groove deformation

Comparing the results between altering power density while keeping clamping force constant and varying clamping force while keeping power density constant, it is evident that power dissipation has a bigger impact on the groove deformation than clamping pressure.

3.4 FE simulation using unevenly distributed IGBT power

3.4.1 Press-pack simulation with one chip failed

Up to this point, simulation was carried out assuming an even power distribution across the IGBT chips and diode chips. Likewise, it was assumed that clamping pressure was

equally distributed amongst all chips. In real applications, however, each chip has its own power loss, and clamping forces are not equal. This results in changes in thermal resistances. Some chips are better thermally connected than other. In addition to different thermal resistances, current will also flow unevenly through the chips due to different electric resistances. These changes grow over time and will result in chip failure, which in a PP IGBT results in a short-circuit. This section and the next simulate these scenarios when chips overheat.

In this section, a 3D model containing a failed chip is investigated. When failure occurs, normally the failed chip carries most of the injected current. In this case, the failed IGBT chip was allocated with a heat loss of 3200pW/µm^3, and the rest of the IGBT chips were allocated with a heat loss of 400pW/µm^3. A heat loss of 200pW/µm^3 was allocated to each diode, based on the same total heat loss (1/3 rated current effect). Figure 3.10(a) shows that the overheated chip was placed in the upper left part of the PP IGBT. Figure 3.10(b) shows the groove deformation. The maximum value was 45.83µm and, unlike in previous simulations, the position of the maximum deformation was now close to the position of the overheated chip.

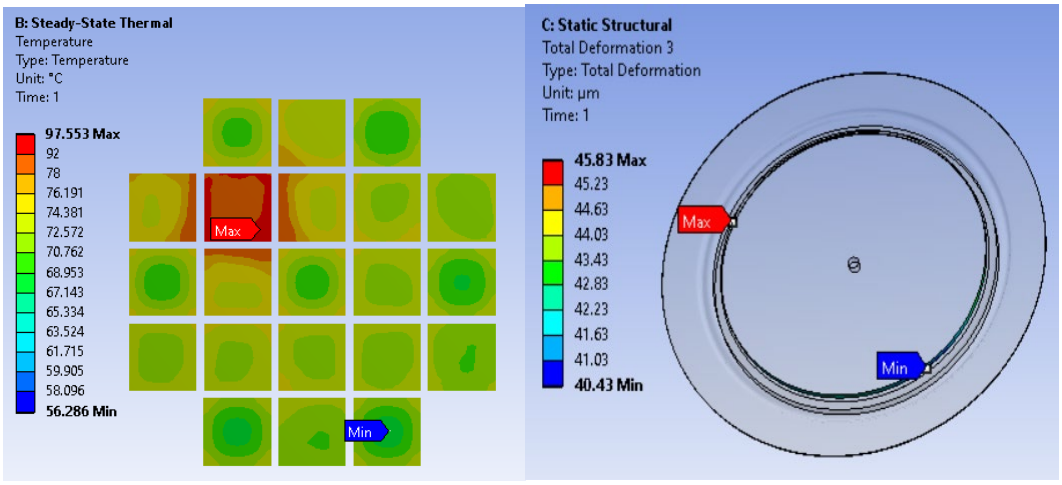

(a) (b)

Figure 3.10 Simulation results (a)Temperature distribution across chip surface with one overheated chip and (b) deformation against lid groove at 97°C

To further explore the influence of the overheated chip on groove deformation, the results displayed in Figure 3.11 were obtained by adjusting the power loss on the faulty chip. As the power loss continued to rise, the deformation value closest to the overheated chip grew, but the deformation values adjacent to the overheated chip also

increased. The reason why the adjacent value increases is because the temperature of the remaining chips rose due to thermal coupling, which caused the overall temperature of the collector lid to rise.

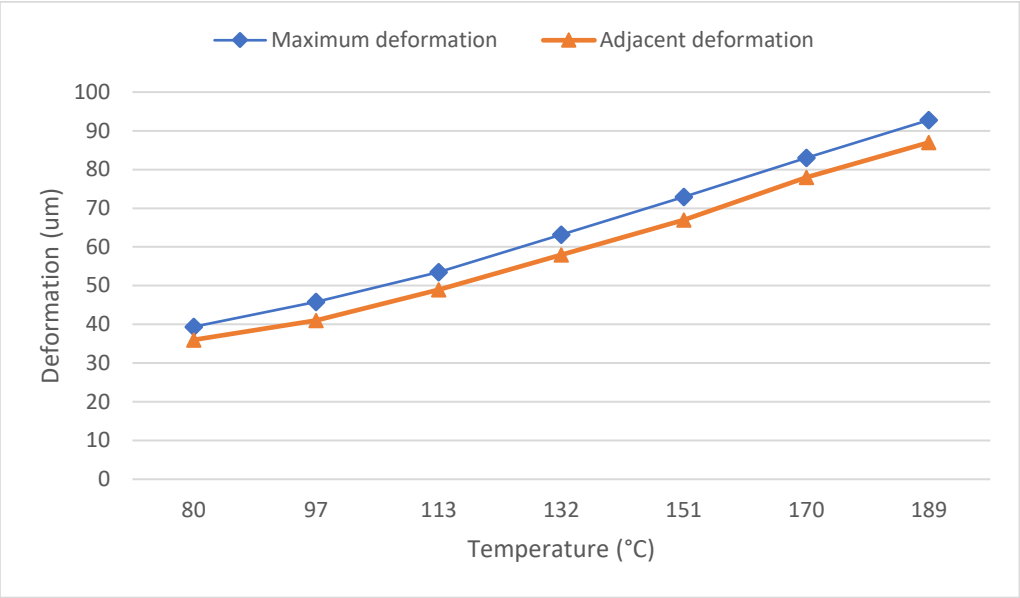

Figure 3.11 Relationship between the maximum temperature on the faulty chip and deformation on the groove

It can therefore be observed that in a healthy PP IGBT that shows an equal power distribution, the groove deformation grows with an increase in power loss and an increase in applied clamping force. The resulting deformation is evenly distributed along the entire groove. However, when a chip is faulty and becomes overheated as a result, the deformation increases at the point closest to the overheated chip. Also, for high chip power loss (short-circuit), the deformation of the entire groove increases.

3.4.2 Press-pack simulation with two chips failed

Although simulation results of an overheated chip show the difference in the deformation at the groove, it is necessary to study the situation when there are multiple overheated chips. This section shows results when there are two overheated chips placed at different positions within the PP IGBT modules.

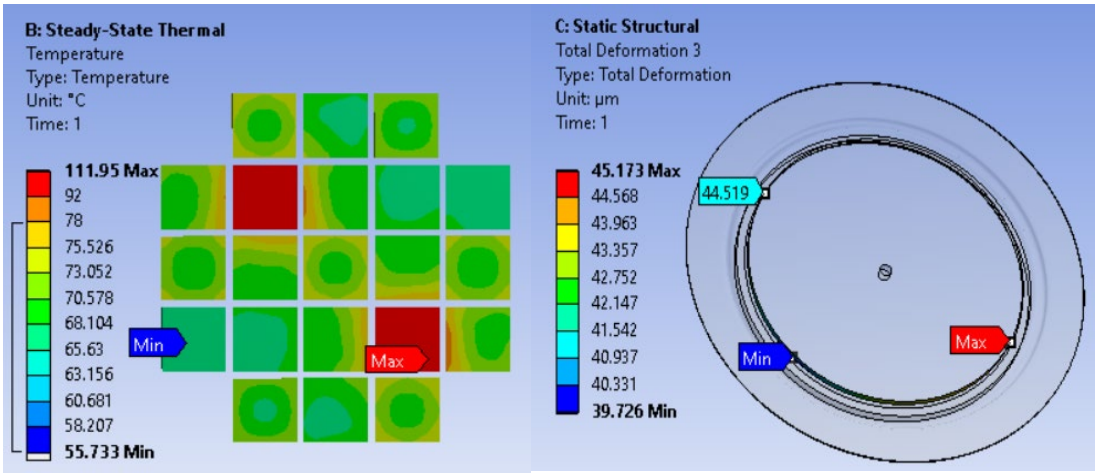

(a) (b)

Figure 3.12 Simulation results (a)Temperature distribution across chip surface with two overheated chips and (b) deformation against lid groove at 112°C

Figure 3.12 shows the deformation distribution on the groove and the thermal distribution on the chip surface with two overheated IGBT chips positioned diagonally to each other. It can be seen that the groove deformation near the two overheated chips was significantly larger than in the remaining circumference of the groove. In order to further explore the influence of two overheated chips, the results shown in Figure 3.13 were obtained by adjusting the power of the faulty chips while keeping the total power unchanged.

Figure 3.13(a) indicates that as the power loss of the overheated chip increased, the deformation of the groove near the two overheated chips increased slightly, while the deformation of the rest of the groove decreased slightly, as shown in Figure 3.13(b), causing greater differences in deformation in different regions. In this case, the current was more highly concentrated on the overheated chip, and the temperature of the remaining chips increased by thermal coupling was slightly lower than before, resulting in a larger difference in the deformation of the groove.

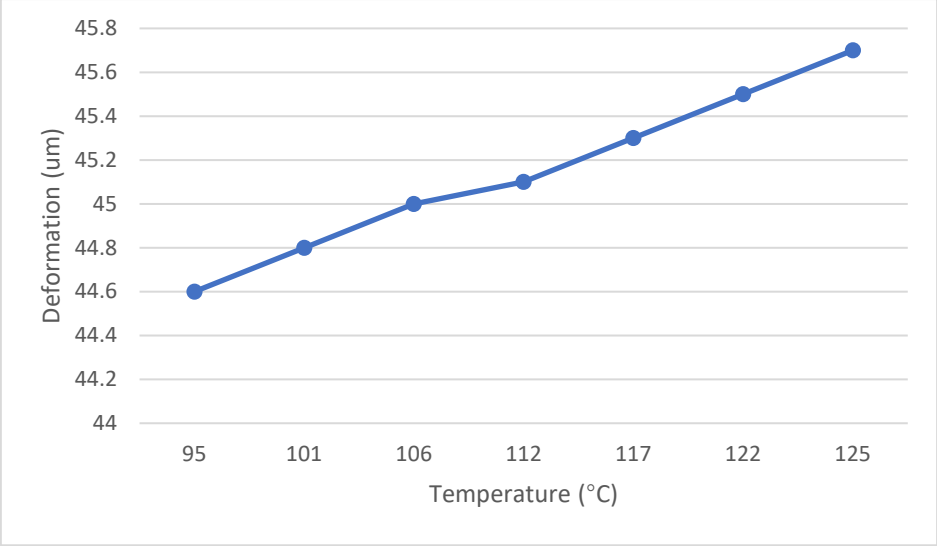

(a)

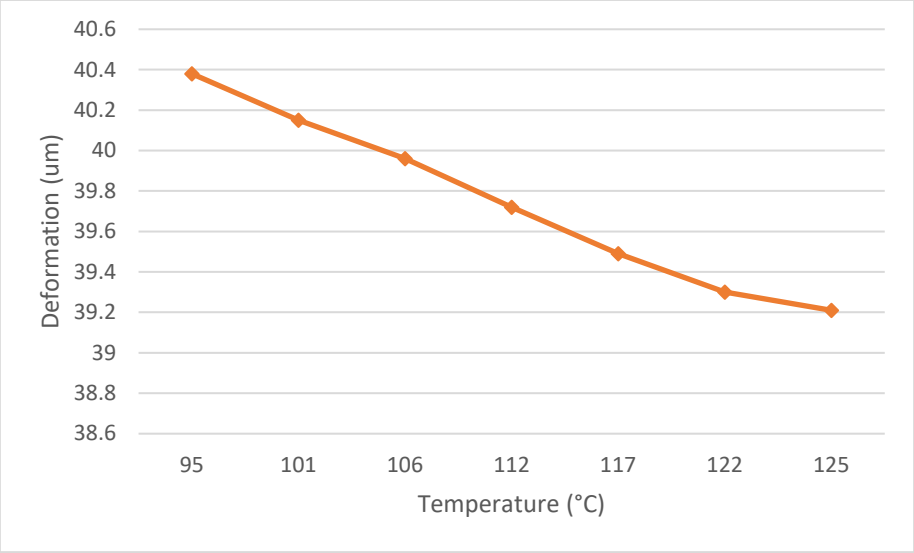

(b)

Figure 3.13 Simulation results for two overheated chips (a) Relationship between the maximum temperature and maximum deformation by increasing the power dissipation on the two faulty chips (b) Relationship between the maximum temperature and deformation of the remaining circumference of the groove

The above results are based on two overheated chips in the diagonal position. In order to better study the influence of two overheated chips on groove deformation, it is also necessary to select two additional overheated chip layouts for simulation. The following discussion focuses on the situation in which two chips overheat or even short-circuit on the same side.

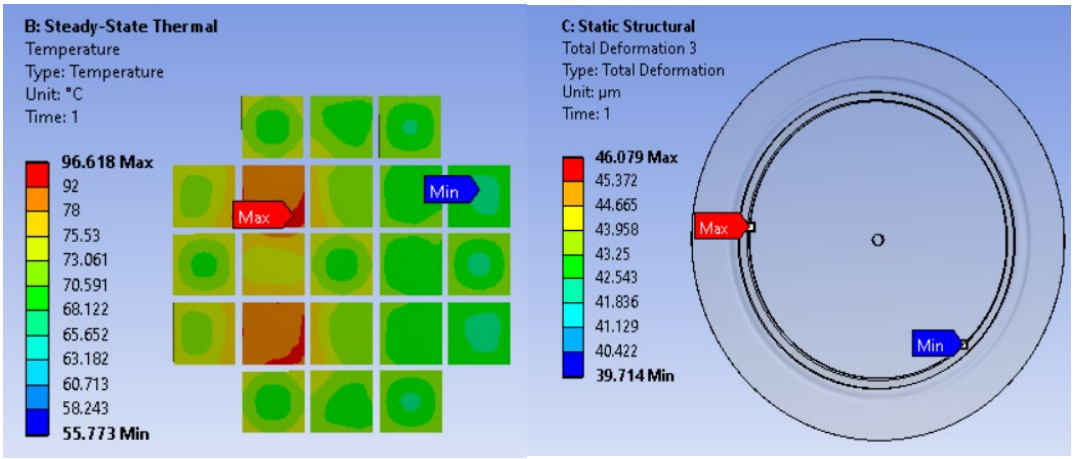

(a) (b)

Figure 3.14 Simulation results (a)Temperature distribution across chip surface with two overheated chips and (b) deformation against lid groove at 112°C

Figure 3.14 shows the results of the deformation distribution and heat distribution for this case. The positions of the two overheated chips are clearly shown, with the maximum groove deformation positioned between the two chips. Compared with the simulation results for an overheated chip, the maximum deformation was reduced under the same total power consumption, but the difference between the minimum deformation points and the maximum deformation point was still obvious.

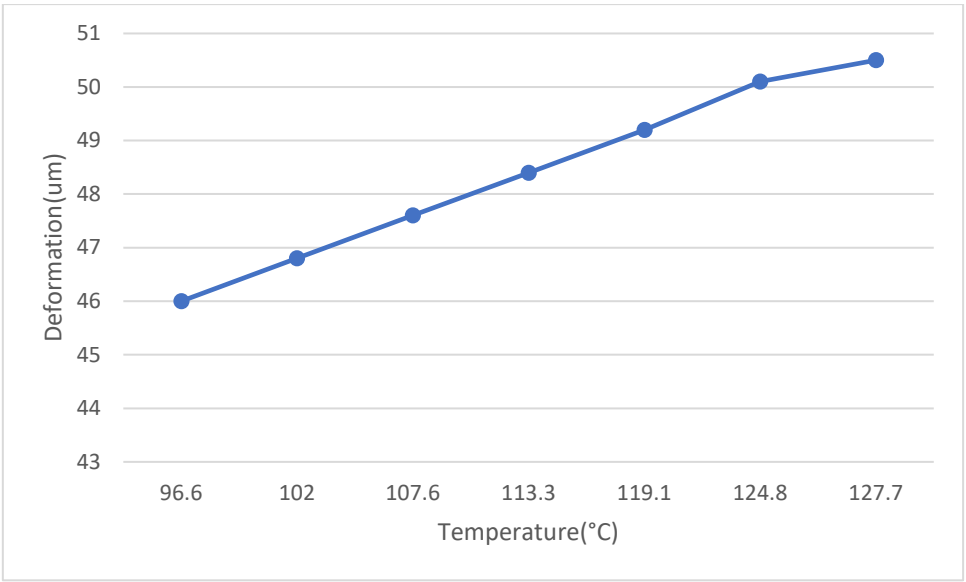

Figure 3.15 Relationship between the temperature and deformation by increasing the power dissipation on the two faulty chips

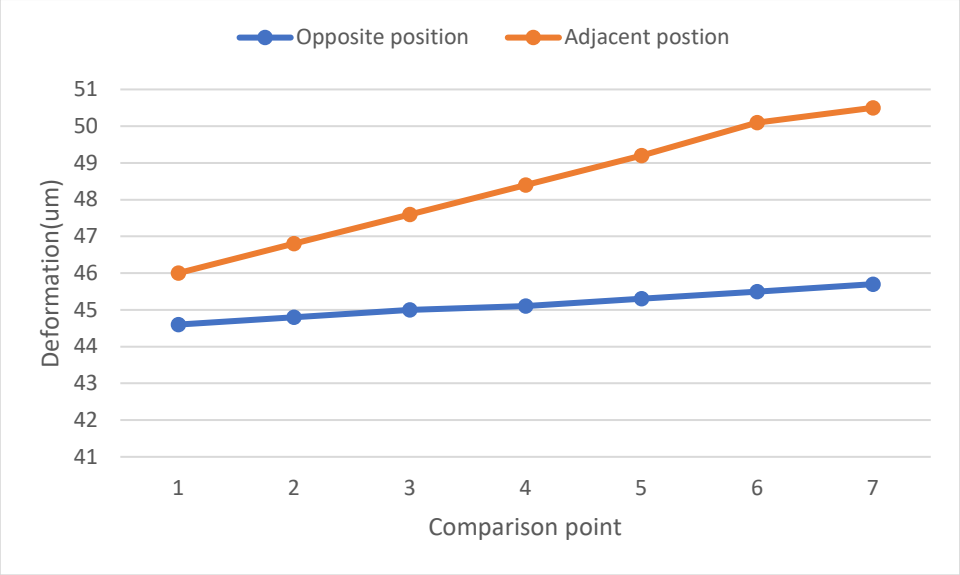

Figure 3.16 Maximum deformation point comparison between the two overheated chips orange: adjacent position and blue: opposite position

Similar to the previous process, the power of the overheated chips was adjusted to study the influence of two overheated chips on groove deformation. In the case of maintaining the total power loss unchanged for all the IGBT chips.

Figure 3.15 shows the deformation as a function of temperature. It can be seen from the figure that as the heat loss of the overheated chips increased, the deformation of the groove near the two overheated chips increased slightly, with the position of the maximum groove deformation point located on the symmetry axis of the two overheated chips. This is caused by the thermal coupling effect.

In order to compare the effect of overheated chips on deformation for the two layouts, the simulation results of the maximum deformation point and the difference between the maximum point and minimum point obtained for each condition are shown in Figure 3.16 and Figure 3.17, respectively. It can be seen from Figure 3.16 and Figure 3.17 the maximum deformation value for the layout with the two faulty chips on the same side is greater than that with the two faulty chips diagonal to each other.

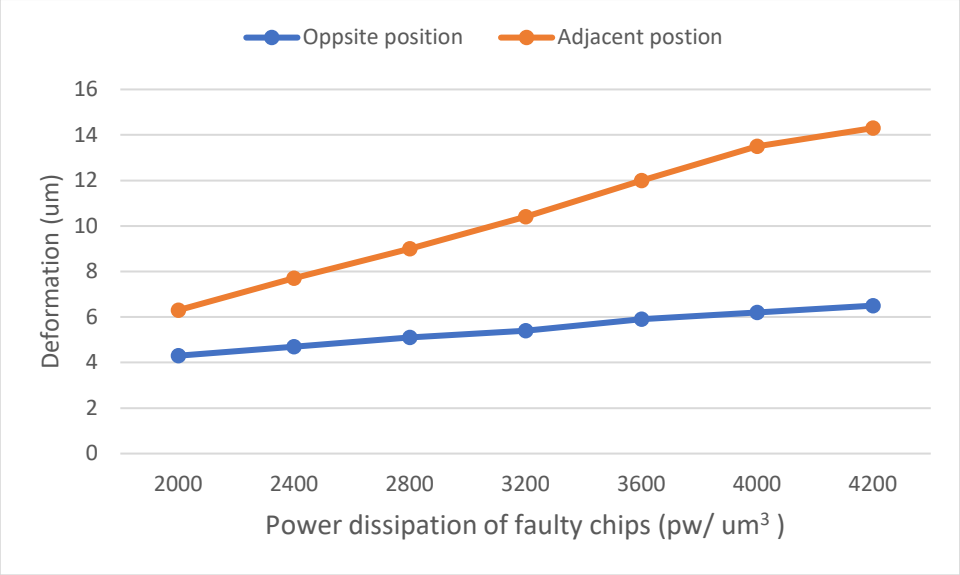

Figure 3.17 Deformation difference comparison between orange: adjacent position and blue: opposite position

3.5 Summary

In this chapter, a detailed deformation analysis based on FE simulation applied to PP IGBT modules was presented. First, the simulation parameters for the FE simulation were selected, and second, a 1:1 high-fidelity model was established. The effect on the deformation of the collector lid groove was investigated by adjusting the power dissipation of the chip and external pressures. In addition, multiple models were established based on the position of the selected faulty chip or chips. The simulation provided evidence that lid circumference measurements can be used to detect faulty chip operations that result in high chip temperatures. The research outcomes from this chapters include the following:

1. The power dissipation of the chip has a greater effect on groove deformation than external pressure.
2. Regardless of the number and position of the faulty chips, the deformation of the groove is larger adjacent to the chip or chips than at other locations on the groove.
3. When the input power is known, the approximate position and number of faulty chips can be determined by the groove deformation.
4. Based on the simulation, it can be concluded that deformation on the lid groove can be used as a new indicator of the health condition of PP IGBTs.

Chapter 4 Deformation detection methods for micro-range applications

4.1 Detection system limitation

As shown in the previous Chapter the deformation on the collector lid groove can be used as a new health condition indicator for PP IGBT. This Chapter identifies a suitable practical sensor that is able to detect deformation of the groove.

As with any sensor, the cost should be low, and it should fulfil additional criteria as well. First, it must fit into the space. The groove is only a few millimetres deep, and due to their physical positions, the distance between the press pack lid and the heat sink is also only a few millimetres.

Thus, the sensor has to be very small in order to fit within the groove. Second, the lid is exposed to very high voltages; therefore, the isolation grade must be high (on the order of several thousand volts). Third, due to switching, PP IGBTs produce high electromagnetic interference (EMI); thus, the sensors must be noise immune. Fourth, as shown in the previous chapter, the absolute value of the deformation is in micrometres, which is small compared to the lid size, which means high accuracy and high sensitivity are required.

According to these practical conditions, several market-available sensors for deformation detection were compared. Table 4-1 lists these commercially available sensors, and each sensor is discussed in more detail in the following sections.

Table 4-1 Deformation Sensors

No.	Sensor	Sensitivity	Immunity	Requirements	Complexity
1	Strain gauge sensor [78][79]	GF=2	Poor	Wheatstone bridge	Medium
2	Low-coherence interferometry fibre-optical sensor [80][81][82]	Nanometer range	High	Need reading unit	High
3	Fabry-perot interferometer [83][84][85]	Nanometer range	High	Same as above	High
4	Capacitive strain sensor [85][86][87]	0.02 Pf/με	Poor	Need additional circuit	Medium
5	ESPI (Electronic speckle pattern interferometry) [88][89][90][91][92]	0.5μm	High	Need CCD camera	High
6	SAWR (Surface Acoustic Wave Resonator) [93][94][95][96][97]	100Hz/ με	Poor	Need network analyzer	Medium
7	FBG (fiber Bragg grating) [98][99][100][101][102]	1pm/με	High	Need integrator	High

4.2 Strain gauge sensor

The strain gauge sensor is a common strain detection sensor that is utilized in various applications. Strain is another word for deformation caused by force. Normally, a strain gauge sensor is a device where the electrical resistance changes proportionally to the amount of strain it is subjected to [78].

Strain gauges offer a number of benefits, including low cost, ease of maintenance, adaptability for long-distance communication, and a simple operation. They do, however, have drawbacks, such as loss of precision over time and the requirement of a very good surface finish for the application.

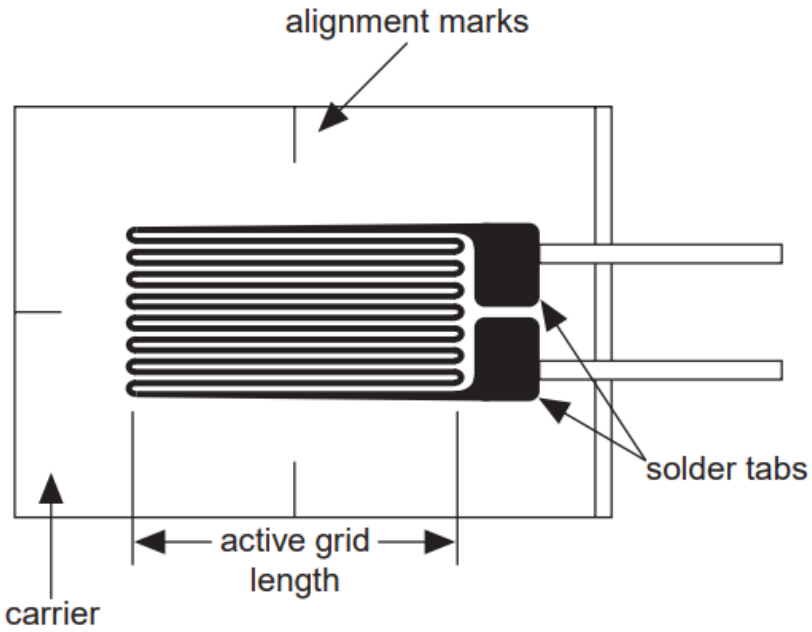

Figure 4.1 Bonded metallic strain gauge [87]

The most widely used gauge sensor is the metallic strain gauge. The metallic strain gauge is made of a grid pattern of very tiny metallic foil wires. Figure 4.1 shows the principal of a bonded metallic strain gauge. To lessen the effects of shear strain and Poisson Strain, the cross-sectional area of the grid is minimised. The grid is adhered to a thin backing, referred to as the carrier, which is connected to the test specimen directly. As a result, the strain of the test specimen is immediately communicated to the strain gauge, which responds with a linear change in electrical resistance.

The gauge factor, which is a quantitative expression of the sensitivity to strain of the gauge, is a basic parameter of the strain gauge (GF). GF is the ratio of fractional change in electrical resistance to fractional change in length, R is the resistance and L is the longitude length of the active grid. Equation (4.1) shows the expression of GF, the typical value of the GF is around 2 for commercial metallic strain gauge [78]:

$$GF = \frac{\frac{\Delta R}{R}}{\frac{\Delta L}{L}} \tag{4.1}$$

In practice, strain measurements rarely include amounts greater than a few milli-strains. As a result, determining the strain necessitates the precise measurement of very minor changes in resistance. Strain gauges are mostly employed in a Wheatstone bridge configuration with a voltage or current excitation source to monitor minor changes in resistance. Figure 4.2 illustrates the general Wheatstone bridge which consists of four resistive arms and is powered by a voltage or current excitation source.

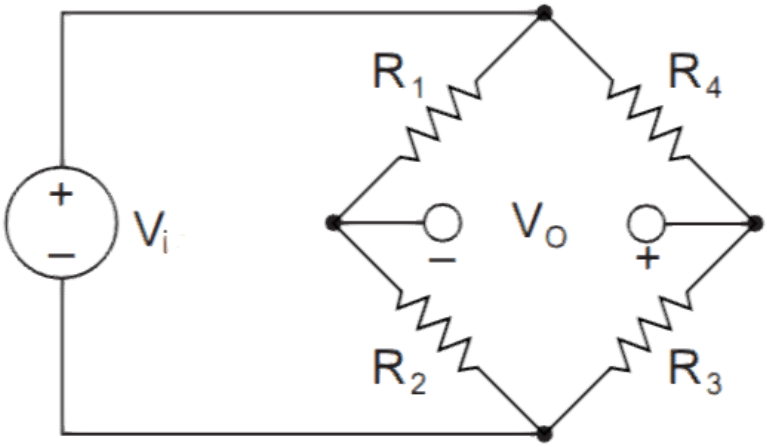

Figure 4.2 Wheatstone bridge circuit

When replacing one resister with a strain gauge sensor, any variations in strain gauge resistance will cause the bridge to become unbalanced, resulting in a nonzero output voltage. Equation (4.2) shows the relationship between the strain and the output of the Wheatstone bridge, where "epsilon" is the strain, V_i is the input voltage, V_o is the output voltage of Wheatstone bridge.

$$\frac{V_o}{V_i} = -\frac{GF \cdot \varepsilon}{4}\left(\frac{1}{1 + GF \cdot \frac{\varepsilon}{2}}\right) \tag{4.2}$$

In order to analyse the feasibility of using strain gauges to measure PP IGBT deformation, electrical simulation was employed. By selecting the most used strain gauge resistance value of 1,000 Ohms, the IGBT drive voltage 15V and the simulated deformation values from the previous sections, the relationship between the deformation and the output voltage ratio is obtained in Figure 4.3.

As can be seen from Figure 4.3, the ratio between output voltage and input voltage varies between 0.0001 to 0.0007, which is very low. Therefore, the noise immunity is poor. Another challenge is the tolerance of the resistors which lead to offsets in the output voltage.

Although strain gauges have the advantage of low cost and low complexity of installation, they are not suitable for PP IGBT deformation measurements due to their low sensitivity and poor immunity to electromagnetic interference.

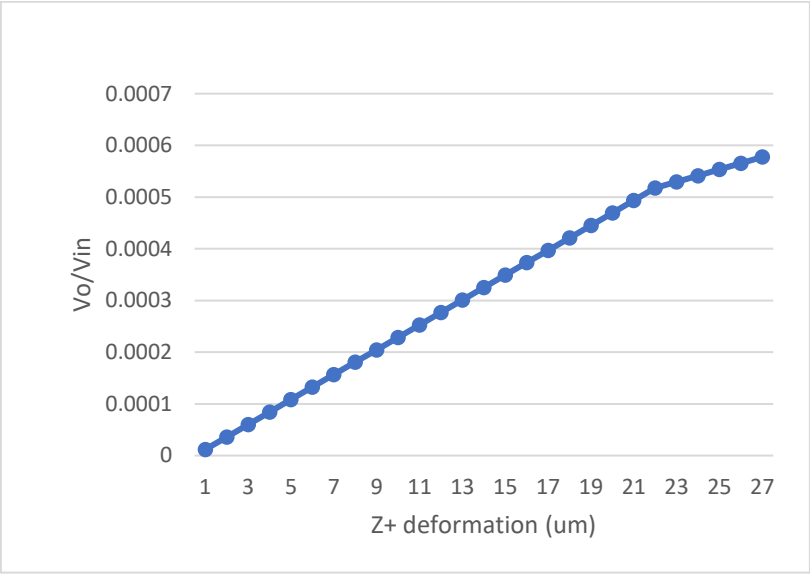

Figure 4.3 Output voltage ratio based on the Z+ deformation

4.3 Low-coherence interferometry fibre-optical sensor

Low-coherence interferometry (LCI) is an optical technology that can be utilized for micron-level accuracy in industrial surface metrology. The signal obtained by an interferometric detector based on LCI fluctuates depending on the external environment, such as changes in temperature, deformation and liquid refractive index.

Figure 4.4 depicts the optical arrangement of a typical fibre optic based LCI system. A Michelson interferometer is made with a single 2x2 fibre coupler [81]. The fibre coupler divides the power of a low coherence source, often a super-luminescent diode, between the sample and reference arms of the interferometer. The light is then reflected and directed back into the readout unit by two silver mirrors situated at the ends of the measurement and reference fibres.

Optical interference can only be noticed if the difference in the pathlength between the reflected beam of the sample and the reference arm is less than the coherence length of the light source [80].

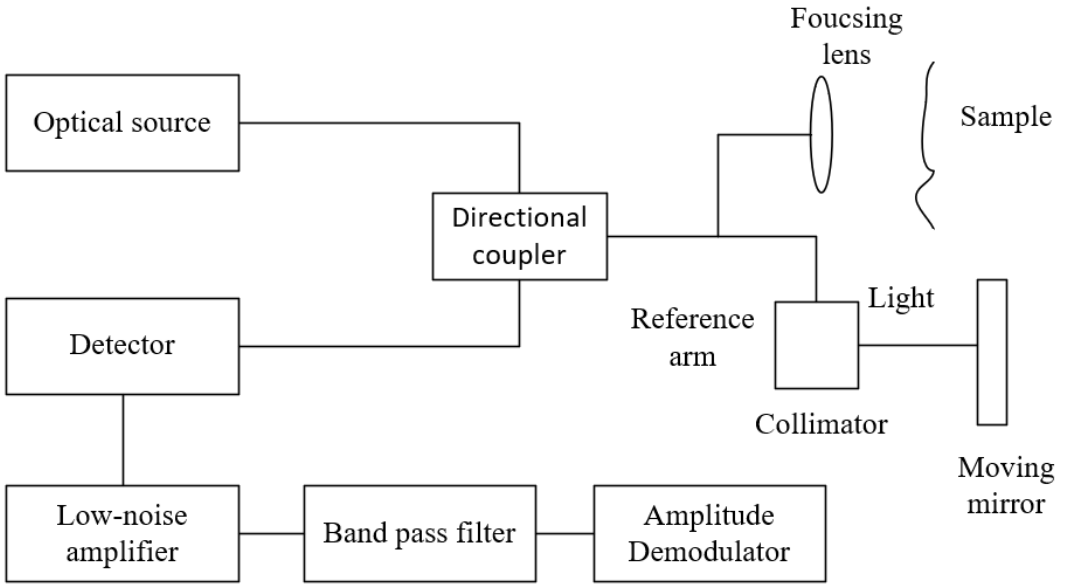

Figure 4.4 Configuration of low coherence interferometry optical sensor

Like most fibre optic sensors, those based on the LCI principle are highly immune to EMI and sensitive, but at the same time they are expensive and difficult to install. Figure 4.5 depicts the internal structure of a sensor based on the LCI concept [81]. A pair of fibres placed in suitable packaging make up the sensitive section. The measuring fibre is pretensioned and mechanically linked to two anchor locations to track the structure's deformation, whereas the reference fibre is not pretensioned nor anchored. The change in integrated strain between the two anchor sites is proportional to the difference in the length of these two fibres.

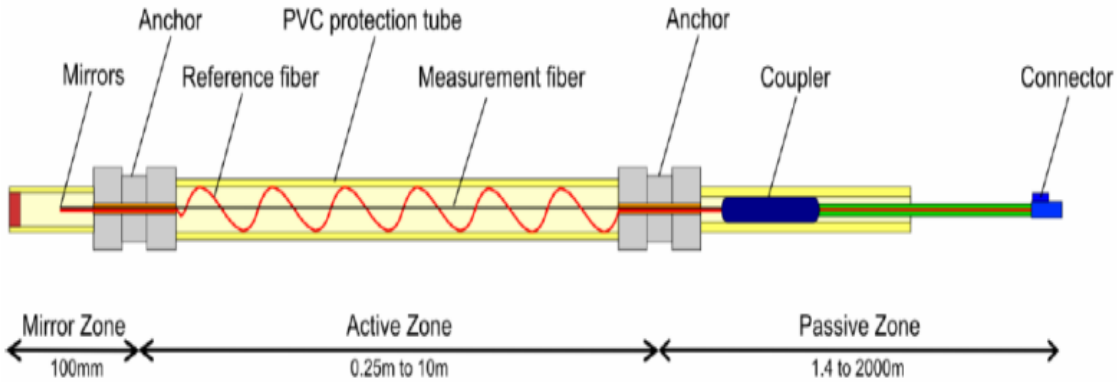

Figure 4.5 Standard configuration of low coherence interferometry deformation sensor [90]

In terms of the sensitivity of the LCI sensor, it can detect nanometre range deformation

[89]. Based on the simulation results in the previous sections it was shown that PP IGBT deformation are in the order of a few tens to a few hundreds of microns, and therefore the sensitivity of the LCI-based fibre optic sensor matches these conditions.

Although this technique may work for one device, it is not applicable for measuring deformation for several PP IGBTS. That is because the sensor measures the integrated strain between two anchor points. This means that the number of optical probes increases relatively. In addition, due to the presence of two internal optical fibres, the sensor needs to be encapsulated, which is typically in the size of several millimetres in diameter, meeting the recess dimensions but also making installation more difficult. Overall, this solution is costly and difficult to be installed.

4.4 Fabry-perot interferometer sensor

The Fabry–Perot interferometer (FPI) is another alternative for measuring deformation. Multiple reflections between two closely separated smooth mirror surfaces are used in this interferometer [84]. Figure 4.6 depicts the operation concept of this device. When light reaches the second surface, a portion of it is transmitted, resulting in numerous offset beams that might interfere with one another. When the external environment changes and a deformation occurs, the distance between the mirrors changes, resulting in a change in the interference fringes.

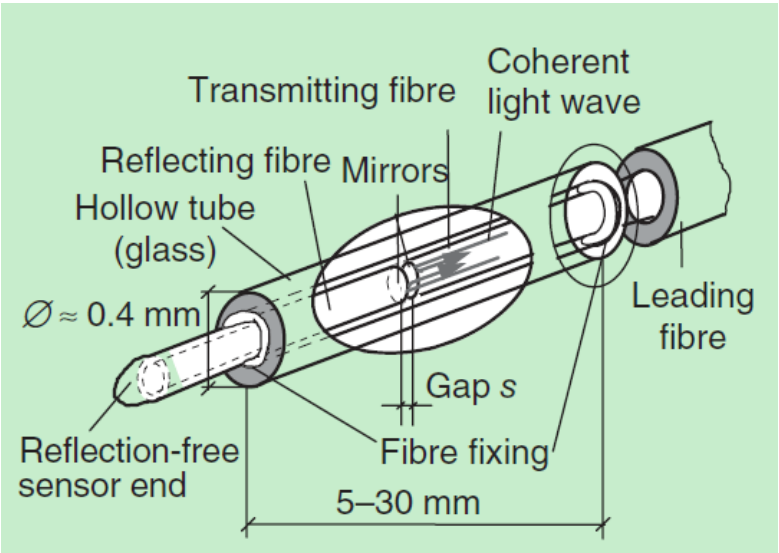

Figure 4.6 Operation principle of Fabry-Perot interferometer [84]

Similar to the previously compared optical fibre sensors, the advantages of FPIs include their small size, light weight, high accuracy, resistance to EMI and high tolerance of

corrosive environments. Concomitantly, their disadvantages include their difficulty in mounting and use of multiple connections.

The sensor in this example is made up of two mirrors (two fibre-optic ends) facing each other, as shown in Figure 4.7 [86]. By utilising tubes aligned and combined to generate an air gap that acts as a low precision Fabry–Perot cavity of length d, one fibre acts as an input–output fibre and the other acts solely as a reflector. Currently commercially available sensors can achieve a sensitivity of 0.1μm/m, meeting the deformation requirements for measuring PP IGBT health conditions.

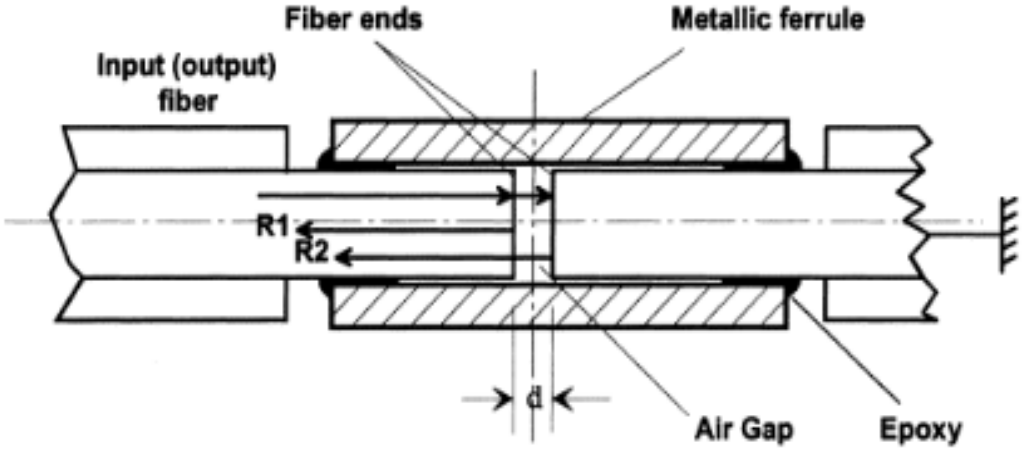

Figure 4.7 Typical construction of FPI [86]

In terms of required size, the two fibres forming the air gap need to be aligned so that encapsulation is indispensable and the PP IGBT collector recess must be of sufficient size to accommodate which in practical terms is hardly achievable. In addition, the need for multiple points of measurement requires the use of multiple FPIs and interferometers which add significantly cost. Therefore, FPIs are less feasible for detecting groove deformation.

4.5 Capacitive strain sensor

Another possible option is the capacitive strain sensor which can be used for detecting deformation. The capacitance variation between the two flexible conductive plates is the operating principle of the sensor. Variations in the distance between the capacitor plates and the electrode surface area occur when the sensor is under strain, affecting the device capacitance [87][88]. Capacitive strain sensors can be tailored to the object being monitored. This is because these sensors can have electrodes with different pitches and areas.

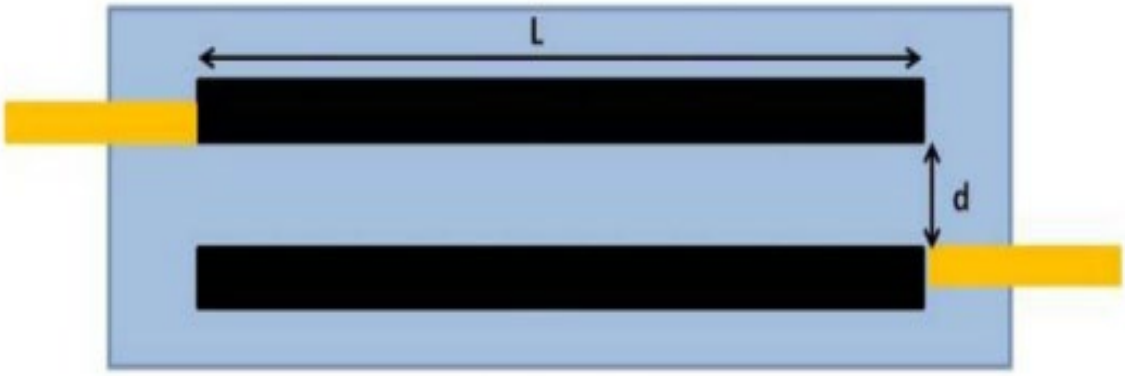

Figure 4.8 Layout of the capacitive strain sensor [87]

Figure 4.8 shows the basic schematic construction of the capacitive strain sensor. The two electrodes are made of copper. The coating of the two plates is inside the polydimethylsiloxane (PDMS) elastomeric structures due to their non-conductive. The initial capacitance value of the plate is:

$$C = \frac{\varepsilon_0 \varepsilon_r A}{d} \tag{4.3}$$

Where εr is the relative permittivity for the medium between the two plates and ε0 is the dielectric constant of free space equal to 8.85 x 10^{-14} F/cm [96], A is the electrode surface area and the d is the distance between the plate. When the strain applies to the sensor, the output capacitance changes accordingly.

Commercial capacitive strain sensor can detect 1-1000 με deformation which meets the need to detect groove deformation. However, the sensitivity of capacitive strain sensors increases with the area of the electrode plate and is therefore limited for this application, because the groove surface area is very small. Furthermore, although a flexible insulating material is used as a substrate for the electrodes, additional circuitry is required to measure changes in capacitance. This circuitry however is exposed to strong EMI generated by the switching devices and therefore causes a risk to produce exact measurements.

Therefore, although the cost of the capacitive strain sensor is low, reliability is not high considering the actual measurement environment.

4.6 Electron speckle pattern interferometry (ESPI)

Electron speckle pattern interferometry (ESPI) is a full-field, non-contact optical metrology technique for measuring displacement and strain. For displacement and

strain measurements, the adoption of ESPI in industry has grown over the last few decades. Recently, it also has moved into MEMS and healthcare applications [88].

The ESPI method is often used to measure the deformation of opaque surfaces. Microelectromechanical systems [89], solder connections [90], flip-chip packaging [92] and vibration analysis are some of its applications [91]. Statistical interference patterns, known as speckles, are created when a rough surface is illuminated using coherent laser light and then imaged with a CCD camera.

An interferogram is created by superimposing a reference light split from the same laser source onto these speckles. When the surface of an object is distorted, the speckle interferogram changes as well. ESPI surface deformation measurements are typically separated into in-plane and out-of-plane measurements, with sensitivity limits of 80 and 25nm, respectively [90]. Figure 4.9 shows the schematic of an out-of-plane measurement using ESPI.

As shown in Figure 4.9, the speckles, like fingerprints, are a part of the studied surface. The speckle interferogram changes as the test object is loaded, such as through mechanical methods, thereby distorting the surface. When an interferogram of the surface is compared before and after loading, a fringe pattern appears, revealing the surface's displacement as contour lines of deformation [92].

Due to the presence of speckles, these qualitative fringe images have poor contrast and are noisy. A technique known as phase shifting creates a quantitative phase map from a series of speckle images for each surface condition. This phase map, unlike the fringe images, has quantitative and directional information that can be readily converted into a displacement value.

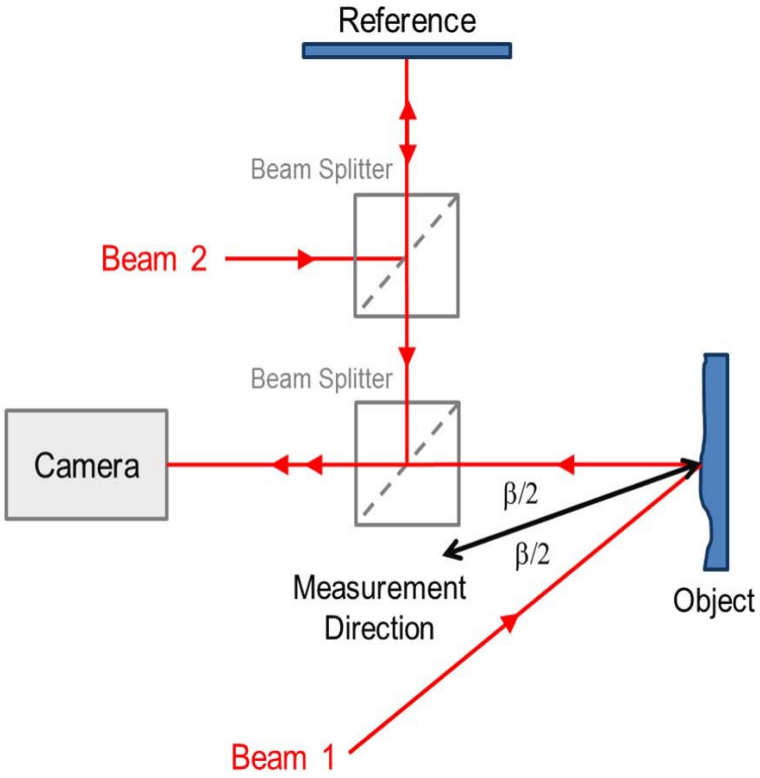

Figure 4.9 ESPI out-of-plane configuration [90]

Equation (4.4) express the basic displacement of the surface, where dop is the out-of-plane displacement, N is the fringe order (phase divided by 2π), λ is the wavelength of light, and β is the angle between the two beams

$$dop = \frac{N\lambda}{1 + \cos\left(\frac{\beta}{2}\right)} \tag{4.4}$$

In contrast to several of the previous methods, there is no doubt that ESPI has sufficient resolution to detect deformation. Furthermore, due to the non-contact measurement, ESPI is also very resistant to interference, and the laser can easily be directed to the groove surface. However, several disadvantages must be considered with ESPI, such as its requirement of at least one set of cameras to set up a module's recess for measurement.

This can be satisfactory for verification in laboratory conditions, but in real-world applications the inspection of multiple modules in series not only increases the cost significantly but would also be difficult to construct. Therefore, ESPI is not a suitable technique.

4.7 Surface Acoustic Wave (SAW) sensor

SAW sensors have been used as deformation sensor. This is due to their advantages such as robustness, compact size, low cost and wireless passive sensing [93].

SAW sensors, are made out of fork-finger or interdigital transducers (IDT) and their spacing may be stretched or shortened, resulting in a shift in resonant frequency [94]. Figure 4.10 shows the basic structure of a SAW sensor with a piezoelectric substrate.

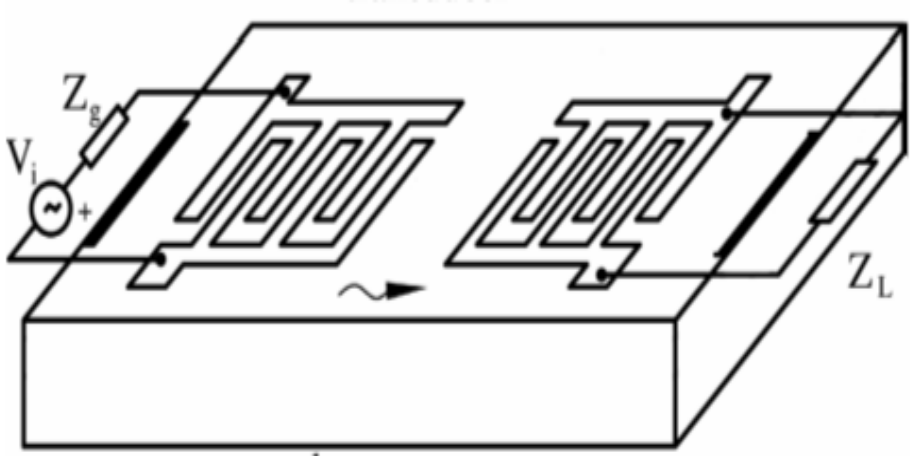

Figure 4.10 Basic SAW sensor structure with a piezoelectric substrate

Figure 4.10 shows that IDT are placed on a piezoelectric substrate by a photolithography and stripping process. The left IDT is excited by an external electric source producing a surface acoustic wave on the substrate. The right IDT receives the wave and converts it into an electrical output signal that can be measured. As the piezoelectric substrate is placed on the surface that shrinks or expands the distances between the fingers changes resulting in a different electric output signature. Equation (4.5) describes the sensor sensitivity to express the linear relationship between the change in strain level and the change in frequency [95], where f is the initial frequency, the f_r is the measured frequency and the ε is the strain.

$$Ssen = \frac{f - f_r}{\varepsilon} \tag{4.5}$$

Typical SAW sensors have a sensitivity in this range from 100Hz/ με to 200Hz/ με [95], which is well suited to the needs of lid groove degradation. However, the usual SAW sensor with a piezoelectric substrate cannot be used well in the collector groove of a PP IGBT module due to the rigidity of the substrate. A flexible SAW sensor based on a single crystal LiNbO 3 film could be used due to its flexibility instead (Figure 4.11 [96]).

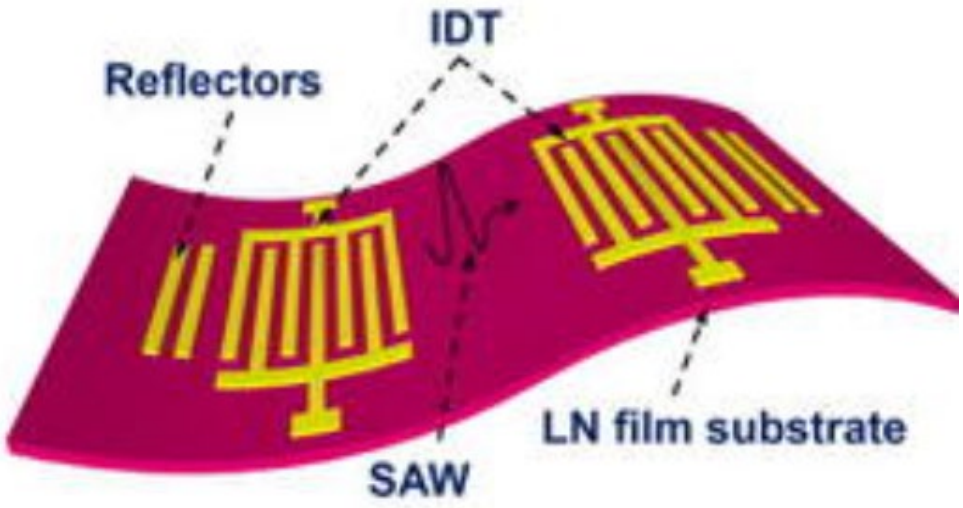

Figure 4.11 SAW sensor structure based on single crystal LiNbO 3 film substrate [97]

While single crystal LiNbO 3 SAW sensors can be well embedded in a PP IGBT collector groove, these sensors require the application of external excitation circuit to operate, which can be influenced by the switching noise. In addition, each PP IGBT would need its own external circuitry adding complexity and cost.

4.8 Fiber Bragg Grating (FBG) sensor

FBG sensor is a grating-based sensor which is a simple and intrinsic sensor. Over the last few decades, FBG sensors have developed rapidly, taking them from being a technology based primarily on laboratory applications to working extensively in practical applications [98]. It has several advantages such as: small size, good corrosion resistance, immune to electromagnetic interference, low thermal conductivity, and distributed measurement ability [99].

Figure 4.12 shows the basic construction of FBG sensing system. The basic principle of the FBG-based sensor system is injecting laser light into the coupler via a broadband light source, all the way into the FBG fibre and all the way to the centre wavelength of the injection being monitored. Then the shift of the reflection or transmission center wavelength (Bragg) is detected by an optical spectrum analyzer, the shift is related to the amount of strain.

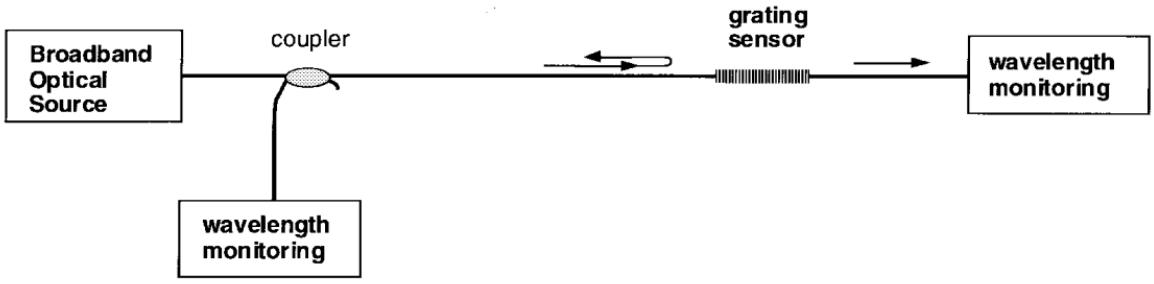

Figure 4.12 Basic FBG sensor system configuration [98]

Figure 4.13 illustrates the corresponding change in the spectrum when the sensitive area of the grating senses a change in the external environment. It can be seen that both the reflected and transmitted spectra show a shift in the Bragg wavelength of the device.

Similar to several previous fibre optic sensors, the sensitivity of the FBG is perfectly suited to measure the deformation of the lid in PP IGBT. Equation (4.6) developed for vacuum, describes the Bragg wavelength of the FBG, λ_B is the function of the periodicity of the grating Λ and the effective refractive index of the fiber n_{eff} [100].

$$\lambda_B = 2n_{eff}\Lambda \tag{4.6}$$

Figure 4.14 shows an important advantage of the FBG, as the measurement is a change in the central wavelength of the grating, by giving different wavelengths to different gratings, it is possible to achieve multiple measurements on a single sensor [100].

This is a fundamental advantage compared to the sensors previously discussed as one string of fibre can hold hundreds of sensors. It is therefore possible to measure the grooves of hundreds of in series connected press packs with only one long string of fibre. The deformation for each groove can be monitored with a single light source and only one spectrum analyser which makes it a cost-effective solution, in particular when compared to the cost of HVDC systems.

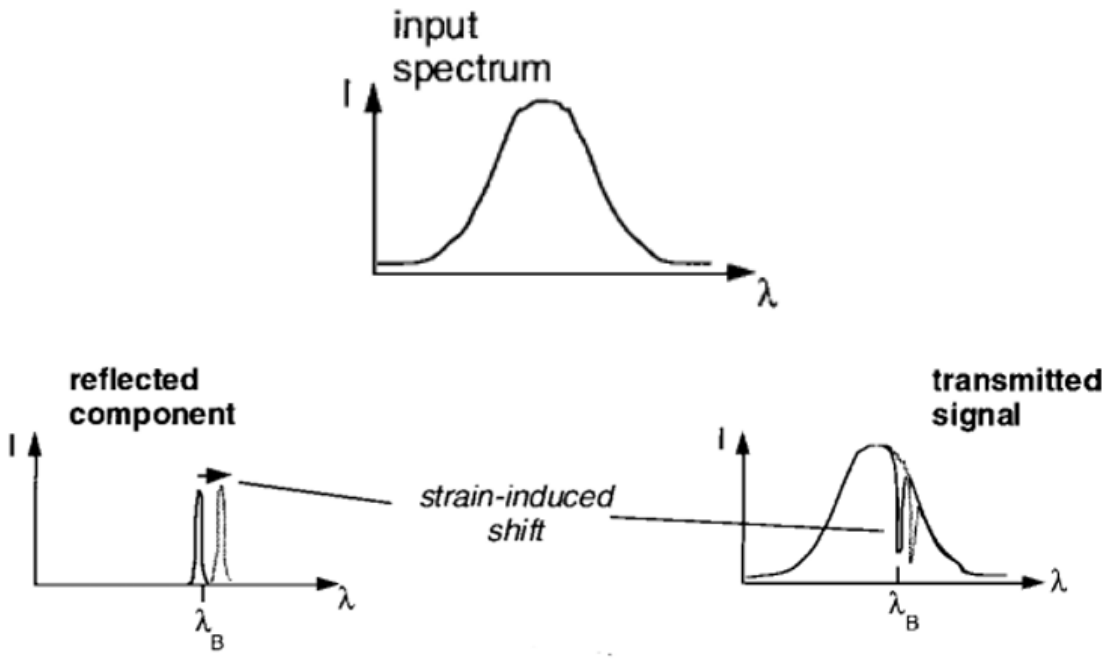

Figure 4.13 Wavelength shift when strain is induced [107]

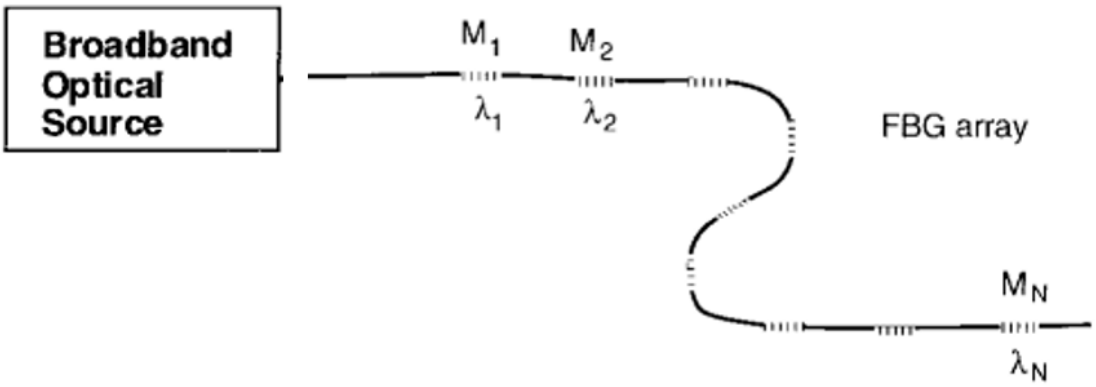

Figure 4.14 Distributed measuring system of FBG array [98]

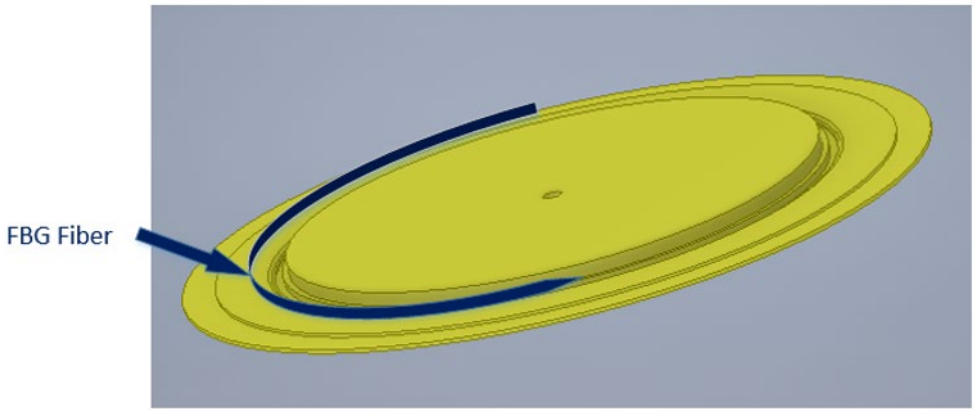

Figure 4.15 Positioning of FBG onto the copper collector lid

Optical fibres are perfectly sized, as on one hand they are small in diameter (millimeters) and on the other hand they can be bended to follow a curved structure. Figure 4.15 shows the principal schematic of positioning a FBG fiber to measure the deformation of the lid. The idea is to wrap the fiber around the groove. Therefore, the FBG sensor is selected as the main sensor for detecting groove deformation of PP IGBTs.

4.9 Summary

In this chapter, several sensors are described and compared. Sensors can be generally categorized into the type of output they produce e.g., voltage, light and frequency. Strain gauge and capacitive strain sensor measure deformation based on the change of the output voltage, the sensitivity of the two sensors is sufficient as they operate in micrometer range. Both sensors have advantages in cost, however, the immunity to the electro-magnetic field is poor. SAW sensor detects the deformation by measuring the change of the frequency of an acoustic wave. Immunity to electro-magnetic noise remains poor and the connection between the sensor and the device is difficult. The long-gauge-length fiber optical sensor and FBG sensor are fiber optical sensor, the immunity is high enough as well is the sensitivity. Fabry-Perot interferometer sensor and ESPI sensor are based on the interferometry principle to detect deformation. Their sensitivity and immunity meet most of the requirements, but both sensors require expensive additional detector units. Of all the sensors discussed it was concluded that FBG sensors are the best choice for detecting groove deformation.

Chapter 5 Implementation of FBG sensor for deformation detection

5.1 FBG sensor comparison and selection

The previous chapter describes the relationship between deformation of the lid grove and IGBT chip temperature. An increase in temperature leads to deformation that can be measured with FBG. The position and amplitude of deformation can be used to estimate the approximate location of faulty chips. This chapter describes the hardware setup that shows the FBG in operation and the chapter will confirm the new proposed TSMP technique.

5.1.1 FBG operating principle

The basic operation principle of the FBG-based measurement system is to monitor changes in wavelength of the Bragg centre as influenced by external parameters such as deformation and temperature. A single-mode fibre core is exposed transversely to intense UV light in a periodic pattern to create Bragg gratings. The refractive index of the fibre core is permanently increased by exposure to strong UV radiation, resulting in a fixed refractive index modulation dependent on the exposure pattern. A grating is a type of fixed refractive index modulation.

Each spatially periodic change in refractive index reflects a small amount of light. All reflected light is coherently merged into a single big reflection with a specified wavelength when the grating period is nearly half the wavelength of the input light. The Bragg condition is the name for this. The wavelength at which incident light is reflected is referred to as the Bragg wavelength. Other wavelengths of light are largely unaffected by the Bragg grating and will continue to pass through the fibre grating. As a result, light propagating across the grating experiences negligible signal attenuation or modification. Only wavelengths that satisfy the Bragg criterion are affected and reflected significantly.

As mentioned in previous chapter, the central wavelength of the reflected light satisfies the following Bragg equation:

$$\lambda_B = 2n_{eff}\Lambda \tag{5.1}$$

Both the refractive index and the grating period are influenced by changes in external parameters, so the magnitude of the change in wavelength at the centre of the reflected light can be used to determine the change in the corresponding physical quantity at the site to be measured.

In order to calculate the sensitivity of the Bragg wavelength with the strain, (5.2) is obtained that the sensitivity with strain is the partial derivative of (4.6) with respect to displacement:

$$\frac{\Delta\lambda_B}{\lambda_B} = 2n_{eff}\frac{\partial\Lambda}{\partial L} + 2\Lambda\frac{\partial n_{eff}}{\partial L} \tag{5.2}$$

The first term in (5.2) is the strain of the grating period due to the extension of the fiber, and the second term is the variation of the index of refraction caused by the strain.

$$\frac{\Delta\lambda_B}{\lambda_B} = (1-\rho_e)\varepsilon_{FBG} \tag{5.3}$$

The expression (5.3) describes the classical form of the Bragg wavelength displacement with the strain which combined both phenomena, where ε_{FBG} is the longitudinal strain of the grating, and the ρ_e is the photo-elastic coefficient which has a numerical value of ≈ 0.22.

Therefore, based on (5.3), the strain can be measured by sensing the shift of the central wavelength. However, the results measured using FBG sensor measurements have both the effect of deformation and the effect of coupling temperature. Therefore, the effect of temperature on the center wavelength change of the fibre needs to be removed.

The formula (5.4) expresses the pure deformation measured by FBG sensor, where CTE is the coefficient of thermal expansion of the specimen, TCS is the temperature cross sensitivity of the FBG sensor, ΔT is the change of the temperature.

$$\varepsilon = \varepsilon_{FBG} - (CTE + TCS)\Delta T \tag{5.4}$$

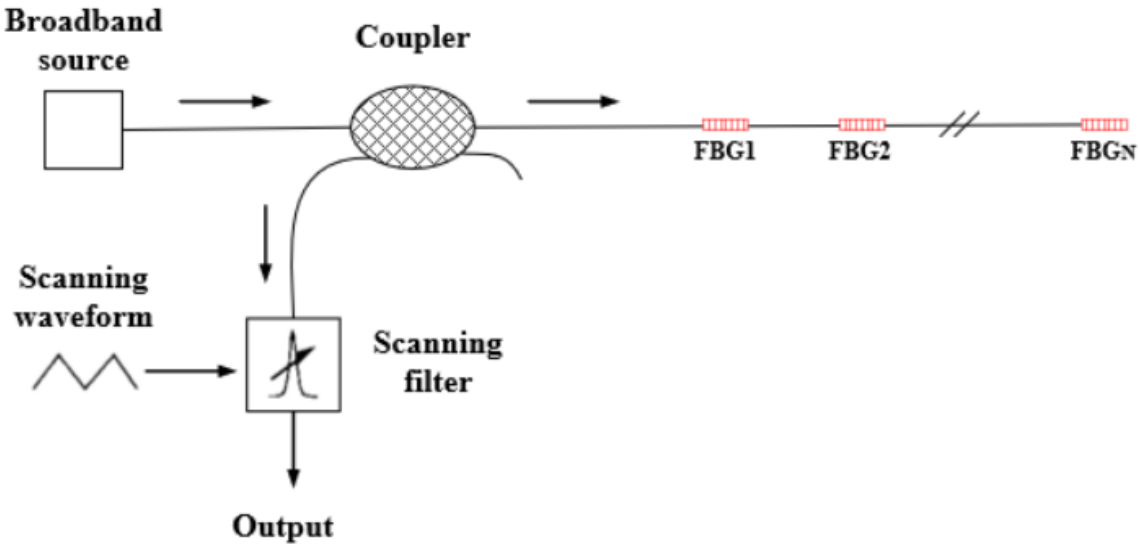

Figure 5.1 Scanning filter interrogating FBG technique

Another important aspect that makes up an FBG-based measurement system is reliable wavelength interrogation. The use of scanning variable passband filters to track the FBG signal is one of the most successful approaches for interrogating FBG sensors. Figure 5.1 shows the basic FBG grating detection technic by using scanning filter.

As can be seen from Figure 5.1, a coupler returns light reflected from a Bragg grating sensor array to a scanning adjustable optical filter and a detector. Depending on the spacing between the mirrors in the device, this filter passes a narrow band wavelength component.

A piezoelectric stack controls the mirror spacing electronically, allowing the passband wavelength to be tuned. When the filter is tuned, the passband is scanned for the return signal of the grating, and when that signal is detected, the wavelength can be estimated and recorded using the voltage of the filter. The sampling rate of the interrogator which can record the reflect wavelength is up to 1k Hz.

5.1.2 Selection for FBG sensor

There are different FBG sensors available on the market. All of them have advantages and disadvantages and Table 5-1 summarises the most common FBG sensors available. All sensors can achieve a sensitivity of 1pm/ με change of central wavelength which is sufficient for the proposed TSMP.

Table 5-1Commercial FBG sensors

FBG for strain	Housing material	Housing diameter	Temperature dependencies	Price £
SMW-01 (FBGS)	Glass fibre reinforced plastic	1.0mm or 0.5mm	Need compensate	£152.6
FSA Strain Sensor (HBK)	polycarbonate	0.8mm	Need compensate	£89
FS62 –Strain Sensor (HBK)	Stainless steel	0.2mm 6mm	Need compensate	£159
Smart fibers	steel or aluminum	2-4 mm	Need compensate	£234

In summary, they all meet the sensitivity required for the measurement. One key parameter for TSMP is the diameter of the sensor as the sensor must fit within the physical space of the lid groove. SMW-01 with glass fibre reinforced plastic, FSA and FS62 offer sensors smaller 1mm in diameter which would allow to be fitted within the groove.

In addition, in terms of price the three chosen sensors are comparable. However, through communication with the manufacturer and in terms of the complexity of real procurement, the product of FSA from HBK was chosen as the measurement element for this project [110].

5.2 Test rig setup

To validate the collector groove deformation as TMSE a test rig was built with the components shown in Figure 5.2.

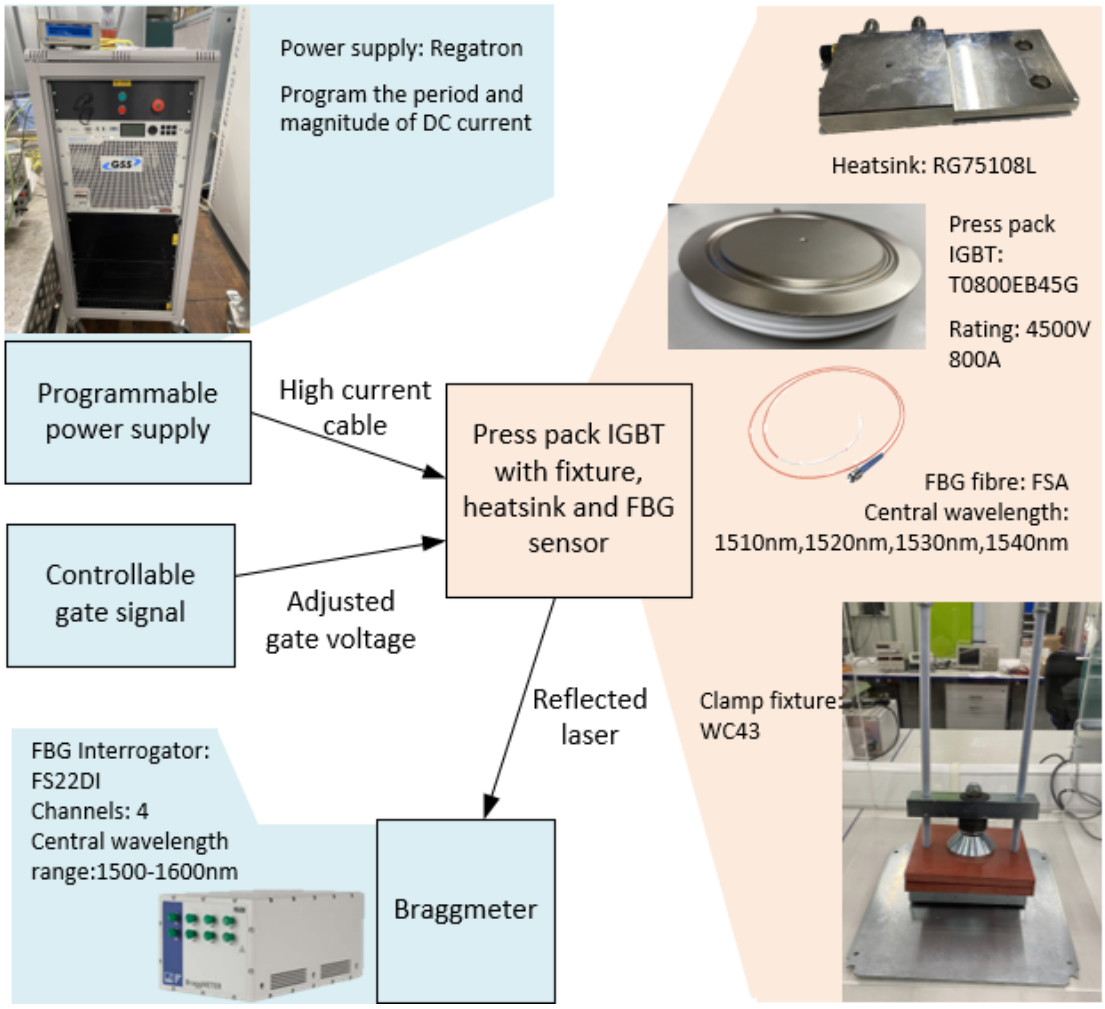

Figure 5.2 Schematic of collector lid

As shown in Figure 5.2, the commercial PP IGBT from Littlefuse (T0800EB45G) was used in this work. The rating current and voltage are 800A and 4,500V respectively. The PP IGBT that was used is an open device meaning the collector lid was not pressed (the lid fits within the module but to seal the device, the lid has to be pressed within the flange).

The open module was deliberately chosen so that later IGBT and diode chips can be rearranged. As an open module was used the device has no gas which is commonly injected in press packs. The inert gas is used to prevent degradation of the electrode due to oxidation. A pre-set pressure clamp was purchased (WC43) which can accompany up to 3PP IGBT modules and heatsinks. The clamp provides the required pressure and setup to apply an even pressure contribution. A detailed drawing of the clamp can be found in Appendix B. The PP IGBT is double sided cooled by the water heatsink (RG75108L). The dimension of the heatsink is shown in Figure 5.3.

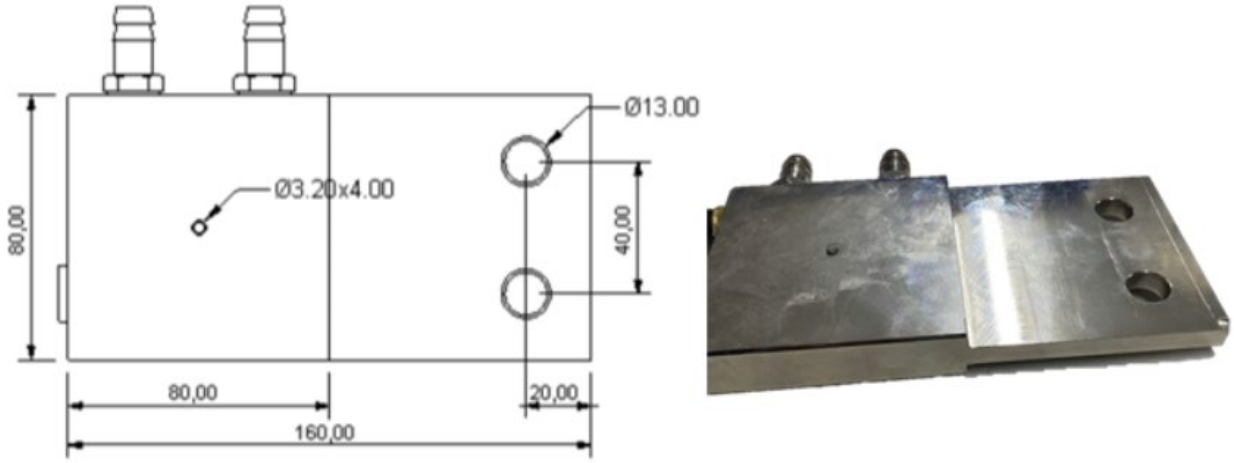

Figure 5.3 Dimension of heatsink

The heating current for the PP IGBT is generated by the Regatron programmable power supply which can program the period and magnitude of the injected DC current.

The FBG measurement system consists of 3 parts: the FBG fibre, the FBG interrogator and the Catman data acquisition software. Table 5-2 lists the specification of the selected FBG sensor and Figure 5.4 shows the schematic of the dimension of the FBG sensor and the detailed size of each grating.

The selected FBG fibre is based on the type of FSA strain sensor from HBK with customized parameter. There are three gratings of different central wavelengths each 45mm apart on the fibre, their central wavelengths are 1508nm, 1518nm and 1528nm, respectively.

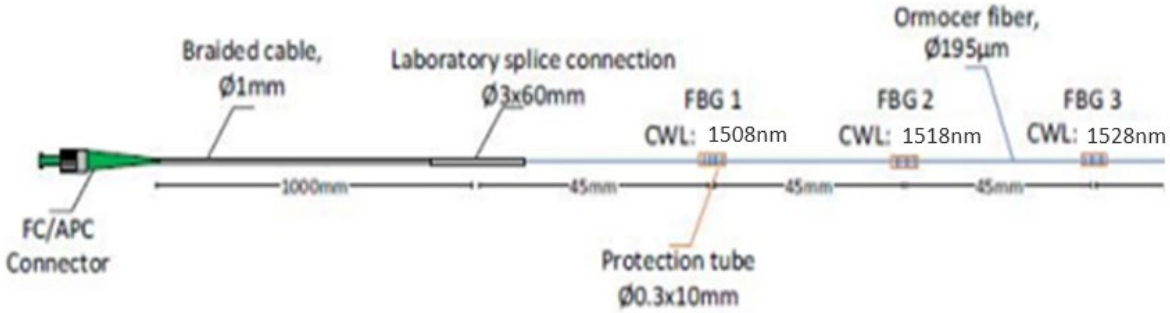

Figure 5.4 Schematic of FBG fibre with grating [110]

Table 5-2 Specification of FBG sensor

Elements	Specification
Central wavelength (nm)	1508,1518,1528
Cable type	Braided cable Ø1mm
Connectors	FC/APC
Braided cable length (mm)	1000
Braided cable bend radius	<5mm
Reflection	20% +/-3%
protecting tubes	Ø 0.3x10mm

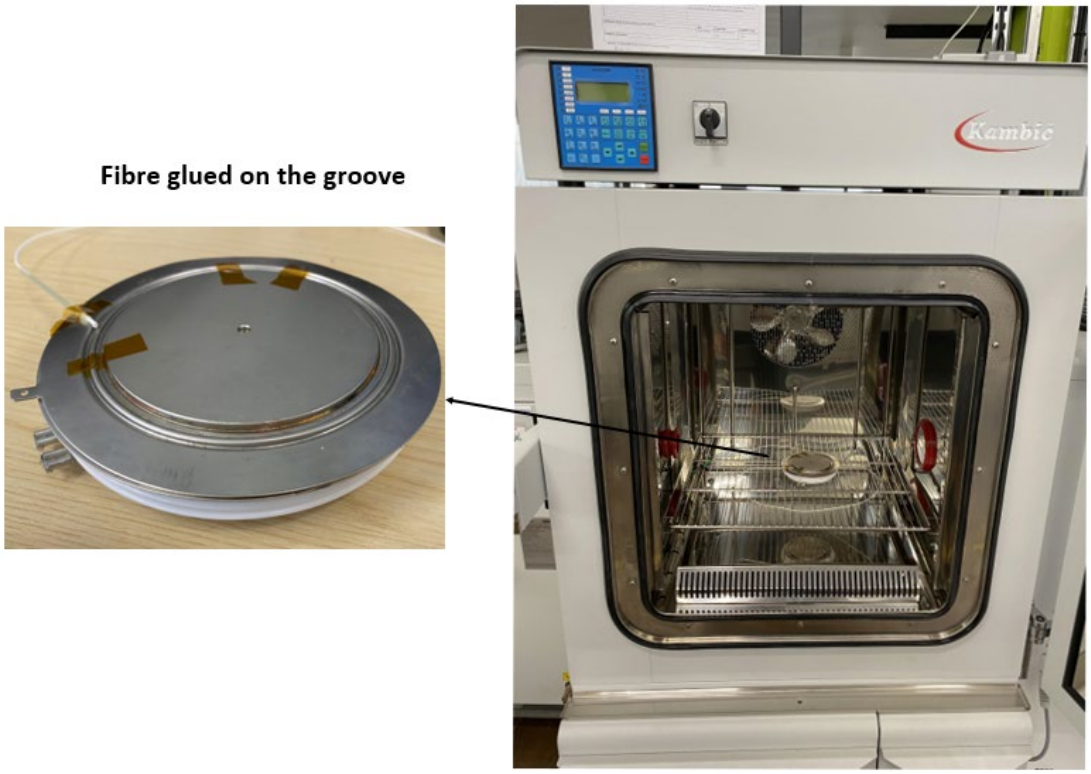

Figure 5.5 FBG fibre install on the lid groove with EP310 in the environmental chamber

In order to keep the FBG fibre in position, the fibre was wrapped around the groove, tightened to make sure that close contact is achieved with the inner lining of the groove and glue (EP310) was used to keep the fibre in position. Figure 5.5 shows the principles in applying the glue. Once the fibre has been put into position it was hold by sticky bands and glue was applied. Then the PP IGBT was put into an oven so that the glue hardens to apply its gluing force. The PP IGBT was kept in the oven for at least 2 hours under 150℃.

5.3 Experimental results and discussion

The work described in the Chapter 3 shows that thermal stress and clamping force result in deformation of the groove. Results have also shown that thermal stress produces more deformation compared to the clamping force. The relationship between temperature and grove deformation was also discussed. Figure 5.6 shows the principal relationships between the electrical, thermal and mechanical parameters that are all drivers of the groove deformation.

The current and voltage inside the PP IGBT produces heat during switching and conduction. This heat must be dissipated using heatsinks. As the heatsinks are attached to the outside of the PP IGBT, a heat flux path is created from the semiconductor chip to the top and the bottom of the PP IGBT collector and emitter lids respectively. Consequently, the material between the chip and the lids will have a temperature which depends on the thermal impedance paths. Due to manufacturing intolerance of press packs some IGBT chips are better cooled than others. It is also well known that chips that are not thermally well connected will become hotter. This is because the i-v characteristic of IGBT switches is changing with temperatures. Consequently, IGBT chips that are less thermally connected will produce higher temperatures compared to those who are better connected thermally. Furthermore, in case an IGBT chip has failed in press packs they most commonly become short-circuit. That means that this chip will produce most heat compared to all other chips.

It is also known that the produced heat in the IGBT that travels along the different materials sandwiched between the chip and the lid impacts on the physical dimensions of the material. The materials used in PP IGBTs have all a positive temperature coefficient meaning when exposed to higher temperature the material physically enlarges in size. Enlargement of adjunct materials leads to deformation and mechanical

stress between the different materials. Deformation and stress will change the thermal contact between materials. As thermal contact worsen, chips are exposed to more heat which results in changes of electrical parameters worsen the performance of the IGBT chip which in effect increases the chip temperature even more, producing even bigger deformation and stress. As Figure 5.6 shows the whole system shows a positive feedback-loop meaning that any change results in an accelerated degradation in the system which ultimately results in a short-circuit. As previous chapters have shown all of the accelerated processes show up in the lid groove deformation.

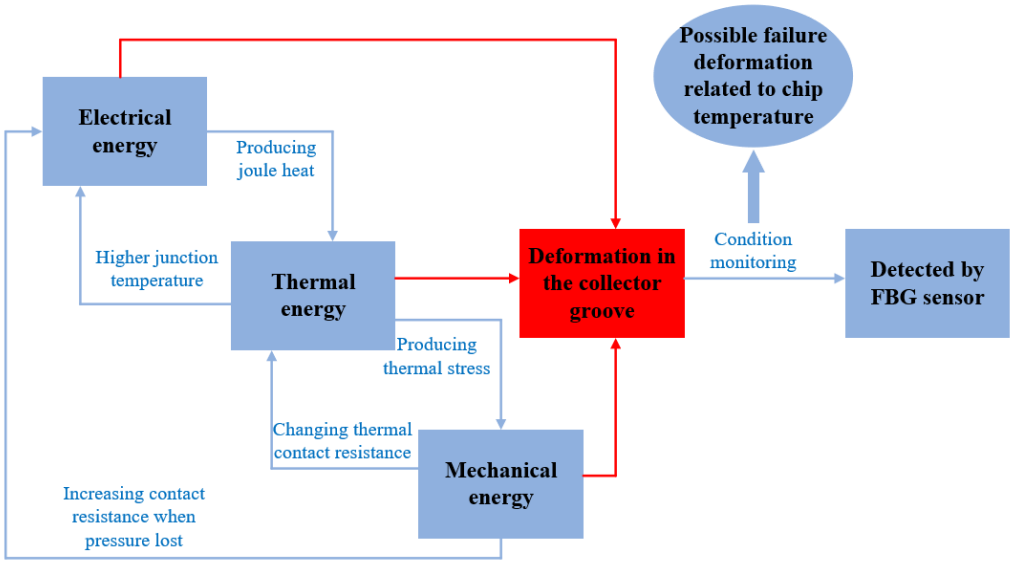

Figure 5.6 Diagram of lid groove deformation affected by electrical/temperature and mechanical energy

Measuring deformation is measuring a mechanical parameter and mechanical parameters have normally long time constants (seconds to minutes). These time constants are much larger compared to those affecting the electrical characteristics of power modules. It is therefore necessary to consider whether measuring the groove deformation can detect module faults in time. The diagram 5.7 shows the relationship between the bottom temperature and the change in temperature of the groove when the collector lid is subjected to heat. As can be seen from the graph, the time difference between the two temperature changes is in the order of milliseconds. In addition, the unique short-circuit failure mode of the PP IGBT [70] ensures that the PP IGBT can continue to operate for a period of time under a short-circuit fault, so that a module failure can be detected in time for replacement.

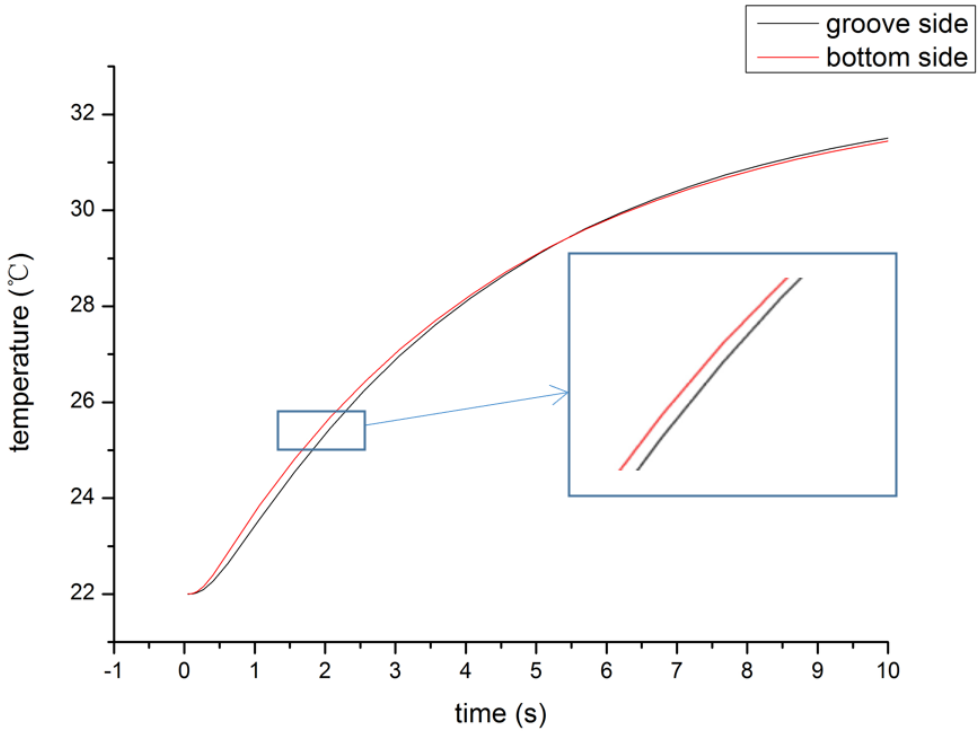

Figure 5.7 Temperature change relationship between the bottom side and groove side of collector lid

5.3.1 Full module deformation test

Experimental evaluation is carried out by measuring the collector groove deformation through a series of tests. The initial test is implemented to see the performance of the deformation measurement ability of FBG sensor.

The basic schematics of the test circuit is presented in Figure 5.8, the FBG fibre is well glued around the collector lid groove for monitoring the deformation, the heat load of the entire system is generated by providing a constant current I_{heat} through the chips, the heatsink is fixed to the sides of the PP IGBT module by means of locating pins, but no chiller is connected to the heatsink (no water cooling). Thermal couples are attached to the lid groove and close to the operating chips to record temperatures. Figure 5.9 shows a picture of the experimental test setup. Additional Figures of the FBG measurement system are presented in the Appendix C.

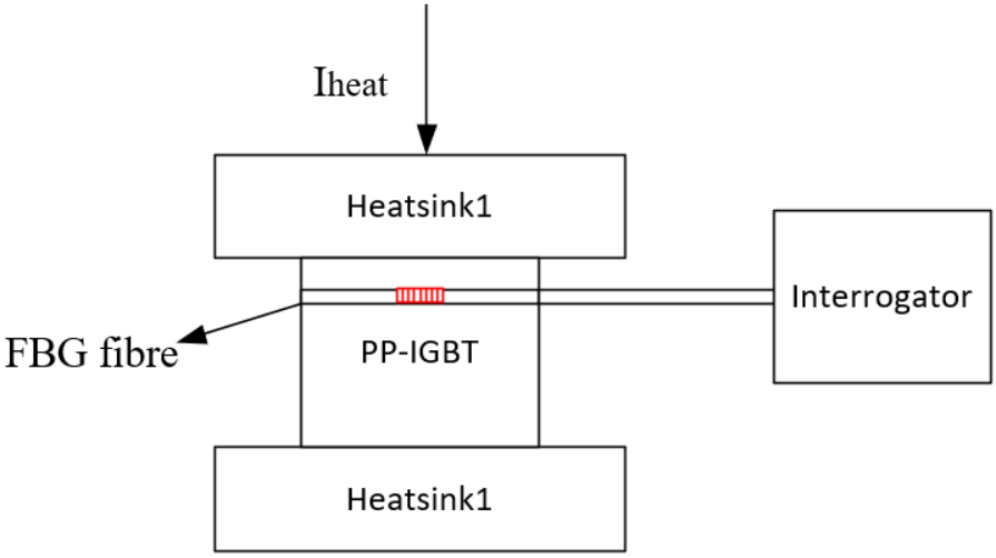

Figure 5.8 Schematic diagram of deformation measurement system

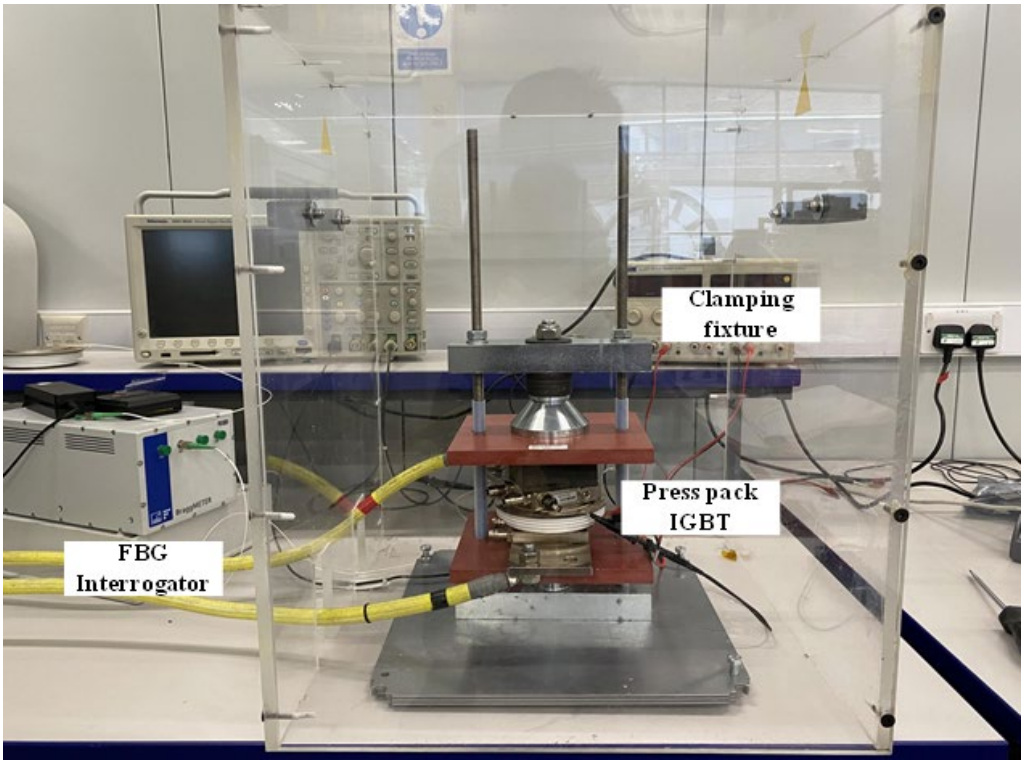

Figure 5.9 Experimental test setup for PP IGBT deformation measurement

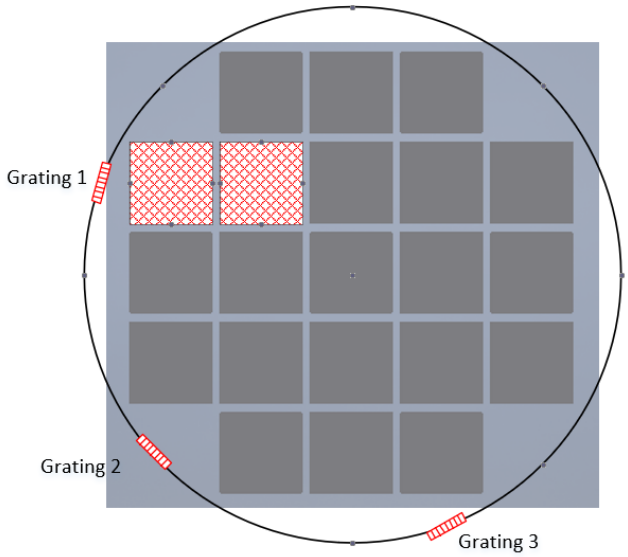

(a)

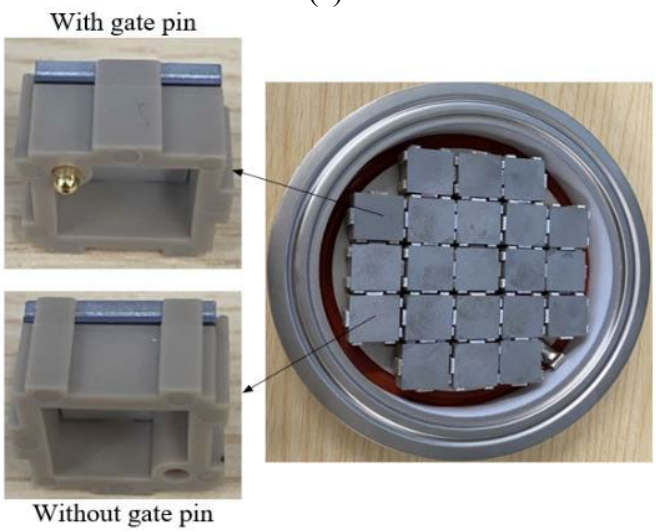

(b)

Figure 5.10 Experimental schematic for one module (a) Operation IGBT chips position (b) Gate pin manipulation of IGBT sub-module

To emulate operation of a failing PP IGBT the chips within the PP IGBT have been altered. The module normally contains 7 diode chips and 14 IGBT chips. By retaining the 7 internal diodes and removing the 12 gate pins from the remaining 14 IGBTs, a situation where only two IGBT chips are operating is generated. Figure 5.10 (a) and (b) show that the position of the two working IGBT chips within the module and the removal of the gate pins, respectively. Also, there are three gratings of different central wavelengths on the same FBG sensor fiber and their positions are also shown in Figure 5.10 (a).

The result of the deformation characterization of grating 1 which is most close to the operated chips is shown in Figure 5.11. The PP IGBT module is subjected to the heating current of 60A, which corresponds to the heat load of around 144W, the clamping force is 30KN applied by pre-clamped fixture. In addition, the gate control voltage was varied from 12V to 18 V to produce different heat load conditions. Measurement was conducted for a 5-minute period. The temperature change for grating 1 is shown in Table 5-3, and after temperature compensation based on (5.4), the deformation result is shown in Figure 5.11. As observed, the deformation on the groove is reduced as the heat load decreases. Figure 5.12 presents the deformation results of the three gratings at different gate voltages strain 3, 2 and 1 represent grating 1, 2 and 3, from which it can be seen that each set of results has the same trend and the deformation of both grating 2 and grating 3 is less than grating 1, due to their different positions. This provides a reference for determining the approximate area of the faulty chip.

Table 5-3 Temperature change after heating period

Group	Before heating (°C)	After heating (°C)	ΔT (°C)
Gate voltage at 12V	20.0	43.6	23.6
Gate voltage at 15V	20.9	40.3	19.4
Gate voltage at 18V	21.3	39.3	18.0

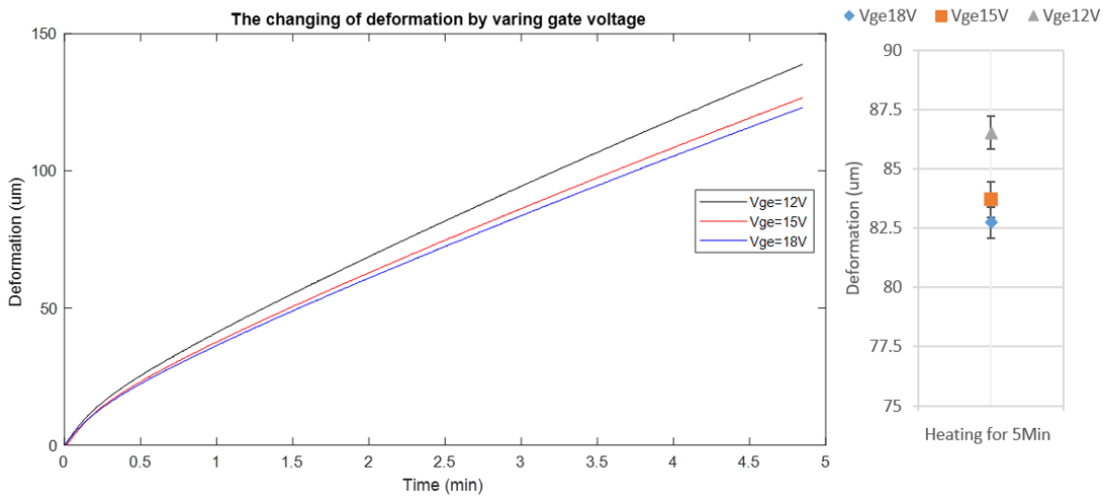

Figure 5.11 Experimental results for deformation measurement under various gate control voltages

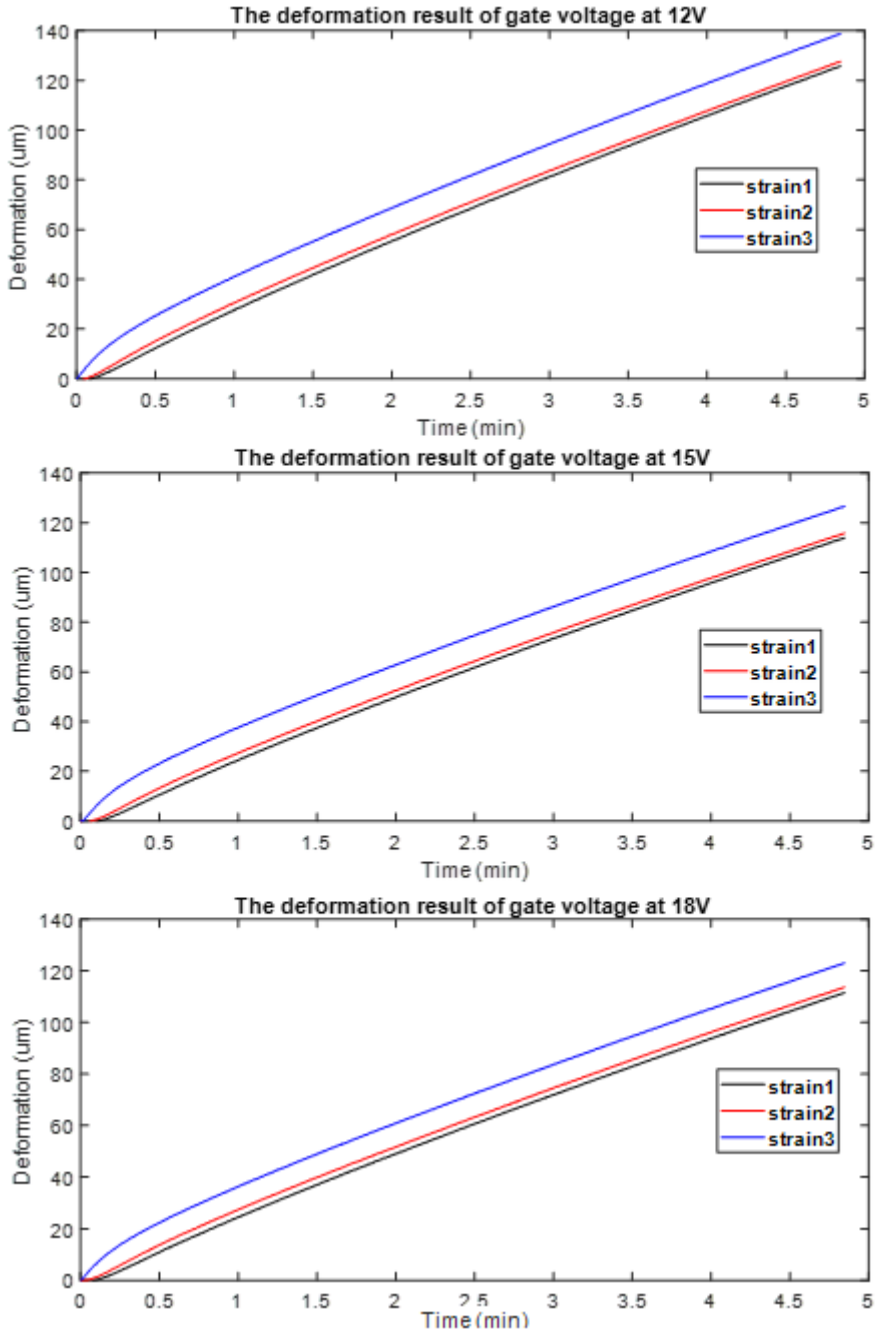

Figure 5.12 Deformation results of 3 gratings based on different gate voltage

During the measurement of the deformation, the chip temperature during the switching event of the IGBT module cannot be determined directly. That is due to the influence of the thermal mass of the lid and the heat delay from the chip to the groove.

For most practical applications of PP IGBTs applied to HVDC, this is not a major problem. This is because in this applications junction temperature fluctuations are less likely to be generated, as they are usually operated for long periods of time at the same average collector current. Therefore, in the above experiments the current is injected

through a constant current source simulating the relatively long-term constant current operation. Figure 5.13 shows the transmitted power of a HVDC transmission line from UK to France from 15.02.2019 to 15.03.2019 [121] and it can be seen that the transmission power fluctuates little in the whole month, as the voltage scale value is essentially constant in HVDC systems, this means that current fluctuations are also small. [120].

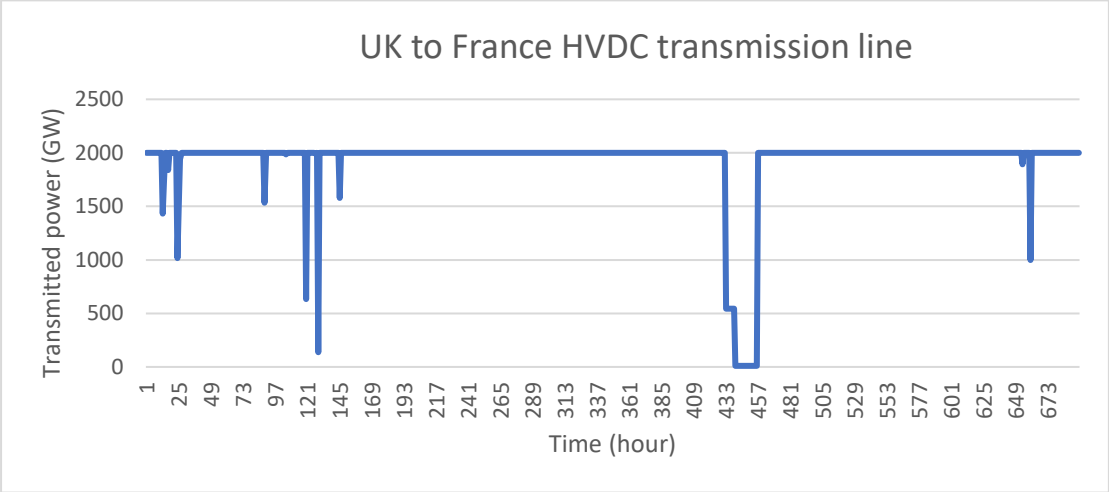

Figure 5.13 HVDC transmission line transmitted power

To further investigate the variation of PP IGBT collector groove deformation under different current conditions, deformation was observed by varying the input current but keeping the gate voltage at a constant of 15V. Experiments were conducted at 50A, 70A and 80A. Again, each measurement is performed for 5 minutes which is same as before. The temperature record is shown in Table 5-4.

Figure 5.14 shows the deformation measurement results based on the same operation chips position and gratings arrangements as Figure 5.10 (a) and the temperature compensated results after heating phase.

As can be seen from the results, with increasing input power the measured deformation increases accordingly. It is worth noting that in the absence of a cooling effect, a time frame of 5 minutes was chosen as it was difficult to achieve steady state inside the safety-protected cover and at room temperature. So data shown are on the slope. If tests could have been conducted for longer the slope would become smaller until steady state is reached.

Table 5-4 Temperature change after heating period

Group	Before heating (°C)	After heating (°C)	ΔT (°C)
Input current at 50A	19.0	32.1	13.1
Input current at 60A	20.9	40.3	19.4
Input current at 70A	23.0	46.2	23.2
Input current at 80A	24.0	55.7	31.7

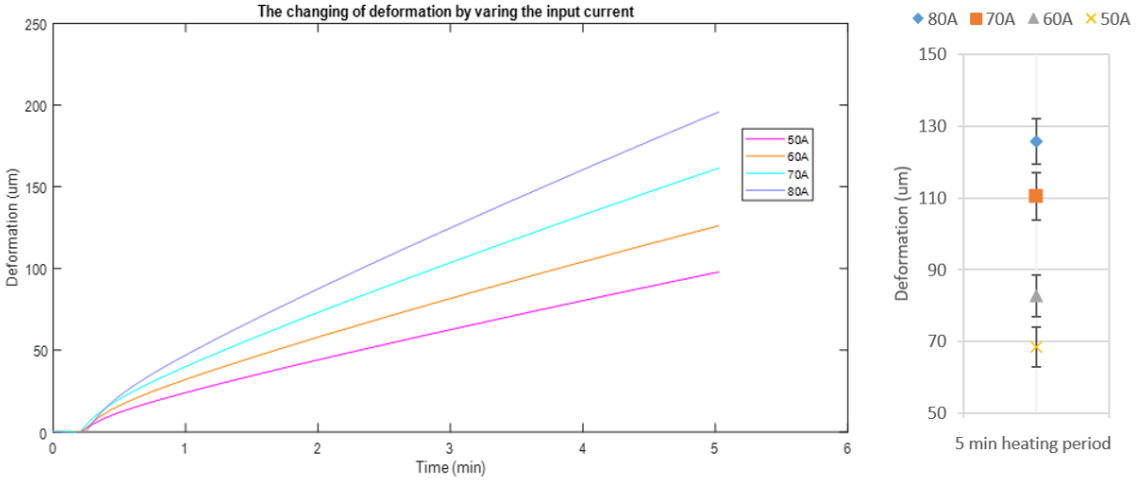

Figure 5.14 Experimental results for deformation measurement under various input current

The results obtained so far are based on static heat power by either varying the collector current or the gate-emitter voltage which is not a true representation of detecting a failure when in operation.

According to the literature [81], a PP IGBT module was subjected to power cycling under constant current, and the collector voltage suddenly underwent a thermal breakdown and it rapidly changing to 10 V from the beginning of the cycle to 6690 cycles, indicating that the faulty module was instantaneously subjected to far more input power than before. The result of the collector voltage change under power cycling is shown in Figure 5.15.

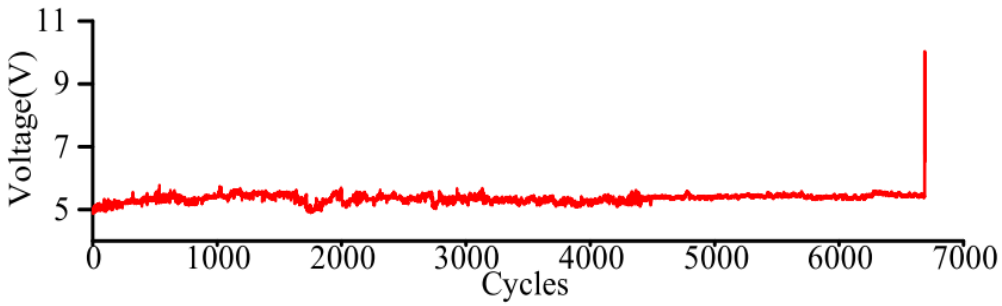

Figure 5.15 Voltage changing of PP IGBT during power cycling [81]

Therefore, in order to emulate this behavior the PP IGBT was operated at two different collector currents. For the first 50 minutes it was operated at 8A to represent normal operating conditions as 8A produces less heat power. At 48 minutes the current was increased to 20A emulating the failure of chips. Results of this experiment are obtained and shown in Figure 5.16.

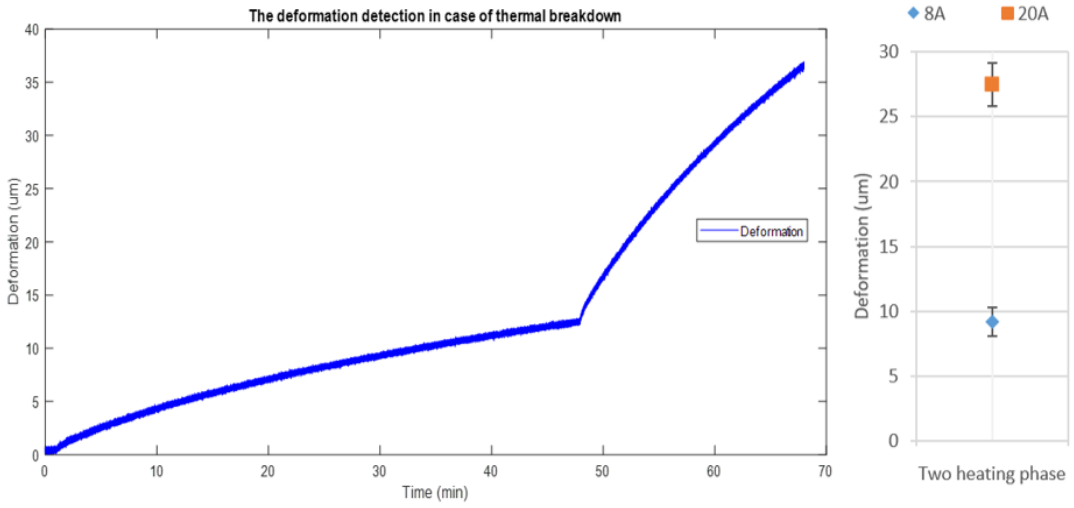

Figure 5.16 Experimental results for deformation measurement with increasing input current

Table 5-5 Temperature change at different heating phase

Group	Before heating (°C)	After heating (°C)	ΔT (°C)
Input current at 8A	18.8	20.1	1.3
Input current at 20A	20.1	24.0	3.9

Table 5-5 shows the temperature change at different heating phase. As can be seen from the figure, the rise in heat leads to a nearly instantaneous increase in deformation. This clear change can be used to determine that a PP IGBT module has a short-circuit chip. This figure shows that the proposed TMSP is detecting failing chips.

5.3.2 Experimental validation for two modules deformation detection

One of the most superior advantages of FBG sensors is that they can achieve multi-point measurements through a single optical fibre. This advantage is particularly suitable for applications using PP IGBTs.

This is due to the fact that the output of a Bragg grating is wavelength, which is an absolute parameter that is not affected by the total amount of light source or the loss of the fibre. Distributed measurements can therefore be achieved by associating each grating with a specific spatial location.

The upper limit on the number of gratings per fibre depends on the operating wavelength of each grating and the wavelength width of the input light source. Currently 20 or more grating elements can be multiplexed in a single fibre [110].

The same interrogator can multiplex the reflected wavelengths of FBG fibres, meaning that one interrogator can monitor a stack of series connected PP IGBT modules at the same time.

The performance on the simultaneous measurement of two lid groove deformations in a single FBG fibre were carried out. Figure 5.17 (a) shows the test circuit and the distribution of the IGBT operating chips inside the two modules and Figure 5.17 (b) shows the number and positions of gratings. In the test, one module has all 14 IGBT chips operating deemed as normal operation, the other module emulates a failed operation, with only two IGBT chips carrying the current. The picture of the experimental setup for two modules test is shown in Figure 5.18.

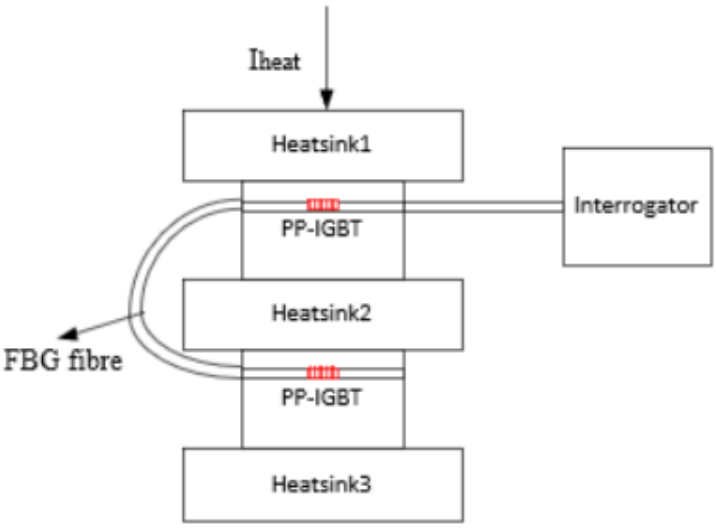

(a)

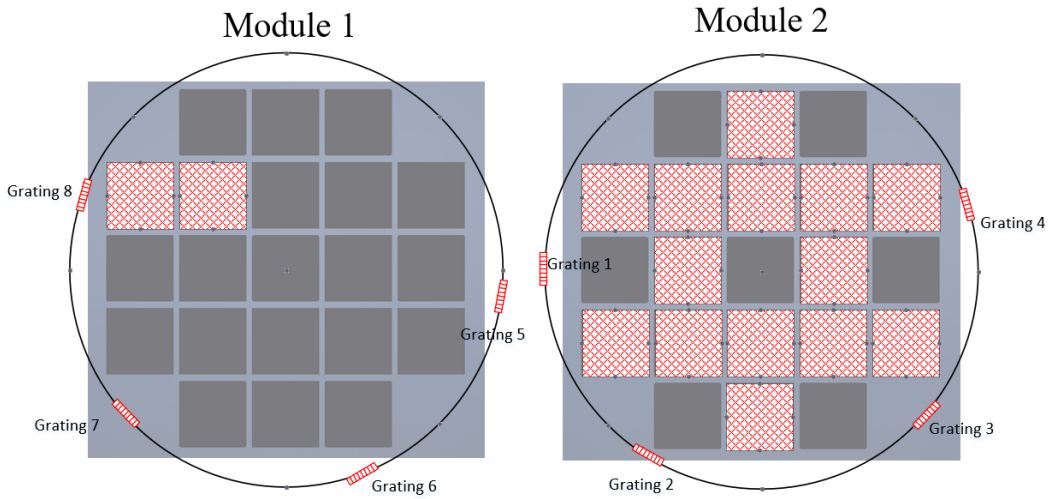

(b)

Figure 5.17 Experimental schematic for two modules (a) Two modules test circuit (b) Distribution of IGBT chips inside the two modules

Table 5-6 Temperature change after heating

Group	Before heating (°C)	After heating (°C)	ΔT (°C)
Grating 1	20.1	29.0	8.9
Grating 8	19.8	42.0	22.2

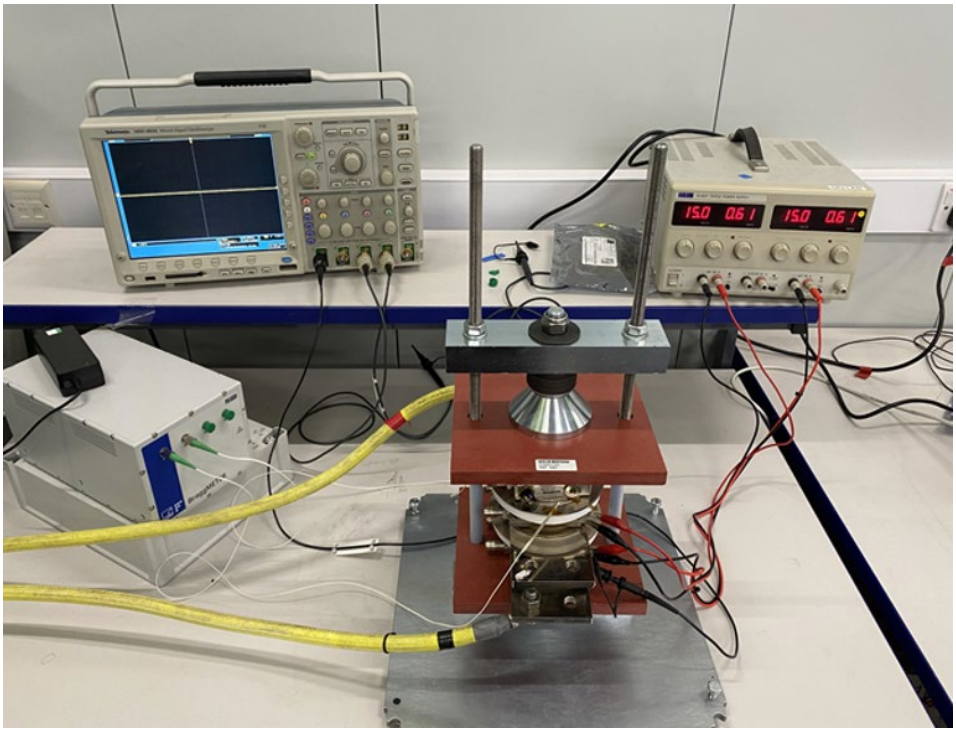

Figure 5.18 Experimental test setup for two PP IGBTs

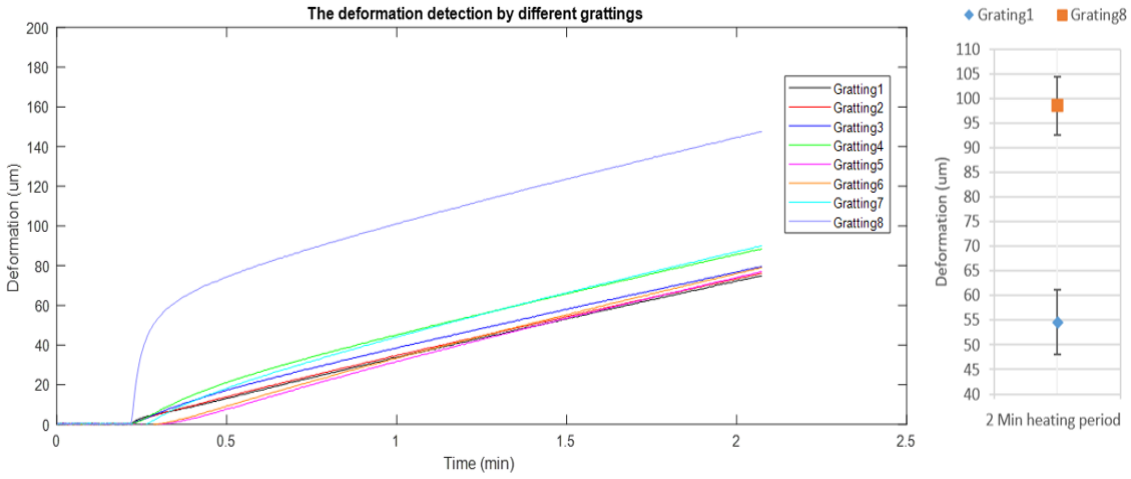

Figure 5.19 Experimental results for deformation measurement of two modules

The result of the deformation characterization for the two modules and the temperature compensated results for gratings 1 and 8 are shown in Figure 5.19. The temperature change recorded for grating 1 and 8 is shown in Table 5-6. The gratings are selected since grating 1 is on the module operated under normal condition and grating 8 is the sensor closest to the chip carried current on the module that simulates failure.

The total of eight gratings in one FBG fibre is used, four for each module, and details of the grating dimensions are shown in the Appendix D. The two modules are subjected

to a heating current of 80A with the same gate voltage of 15V. The clamping force is 30KN which is the pre-set rated clamping force.

The measurements are performed for a duration of 2 minutes. It is worth mentioning that similar to the previous experiments, three heat sinks were used to connect the PP IGBT modules and fixture for the dual module deformation measurements, but without the effect of the chiller. Therefore, a shorter time range of 2 minutes was chosen to record data without the cooling as it can clearly show the differences in the slopes.

Results in Figures 5.19 show clearly that the deformation of the grating 8 closest to the two faulty chips is much larger than the rest. In addition, with the exception of the grating 8 close to the failed chip, the remaining seven gratings detected a range of deformation that was relatively close.

The results of gratings 4 and 7 show the slight difference compared to the other 5 gratings. This is because grating 7 is the closest sensor on the fault module to the IGBT chip carrying current apart from grating 8, while grating 4 is positioned closer to the area of the through-current IGBT chip than the other three gratings on the normal operation module. By assigning different wavelengths to the gratings at different locations, it was possible to obtain information about the failed module and to determine the location of the failed chip in general.

Similar to the experiment before, two currents were applied to emulate the failure of a device. First a current of 30A was applied until 1.7minutes. Then the current was increased to 70A to emulate higher heating power. This jump is to indicate a failing device chip (e.g. short-circuit). The gate-source voltage was kept constant to 15V and the clamping force was 30KN.

Table 5-7 Temperature change at different heating phase

Group	Before heating (°C)	After heating (°C)	ΔT (°C)
Grating 1 at 30A	20.1	22.0	1.9
Grating 1 at 70A	22.0	28.2	6.2
Grating 8 at 30A	20.3	23.4	3.1
Grating 8 at 70A	23.4	43.4	20

Like in the experiments before the heatsinks were not cooled by water and the temperature change is shown in Table 5-7. Figure 5.20 shows the results of the measured deformation. From the figure, it can be seen that the deformation value of the faulty module rises steeply with the transient increase of current, and the difference between the faulty and healthy modules can be clearly seen. The experiment verifies the feasibility of using the same fiber for multiple modules.

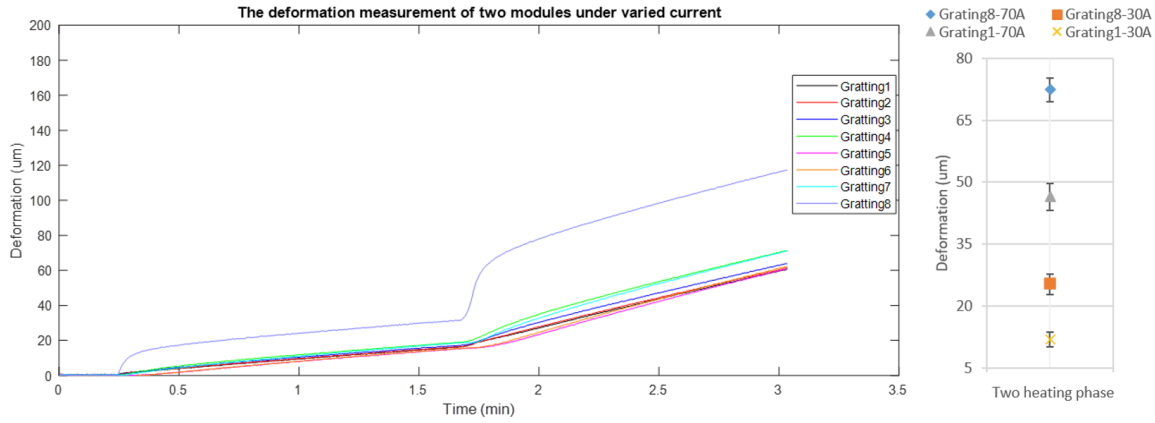

Figure 5.20 Experimental results for deformation measurement of two modules under varied current

5.3.3 Results with water cooled heatsinks

So far, the heatsinks used in the experiments were not water cooled. This was done intentional to run experiments at lower and safer currents. The choose PP IGBT operates at much higher currents and to compare deformation between simulation results and practical results a larger current is required and to cool the module water cooling is required too.

Figure 5.21 (a) shows the test circuit and (b) shows the distribution of the IGBT operating chips inside the module and the number and the position of the gratings. In this test, the module with all 14 IGBT chips were used and three different collector currents were applied: 280A, 420A and 560A. The clamp force was 30kN and the gate source voltage was 15V. A valve determines the flow rate and a flow meter is placed at the inlet pipe. A thermocouple was also placed at the inlet pipe to monitor the inlet temperature of the water. The picture of the experimental setup for water cooling test is shown in Figure 5.22.

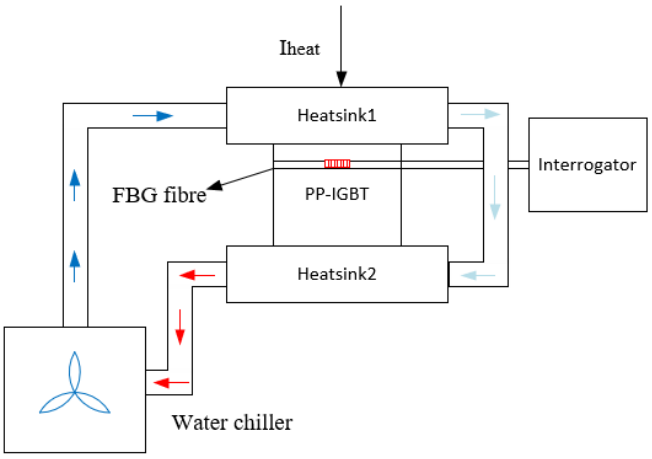

(a)

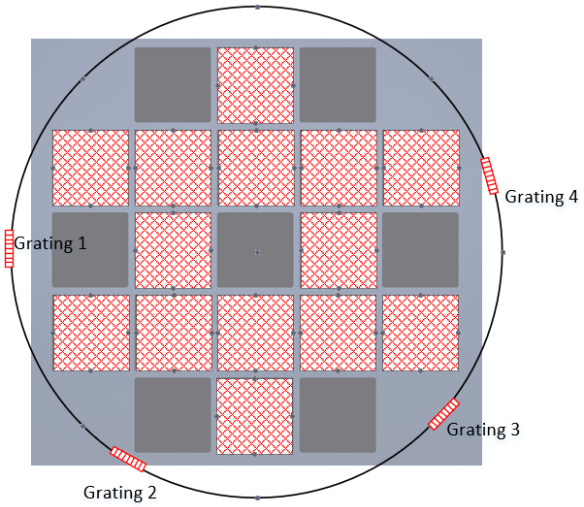

(b)

Figure 5.21 Experimental schematic with heatsink (a) Water cooling test circuit (b) Distribution of IGBT chips inside the module

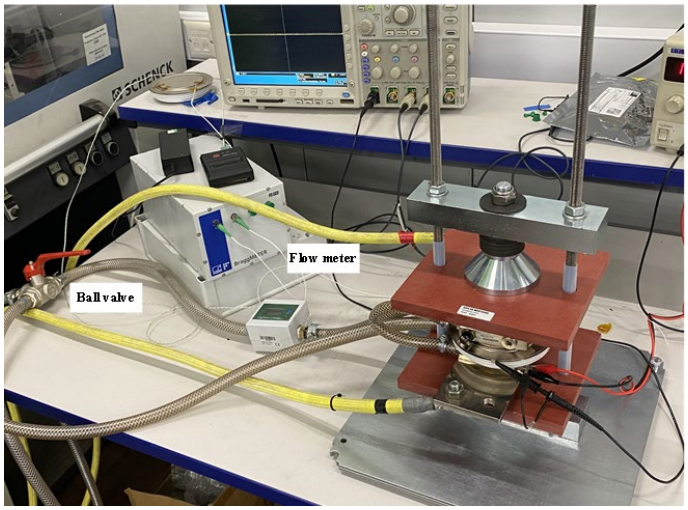

Figure 5.22 Experimental test setup for water cooling deformation measurement

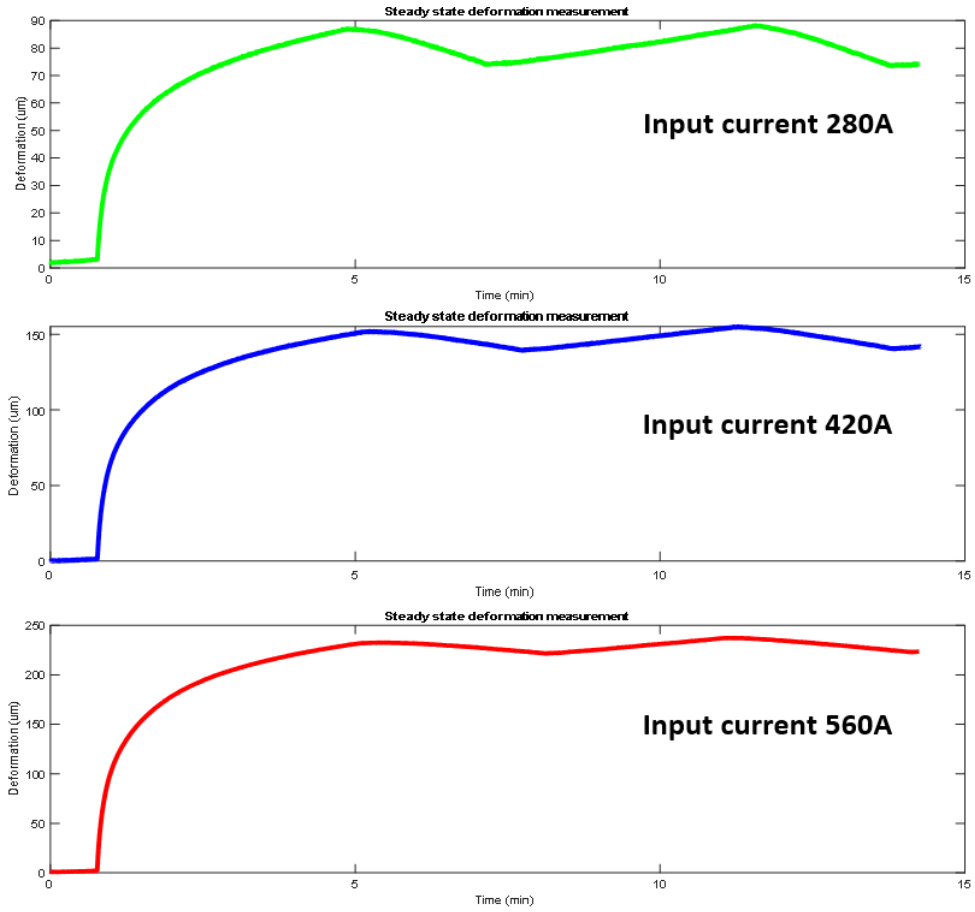

Figure 5.23 Experimental results for deformation measurement of water-cooled test

Table 5-8 Temperature change at different heating phase

Group	Before heating (°C)	After heating (°C)	ΔT (°C)
Input current 280A	16.1	26.5	10.4
Input current 420A	16.2	33.7	17.5
Input current 560A	16.1	43.3	27.2

The result of the deformation characterization for grating 4 with the water-cooling effect is shown in Figure 5.23. The flow rate is set at 12L/m, and the chiller outlet temperature is set as 20℃.

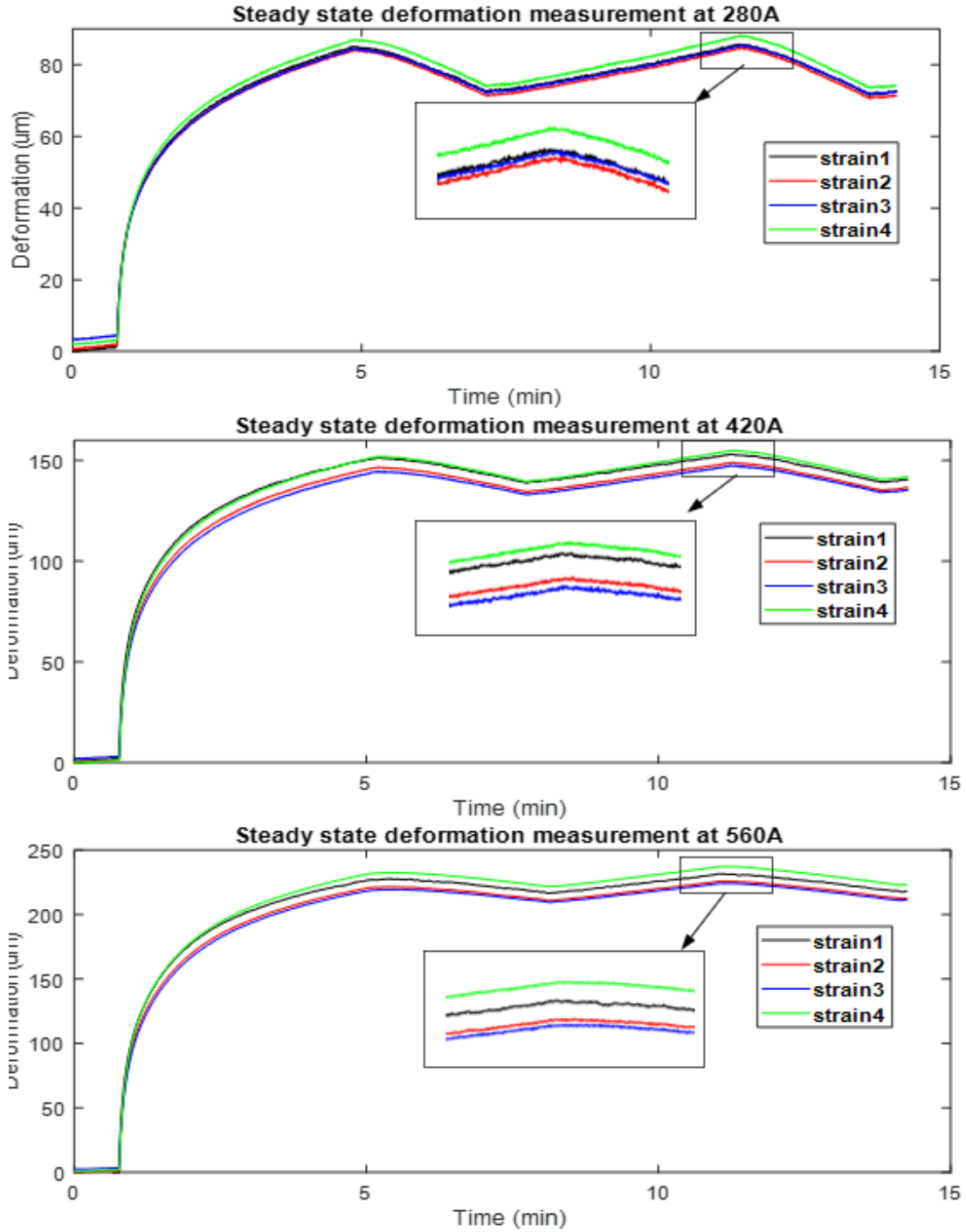

Figure 5.24 Deformation results for water-cooled test of 4 gratings based on different current

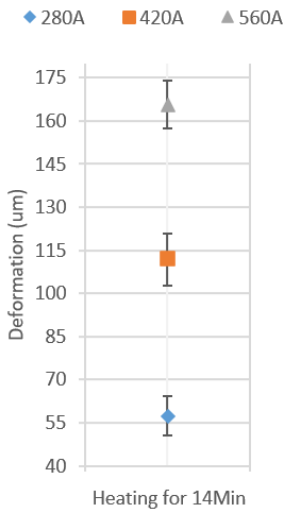

Figure 5.25 Experimental results for deformation measurement of water-cooled test with temperature compensated

The experimental results were obtained by applying current for 14 minutes at a laboratory room temperature around 20°C in order to reach the steady state. The temperature change is shown in Table 5-8. The results with temperature compensation are shown in Figure 5.25. The average steady state values of the deformation for the three different input currents are: 57 μm, 112 μm and 166 μm, respectively. Although there are fluctuations in the measurements, they are all within 5% of the steady state value. The reason for this fluctuation is that the inlet water temperature to the heatsink is changing. This changing is due to the chiller operation mechanism which works to regulate the outlet water temperature in accordance with the internally detected inlet water temperature.

Figure 5.24 shows the deformation results of 4 gratings based on different current, it clearly shows that the results of 4 gratings has very close trend, this is because the IGBT chips are all carrying current and evenly distributed. The slight differences in the measurements of the different gratings may be due to the different contact levels of each grating.

5.3.4 TMSP as an early warning system

As can be seen from the Figure 5.23, the difference in deformation values for different input currents varies uniformly at a cold-water flow rate of 12L/min. Equation 5.5 expresses the amount of heat carried away by the module under the action of water cooling. Where Cw is specific heat capacity, the Mw is the mass and ΔT is the change

of temperature.

$$E = Cw \cdot Mw \cdot \Delta T \tag{5.5}$$

Due to the limitations of the experimental equipment, the maximum injected current can only up to 560A, therefore a finite element simulation was carried out in order to obtain the steady state deformation values for the injected rated current under the same heat dissipation conditions.

Figure 5.26 shows the comparison between the simulated and experimental results for input currents of 280A, 420A and 560A under similar thermal conditions, it is worth pointing out that the difference between the measured deformation values in the experiment and the simulation may be caused by the imperfect contact between the FBG fiber and outer lining of the groove, and the error quantity is around 15%. However, it shown that the trend of the experimental and simulated deformation is consistent at different input powers. As the rated current of the PP IGBT is 800A but the current source was limited to 600A deformation can be extrapolated using the trendline shown in Figure 5.24. At 800A the deformation is 259 μm assuming 20℃ inlet water temperature. As such, for different currents a deformation value can be found so long the current applies for a given period so that steady state can be reached. Again, in HVDC transmission the current profile does not vary too frequently like for example in electric drives applications [104].

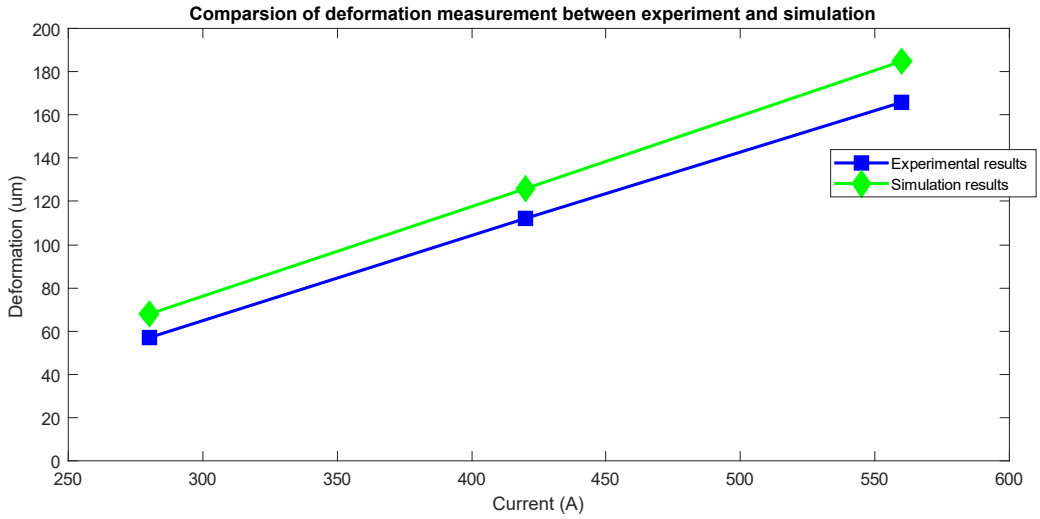

Figure 5.26 Comparison between experiment results and simulation results

In order to establish an early warning system the same principle as applied in TSEPs is used. For example, when measuring the collector-emitter voltage as condition

monitoring for conventional packaged IGBTs, the difference between the measured and trendline values are used. If the difference exceeds a threshold a warning signal [119] is produced. The threshold activating a warning signal is an error of [119]:

$$\Delta Vce(\%) = \frac{1500}{Irate} \tag{5.6}$$

Like TSEPs when PP IGBTs start degrading, the trendline will differ from the baseline. In HVDC applications current and water temperature are measured so TSMP constantly monitors the current and inlet temperature. When both have been constant for a while (steady state) the measured deformation is logged as reference value and compared with the baseline value. If both values differ significantly one can conclude that the PP IGBT starts failing.

The percentage value of the warning threshold depends on many factors and is out of scope in this research. As the deformation mainly come from thermal effect caused by the injected current, for simplicity using (5.6), assuming the rated current of 800A the threshold for the deformation is 1.875%. Thus, if the deformation increases from 259 μm to 263.86 μm a warning is provided. However, other percentages can be chosen.

5.4 Summary

In this chapter, the FBG sensor used in the experimental measurements is first selected based on fiber dimension and cost. Then the experimental platform was built based on the FBG measurement system. The internal configuration and external conditions of the module were adjusted according to different experimental purposes. The feasibility of using collector groove deformation as the new indicator for monitoring the health status of PP IGBT modules was verified. The main research outcomes in this chapter are:

1. The feasibility of using FBG fiber optic sensor to measure the collector groove deformation is verified. The module status can be determined by measuring the deformation when thermal breakdown occurs under average current input.

2. The use of FBG fiber optic sensors enables the simultaneous monitoring of multiple modules and the determination of the location of the faulty module and the approximate area of the faulty chip.

3. Validating deformation values of PP IGBT module operating at full power with simulation results.

Chapter 6 Conclusion and Future Work

6.1 Conclusion

Power electronics play an important role in power systems and are a vital part of the process of transmitting and controlling energy. They are used in many important applications of national importance, such as HVDC and wind power. In HVDC applications PP IGBTs are used to control the amount of energy transmitted. Due to their unique packaging structure, PP IGBT have many advantages over conventional bond wire IGBT modules, such as their double-sided heat dissipation, short-circuit failure mode, high power density and high reliability. PP IGBTs are also increasingly being used in other applications, such as high-power drives.

Although PP IGBTs show good reliability, they are also prone to failure. This can be a particular challenge in HVDC applications, in which hundreds of PP IGBTs are connected in series and a catastrophic failure of a single module could result in the complete loss of energy transfer to suburbs or towns. As such, monitoring the health of PP IGBTs is essential to ensure that degrading modules can be changed before they fail. In this thesis, health monitoring devices for PP IGBT modules were investigated and compared. PP IGBT modules are electrically and thermally contacted by pressure instead of a bonding wire. In addition, PP IGBT modules achieve high power densities based on the internal parallel connection of multiple chips. Some condition monitoring methods for conventional IGBT modules are not applicable to PP IGBT modules. Therefore, this study investigated a bespoke health condition monitoring circuit for PP IGBTs as well as monitoring circuits for measuring the health of conventional IGBT modules that can be adapted to PP IGBTs. The investigation led to the development of a new concept for the health monitoring of PP IGBTs, namely the temperature sensitive mechanical parameter (TSMP). The TSMP method monitors the condition of PP IGBT modules via a new indicator: deformation of the lid groove. As such, the thesis describes the development of a measurement system by focusing on how to detect deformation at the groove of the PP IGBT module and how the deformation is linked with the health of the power module.

High-fidelity physical models of two PP IGBT modules were built to simulate the variation of the physical parameters of the PP IGBT modules under average current injection. From the finite element simulation, it was concluded that the deformation at

the collector groove changes the most with clamping fixture pressure and internal chip power dissipation, while being easily measurable from outside the module. The simulation results showed that the heat generated by the internal chip due to losses has a greater influence on the deformation than external pressure. At the same time, the area and approximate location of the faulty chip can be derived from the deformation values at different points along the groove.

Different sensor types were investigated for detecting deformation at the groove. The FBG sensor was selected to measure the collector groove deformation, as it has the advantages of high sensitivity, immunity to electromagnetic interference, the possibility of distributed measurement and a relatively low cost. This type of sensor can achieve high sensitivity around 1pm/με with high accuracy.

A test platform was built based on the FBG measurement system. The experimental results validated the conclusions of the finite element simulation. By varying the input current, IGBT chip positions, gate-source voltages, clamping forces and cooling temperatures, thermal stresses were emulated in a PP IGBT module, and the relationships between deformation at different points along the groove using FBG with the chip temperatures and clamping forces were recorded and discussed. In addition, the superiority of the FBG sensor for distributed measurements was also practically verified. Finally, the deformation range for normal operation of PP IGBT modules with water cooling effect is investigated, for the 800A rated PP IGBT module, additional maintenance was required when the deformation exceeded 259 μm.

6.2 Future work

6.2.1 Installation process improvement

Based on the work in this thesis, the proposed method for detecting deformation has the potential for further development. In order to make TMSP with FBG more applicable to practical applications, it is desirable to bring the fiber and the collector into better contact than just using a professional adhesive to connect these two objects. In addition, although there is enough space in the collector groove for installing the FBG fiber, better results could be extracted when making a bespoke thin slot in the middle of the collector lid to ensure better contact between the FBG sensor and the current collector lid.

6.2.2 Measurement improvement

The gratings on the FBG fiber should be designed according to the size of PP IGBT modules, which can ensure a better monitoring of the area of the faulty chip. Also, for distributed measurements, an extra layer of coating should be added outside the braided cable, considering the protection of non-sensitive areas of the fiber and the reliability of long-term use. Finally, the proposed method should be applied to other applications such as electric drives.

Appendix A

FE simulation for Toshiba model

The finite element simulation of the Toshiba PP IGBT is divided into two different models. Figure A.1 shows the schematic diagram of the first model, which is unique to the general PP IGBT structure in that it has a single upper Mo plate.

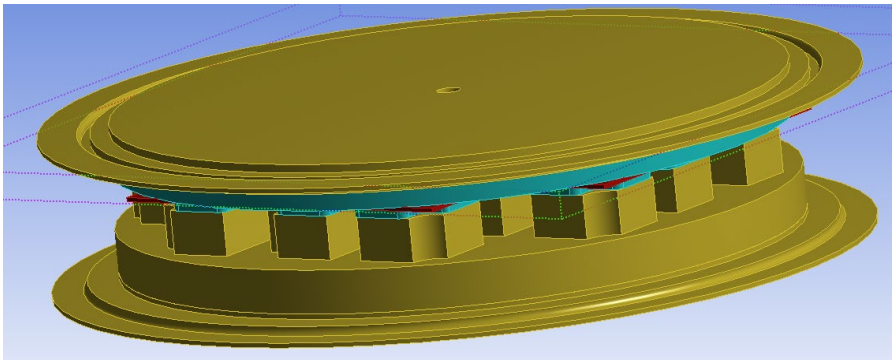

Figure A.1 Geometry model of Toshiba with whole upper Mo plate

Figure A.2 (a) illustrates the temperature distribution in the static thermal and (b) shows the deformation results on the lid. Based on the normal operation feature of PP IGBT, each IGBT chip has the loss around 100W under rated current condition. According to the manual sheet of PP IGBT, the power loss of each diode chip can be assigned as 30W and the clamping force is 13.5KN. And the room temperature is set at 22 °C. The results lead to similar conclusions, with the deformation of the lid of the collector being greatest at the groove. The simulation of Toshiba's model focuses more on the second which has the most common PP IGBT structure, where each sub-module has a separate upper Mo plate.

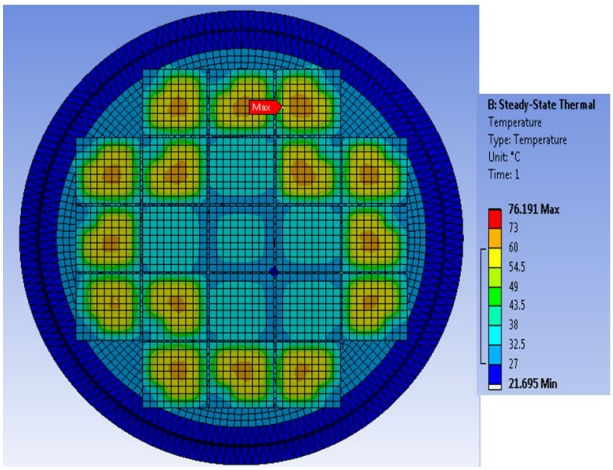

(a)

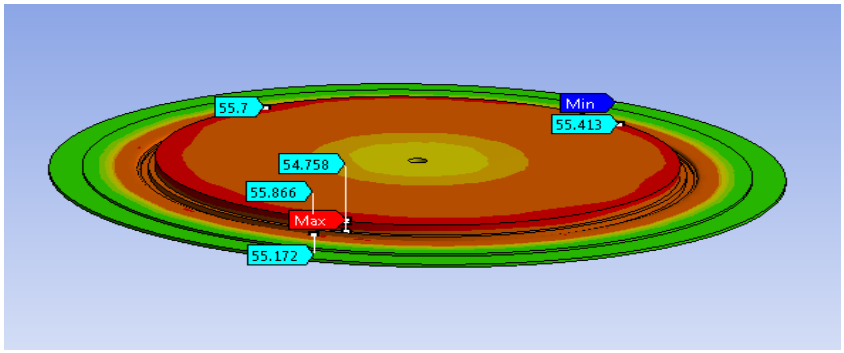

(b)

Figure A.2 (a)Temperature distribution of the chip layer (b) Deformation of collector lid

The second geometry model from Toshiba is presented in Figure A.3, it clearly shows that each chip has individual upper Mo plate.

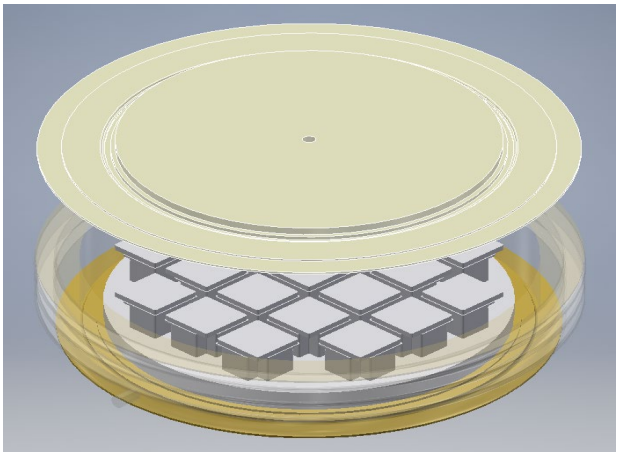

Figure A.3 Geometry model of Toshiba with individual upper Mo plate

Following the similar procedure as in chapter 3, the investigation of varying the input power dissipation is carried out.

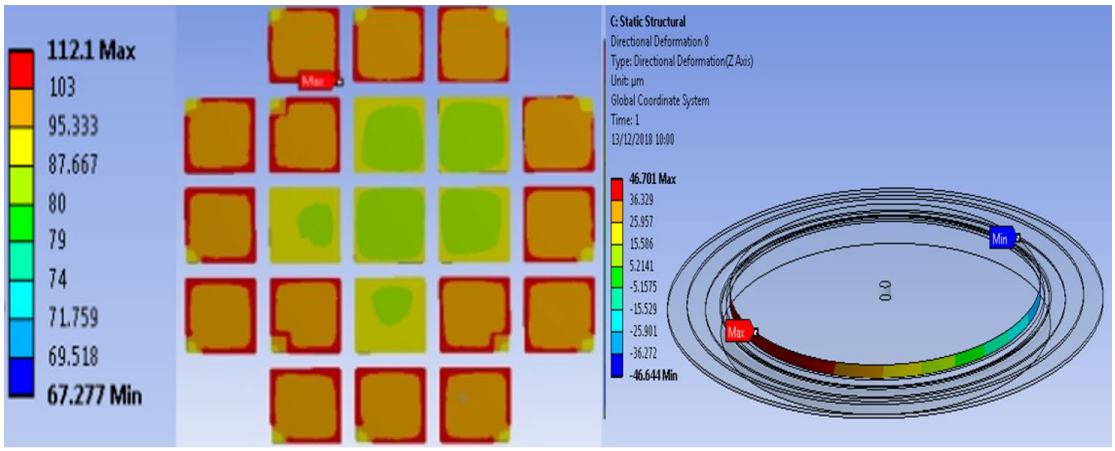

(a)

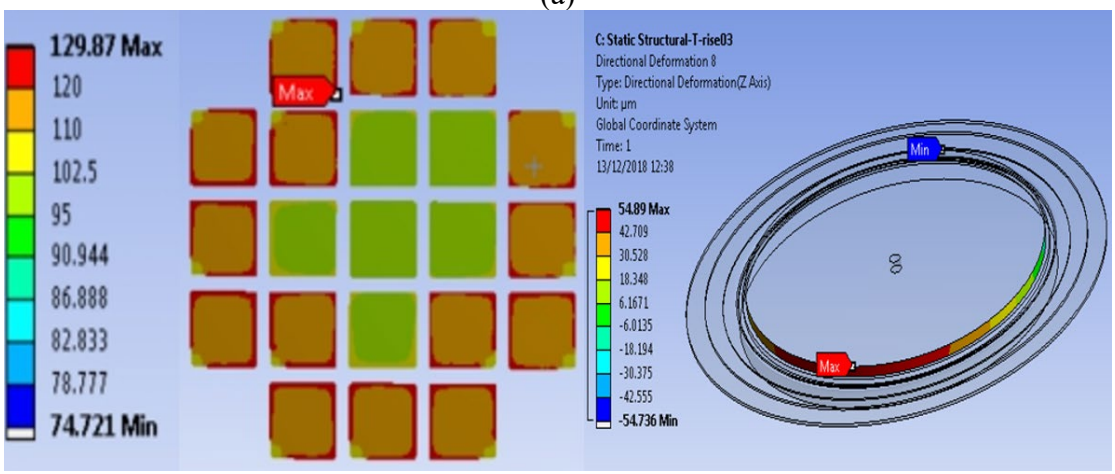

(b)

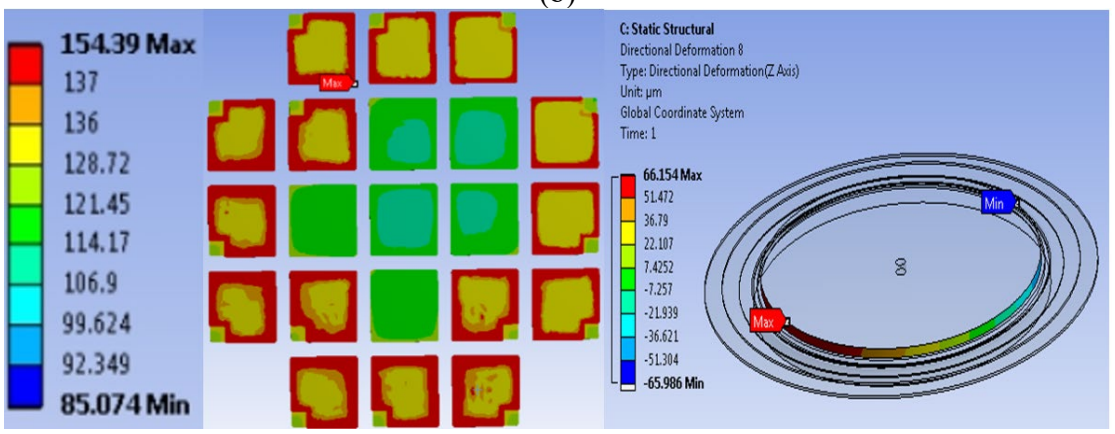

(c)

Figure A.4 Simulation results of temperature distribution across the chip surface and deformation against the temperature of the upper lid groove (a) 3000 pw/µm3 (b) 3300 pw/µm3 (c) 3600 pw/µm3

Figure A.4 shows the temperature distribution of chips on the collector side when the power dissipation of the die is set from 3000 to 3600 pw/μm3 and presents the Z-axis deformation of the lid groove according to each temperature distribution, it can be seen that the IGBT chips on the outer ring have higher temperature compared with diode chips owing to the different power loss. In addition, higher temperature trend at the edge of each chip. Figure A.5 shows the relationship between the temperature and deformation, the deformation value increase with the rise of the power loss.

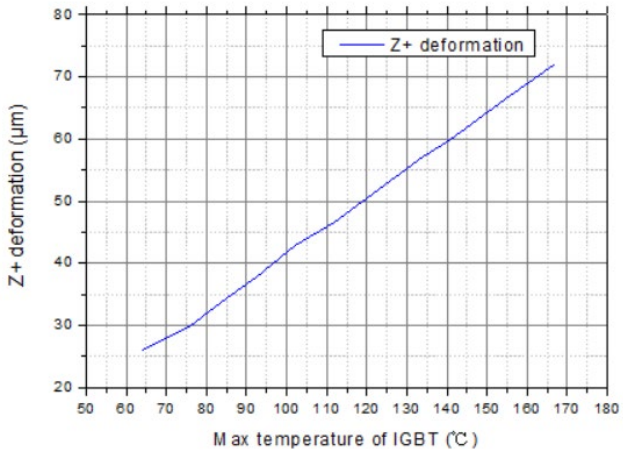

Figure A.5 Relationship between the maximum temperature of the chip surface and maximum deformation of the lid groove

Appendix B

PP IGBT clamping fixture drawing and picture

Drawing containing dimensions for the clamping fixture is presented in Figure B.1.

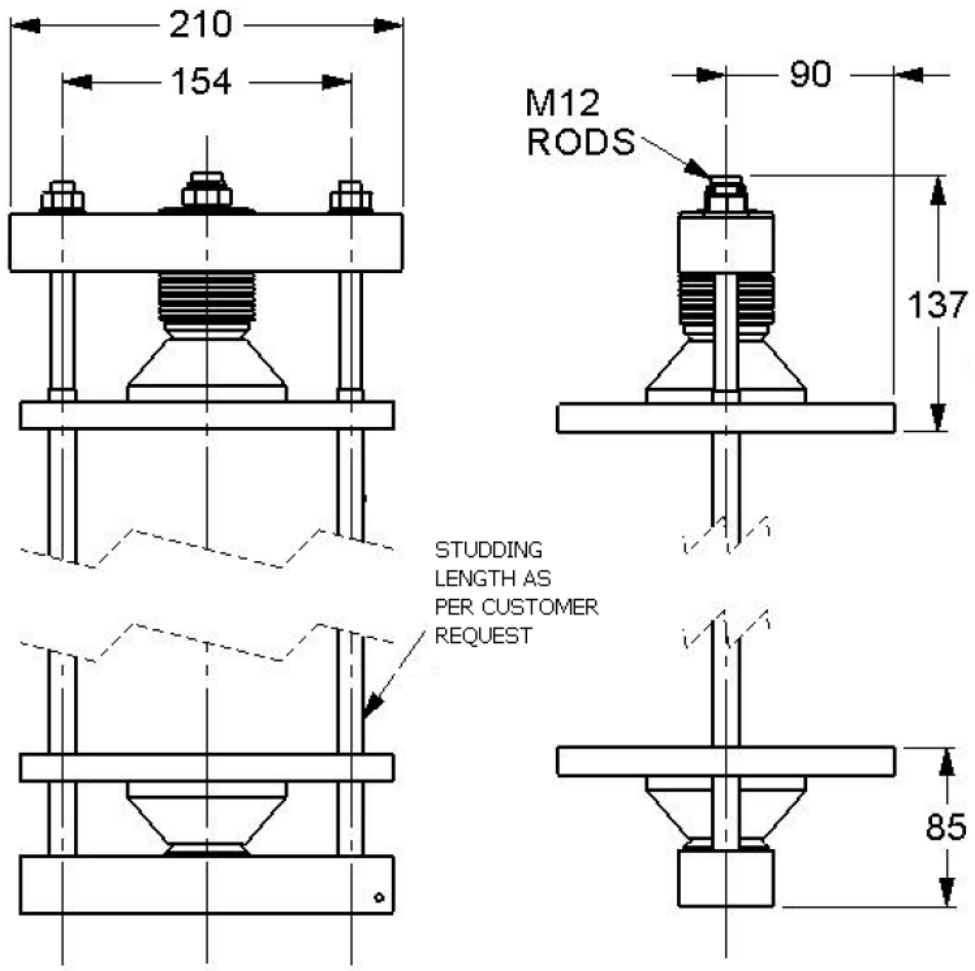

Figure B.1 Dimensions of clamping fixture

Figure B.2 shows the picture of the clamping fixture, the steel base is post-mounted for using in lab.

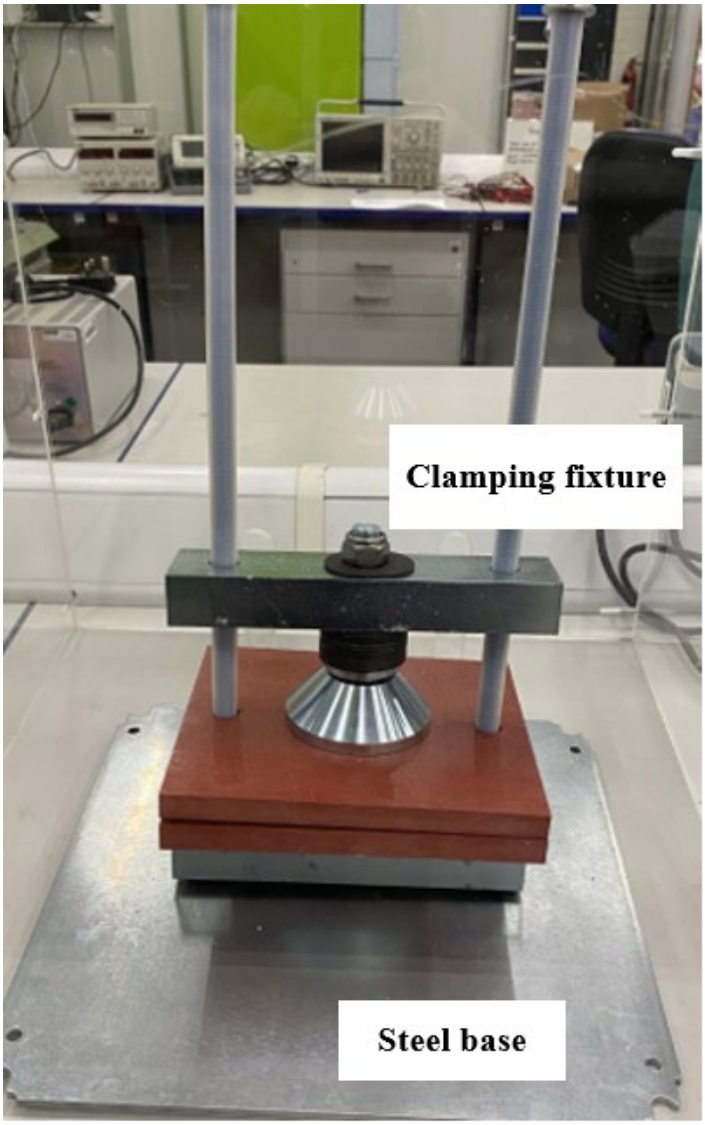

Figure B.2 Picture of clamping fixture with steel base

Appendix C

FBG based measuring system pictures

Figure C.1-2 show the detailed picture of FBG based measuring system.

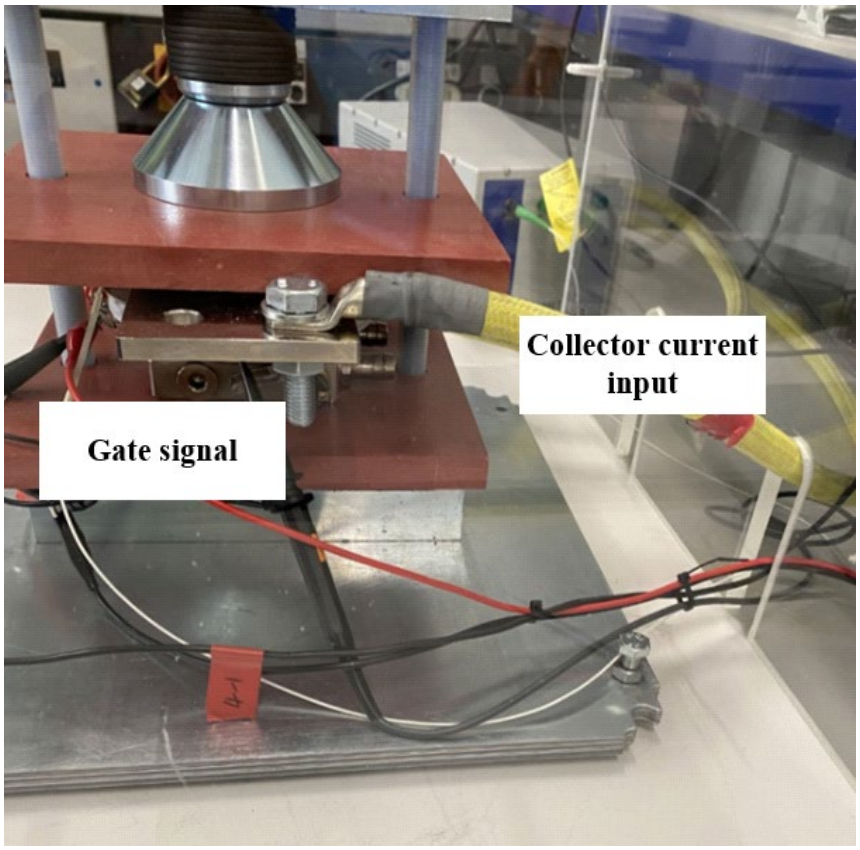

Figure C.1 Picture of FBG measurement system in left side

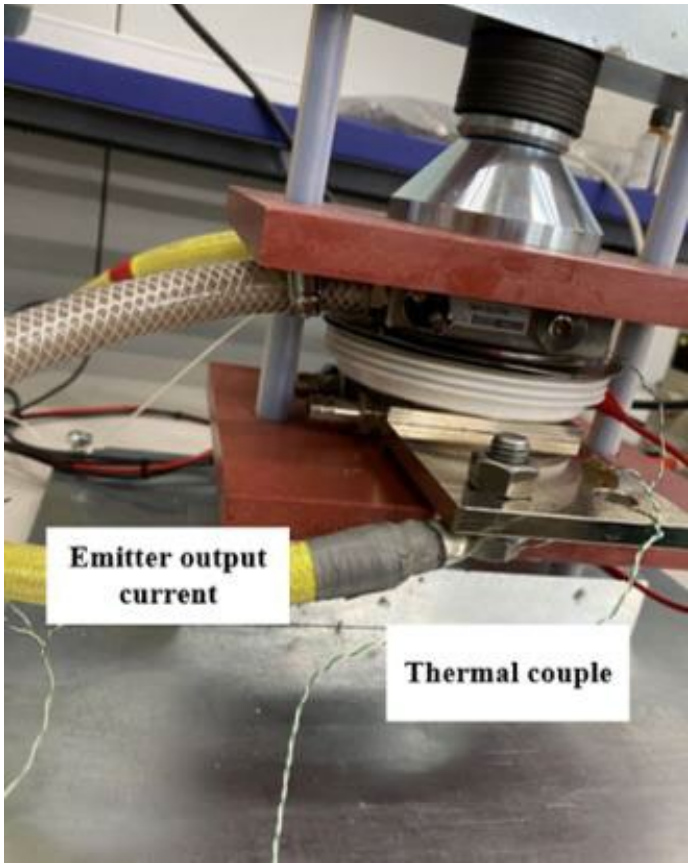

Figure C.2 Picture of FBG measurement system in right side

Appendix D

FBG sensor with 8 gratings drawing and pictures

Drawing containing dimensions for the FBG sensor is presented in Figure D.1.

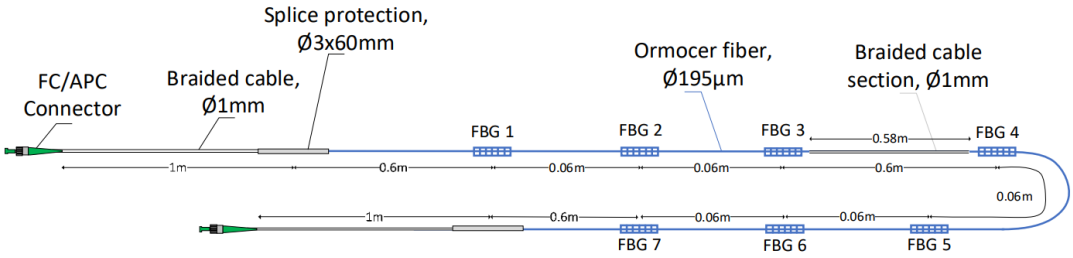

Figure B.1 Dimensions of FBG fiber sensor

Figure D.2 shows the picture of the FBG sensor.

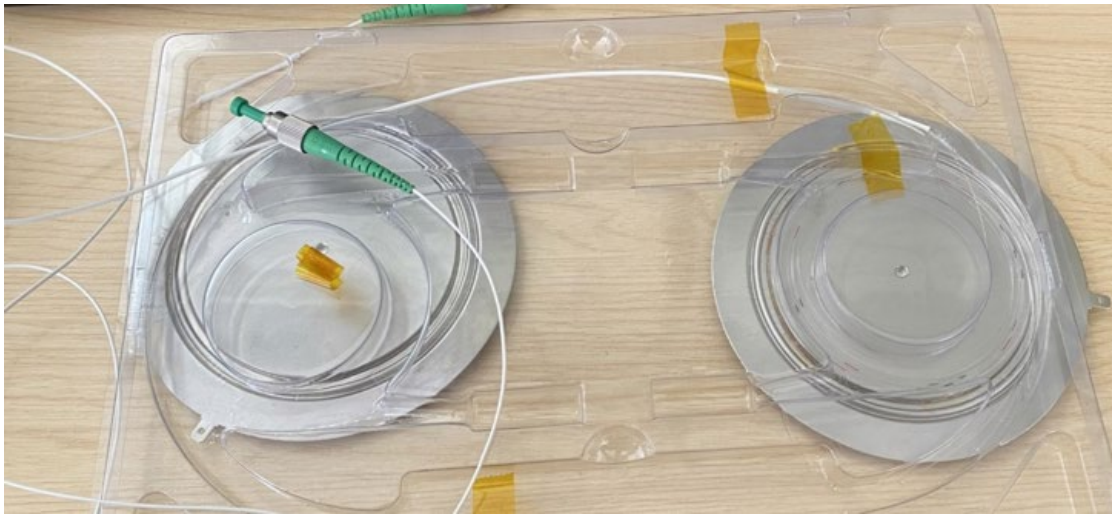

Figure D.2 Picture of FBG fiber sensor

Reference

[1] Elsam A/S, “Horns Ref Offshore Wind Farm, the world’s largest offshore wind energy project”, http://www.hornsrev.dk

[2] ABB (2021) *HVDC transmission for lower investment cost*, Available at: http://www.abb.com/cawp/GAD02181/C1256D71001E0037C12568320064F435.aspx (Accessed: 22 July 2021)

[3] "Q&A". *Western HVDC*. Archived *from the original on 22 March 2015*. Retrieved 28 March 2015.

[4] "NG ETYS 2015". *Electricity 10-year statement. National Grid plc*. Archived *from the original on 21 December 2015*. Retrieved 31 December 2015.

[5] Muneer, T., Jadraque Gago, E. and Etxebarria Berrizbeitia, S., 2022. Solar and Wind Energy Technologies. In *The Coming of Age of Solar and Wind Power* (pp. 21-103). Springer, Cham.

[6] Infineon (2021) *IGBT-modules*. Available at: https://www.infineon.com/cms/en/product/power/igbt/igbtmodules/fz500r65ke3/ (Accessed: 22 July 2021)

[7] Khomfoi, S. and Tolbert, L.M., 2011. Multilevel power converters. In *Power electronics handbook* (pp. 455-486). Butterworth-Heinemann.

[8] M. Ciappa and W. Fichtner, "Lifetime prediction of IGBT modules for traction applications," in *Reliability Physics Symposium, 2000. Proceedings. 38th Annual 2000 IEEE International*, 2000, pp. 210-216.

[9] Alassi, A., Bañales, S., Ellabban, O., Adam, G. and MacIver, C., 2019. HVDC transmission: technology review, market trends and future outlook. *Renewable and Sustainable Energy Reviews*, *112*, pp.530-554.

[10] Huang, A.Q., 2019. Power semiconductor devices for smart grid and renewable energy systems. *Power electronics in renewable energy systems and smart grid: Technology and applications*, pp.85-152.

[11] Shenai, K., 2015. The invention and demonstration of the IGBT [a look back]. *ieee Power* electronics magazine, 2(2), pp.12-16.

[12] special report: 60 years of HVDC ABB Technical Journal, ABB, Sweden (2011) ISSN: 1013-3119

[13] Simpson, R., Plumpton, A., Varley, M., Tonner, C., Taylor, P. and Dai, X., 2017. Press-pack IGBTs for HVDC and FACTs. *CSEE Journal of Power and Energy Systems*, *3*(3), pp.302-310.

[14] ABB (2021) *ABB StakPak*. Available at: https://www.hgelectronics.de/produktpartner/abb/ABB_PDFs/ABBStakPak.pdf (Accessed: 07 August 2021)

[15] Chokhawala, R., Danielsson, B. and Angquist, L., 2001, June. Power semiconductors in transmission and distribution applications. In *Proceedings of the 13th International Symposium on Power Semiconductor Devices & ICs. IPSD'01 (IEEE Cat. No. 01CH37216)* (pp. 3-10). IEEE.

[16] Volke, A. and Hornkamp, M., 2011. *IGBT modules: technologies, driver and application*. Infeneon Technologies.

[17] M. Gu *et al*., "Condition Monitoring of High Voltage IGBT Devices Based on Controllable RF Oscillations," *201931st International Symposium on Power Semiconductor Devices and ICs (ISPSD)*, Shanghai, China, 2019, pp. 355- 358.

[18] Y. Chang, Y. Chen, W. Li, and X. He, "Junction temperature extraction with maximum collector current falling rate during turn-off for press-pack IGBT modules," Trans. China Electrotechnical Soc., vol. 32, no. 12, pp. 70–78, 2017.

[19] E. Deng, Z. Zhao, P. Zhang, J. Li, and Y. Huang, "Study on the method to measure the junction-to-case thermal resistance of press-pack IGBTs," IEEE Trans. Power Electron., vol. 33, no. 5, pp. 4352–4361, May 2018.

[20] Filsecker, F., Alvarez, R. and Bernet, S., 2012. Comparison of 4.5-kV press-pack IGBTs and IGCTs for medium-voltage converters. *IEEE transactions on industrial electronics*, *60*(2), pp.440-449.

[21] IXYS (2014) IXYS application Available at: https://fhi.nl/app/uploads/sites/38/2014/01/KWx-IXYS-UK-IGBT-june14.pdf (Accessed: 07 August 2021)

[22] O. V. Thorsen and M. Dalva, "Methods of condition monitoring and fault diagnosis for induction motors," ETEP, vol. 8, no. 5, Sept./Oct. 1998.

[23] P. J. Tavner and J. Penman, Condition Monitoring of Electrical Machines: Research Studies Press, Ltd., 1987.

[24] Wei, K., Wang, W., Hu, Z. and Du, M., 2019. Condition monitoring of IGBT modules based on changes of thermal characteristics. *IEEE Access*, *7*, pp.47525-47534.

[25] Brunko, A., Holzke, W., Groke, H., Orlik, B. and Kaminski, N., 2019, September. Model-based condition monitoring of power semiconductor devices in wind turbines. In *2019 21st European Conference on Power Electronics and Applications (EPE'19 ECCE Europe)* (pp. P-1). IEEE.

[26] Schubert, M. and De Doncker, R.W., 2020. Semiconductor temperature and condition monitoring using gate-driver-integrated inverter output voltage measurement. *IEEE Transactions on Industry Applications*, *56*(3), pp.2894-2902.

[27] S. Yang, D. Xiang, A. Bryant, P. Mawby, L. Ran, and P. Tavner, "Condition monitoring for device reliability in power electronic converters: A review," *IEEE Trans. Power Electron*., vol. 25, no. 11, pp. 2734–2752, Nov. 2010.

[28] B. J. Baliga, M. S. Adler, P. V. Gray, R. P. Love, and N. Zommer, "The insulated gate rectifiifier (IGR): A new power switching device," in *Proc. Int. Electron Devices Meeting*, San Francisco, CA, USA, 1982, pp. 264–267.

[29] Zhang, Y., Deng, E., Zhao, Z., Chen, J., Zhao, Y., Guo, J. and Cui, X., 2020. Sequential V ce (T) Method for the Accurate Measurement of Junction Temperature Distribution Within Press-Pack IGBTs. *IEEE Transactions on Power Electronics*, *36*(4), pp.3735-3743.

[30] B. J. Baliga, "Evolution of MOS-bipolar power semiconductor technology," *Proc. IEEE*, vol. 76, no. 4, pp. 409–418, Apr. 1988.

[31] FUJI IGBT modules application manual," Fuji Electric Device Technology Co., Ltd.2004.

[32] T. Komiyama, Y. Chonan, J. Onuki, M. Koizumi, and T. Shigemura, "High-temperature thick Al wire bonding technology for high-power modules," *Japanese J. Appl. Phys. Part 1: Reg. Papers*, vol. 41, pp. 5030–5033, Aug. 2002

[33] M. Held, P. Jacob, G. Nicoletti, P. Scacco, and M. H. Poech, "Fast power cycling test of IGBT modules in traction application," in *Power Electronics and Drive Systems, 1997. Proceedings., 1997 International Conference on*, 1997, pp. 425-430 vol.1.

[34] L. Feller, S. Hartmann, and D. Schneider, "Lifetime analysis of solder joints in high power IGBT modules for increasing the reliability for operation at 150°C," *Microelectronics Reliability,* vol. 48, pp. 1161-1166.

[35] C. Mauro, "Selected failure mechanisms of modern power modules," *Microelectronics Reliability,* vol. 42, pp. 653-667.

[36] M. Ciappa and W. Fichtner, "Lifetime prediction of IGBT modules for traction applications," in *Reliability Physics Symposium, 2000. Proceedings. 38th Annual 2000 IEEE International*, 2000, pp. 210-216.

[37] V. Smet, F. Forest, J.-J. Huselstein, F. Richardeau, Z. Khatir, S. Lefebvre, and M. Berkani, "Ageing and failure modes of IGBT modules in high-temperature power cycling," *IEEE Transactions on Industrial Electronics,* vol. 58, pp. 4931-4941, 2011.

[38] A. Morozumi, K. Yamada, T. Miyasaka, S. Sumi, and Y. Seki, "Reliability of power cycling for IGBT power semiconductor modules," *Industry Applications, IEEE Transactions on,* vol. 39, pp. 665-671, 2003.

[39] K. Guth, F. Hille, F. Umbach, D. Siepe, J. Görlich, H. Torwesten, and R. Roth, "New assembly and interconnects beyond sintering methods," *presented at the Intelligent Motion and Power Quality (PCIM) Europe*, Nuremberg, Germany, 2010.

[40] A. Ciliox, F. Hille, F. Umbach, J. Görlich, K. Guth, D. Siepe, S. Krasel, and P. Szczupak, "New module generation for higher lifetime*," presented at the Intelligent Motion and Power Quality (PCIM) Europe,* Nuremberg, Germany, 2010.

[41] L. Dupont, Z. Khatir, S. Lefebvre, R. Meuret, B. Parmentier, and S. Bontemps, "Electrical characterizations and evaluation of thermo-mechanical stresses of a power module dedicated to high temperature applications," in *Power Electronics and Applications, 2005 European Conference on*, 2005, pp. 11 pp.-P.11.

[42] Littelfuse-IXYS UK (2021) *Expanded Product Brief*. Available at: https://www.iconopower.com/v/ixys/Ixys%20Presspack%20IGBT%20Product%20Brief%20Issue%202.pdf (Accessed: 06 August 2021)

[43] V. Smet, F. Forest, J.-J. Huselstein, F. Richardeau, Z. Khatir, S. Lefebvre, and M. Berkani, "Ageing and failure modes of IGBT modules in high-temperature power cycling," *IEEE Transactions on Industrial Electronics,* vol. 58, pp. 4931-4941, 2011.

[44] A. Morozumi, K. Yamada, T. Miyasaka, S. Sumi, and Y. Seki, "Reliability of power cycling for IGBT power semiconductor modules," *Industry Applications, IEEE Transactions on,* vol. 39, pp. 665-671, 2003.

[45] K. Guth, F. Hille, F. Umbach, D. Siepe, J. Görlich, H. Torwesten, and R. Roth, "New assembly and interconnects beyond sintering methods," *presented at the Intelligent Motion and Power Quality (PCIM) Europe*, Nuremberg, Germany, 2010.

[46] A. Ciliox, F. Hille, F. Umbach, J. Görlich, K. Guth, D. Siepe, S. Krasel, and P. Szczupak, "New module generation for higher lifetime*," presented at the Intelligent Motion and Power Quality (PCIM) Europe,* Nuremberg, Germany, 2010.

[47] L. Dupont, Z. Khatir, S. Lefebvre, R. Meuret, B. Parmentier, and S. Bontemps, "Electrical characterizations and evaluation of thermo-mechanical stresses of a power module dedicated to high temperature applications," in *Power Electronics and Applications, 2005 European Conference on*, 2005, pp. 11 pp.-P.11.

[48] L. Dupont, Z. Khatir, S. Lefebvre, and S. Bontemps, "Effects of metallization thickness of ceramic substrates on the reliability of power assemblies under high temperature cycling," *Microelectronics Reliability,* vol. 46, pp. 1766-1771.

[49] A. Morozumi, K. Yamada, T. Miyasaka, S. Sumi, and Y. Seki, "Reliability of power cycling for IGBT power semiconductor modules," *Industry Applications, IEEE Transactions on,* vol. 39, pp. 665-671, 2003.

[50] G. Mitic and G. Lefranc, "Localization of electrical-insulation and partial discharge failures of IGBT modules," *Industry Applications, IEEE Transactions on,* vol. 38, pp. 175-180, 2002.

[51] E. A. Amerasekera and F. N. Najm, *Failure Mechanisms in Semiconductor Devices, 2nd ed*, 2nd ed.: John Wiley & Sons Ltd, 1998.

[52] Golland.A & Wakeman.F "New family of 4.5kV Press-pack IGBTs", *PCIM* 2005, pp 137 – 142.

[53] F. Wakeman, J. Pitman and S. Steinhoff, "Long term short-circuit stability in Press-pack IGBTs," *2016 18th European Conference on Power Electronics and Applications (EPE'16 ECCE Europe)*, Karlsruhe, 2016, pp. 1-10.

[54] Robin Simpson, Ashley Plumpton, Michael Varley. "Press-pack IGBTs for HVDC and FACTS". *Csee Journal of power and energy systems,* vol. 3, no.3, Sep. 2017.

[55] U. Scheuermann, "Reliability challenges of automotive power electronics," *Microelectron. Rel.*, vol. 49, pp. 1319–1325, 2009

[56] ABB Switzerland Ltd, Semiconductors, IGBT and Diode chips. http://www. 5scomponents. com/ pdf/ Chip-Flyer_0409_Web.pdf. Visited: 2014-04-08

[57] T. Poller, T. Basler, M. Hernes, S. D'Arco, and J. Lutz, "Mechanical analysis of press-pack IGBTs," *Microelectron. Rel.*, vol. 52, pp. 2397– 2402, Sep./Oct. 2012.

[58] Chen H, Cao W, Bordignon P, et al. Design and testing of the World's first single-level press-pack IGBT based submodule for MMC VSC HVDC applications[C]//*Energy Conversion Congress and Exposition (ECCE),* 2015 IEEE.

[59] T. Poller, J. Lutz, S. D'Arco and M. Hernes, "Determination of the thermal and electrical contact resistance in press-pack IGBTs," *2013 15th European Conference on Power Electronics and Applications (EPE),* Lille, 2013, pp. 1-9.

[60] Lukas Tinschert, Atle Rygg Årdal, Tilo Poller, Marco Bohlländer, Magnar Hernes, Josef Lutz, Possible failure modes in Press-Pack IGBTs*, Microelectronics Reliability,* Volume 55, Issue 6, 2015, Pages 903-911,

[61] E. Deng, Z. Zhao, Z. Lin, R. Han and Y. Huang, "Influence of Temperature on the Pressure Distribution Within Press Pack IGBTs," in *IEEE Transactions on Power Electronics*, vol. 33, no. 7, pp. 6048-6059, July 2018

[62] Varley, Michael, et al. "Thermo-Mechanical Optimisation of Press-Pack IGBT Packaging Using Finite Element Method Simulation." *PCIM Europe 2017; International Exhibition and Conference for Power Electronics, Intelligent Motion, Renewable Energy and Energy Management; Proceedings of*. VDE, 2017.

[63] H. T. Grimmelius, P. P. Meiler, and L. M. M. Maas et al., "Three state-of-the-art methods for condition monitoring," IEEE Trans. Ind. Electron., vol. 46, pp. 407–416, 1999

[64] S. Yang, A. Bryant, P. Mawby, D. Xiang, L. Ran, and P. Tavner, "An industry-based survey of reliability in power electronic converters," *IEEE Trans. Ind. Appl.*, vol. 47, no. 3, pp. 1441–1451, May/Jun. 2011.

[65] C. Bengtsson, "Status and trends in transformer monitoring," IEEE Trans. Power Delivery, vol. 11, pp. 1379–1384, July 1996.

[66] Xinling Tang, Yan Pan, Peng Zhang, Zhibin Zhao, Xiang Cui. A new method to

extract stray inductance in IGBTs' Dynamic test bench [C]. *The 2'nd International Conference on HVDC*, Shanghai, China, 2016.

[67] *Ø. Frank, "Power Cycle Testing of Press-Pack IGBT Chips", 2014*

[68] S. Gunturi and D. Schneider, "On the operation of a press pack IGBT module under short circuit conditions," in *IEEE Transactions on Advanced Packaging*, vol. 29, no. 3, pp. 433-440, Aug. 2006.

[69] Cengelci, E., Sulistijo, S.U., Woo, B.O., Enjeti, P., Teoderescu, R. and Blaabjerg, F., 1999. A new medium-voltage PWM inverter topology for adjustable-speed drives. *IEEE Transactions on Industry Applications*, *35*(3), pp.628-637.

[70] Oh H, Han B, McCluskey P, et al. Physics-of-failure, condition monitoring, and prognostics of insulated gate bipolar transistor modules: A review[J]. *IEEE Transactions on power electronics,* 2015, 30(5): 2413-2426.

[71] M. Gu *et al*., "Condition Monitoring of High Voltage IGBT Devices Based on Controllable RF Oscillations," *201931st International Symposium on Power Semiconductor Devices and ICs (ISPSD)*, Shanghai, China, 2019, pp. 355- 358.

[72] H. Li, R. Yao, W. Lai, H. Ren and J. Li, "Modeling and Analysis on Overall Fatigue Failure Evolution of Press-Pack IGBT Device," *in IEEE Transactions on Electron Devices*, vol. 66, no. 3, pp. 1435-1443, March 2019.

[73] Y. Chang, Y. Chen, W. Li, and X. He, "Junction temperature extraction with maximum collector current falling rate during turn-off for press-pack IGBT modules," Trans. China Electrotechnical Soc., vol. 32, no. 12, pp. 70–78, 2017.

[74] E. Deng, Z. Zhao, P. Zhang, J. Li, and Y. Huang, "Study on the method to measure the junction-to-case thermal resistance of press-pack IGBTs," IEEE Trans. Power Electron., vol. 33, no. 5, pp. 4352–4361, May 2018.

[75] G. Dong et al., "Optimization of the thermal contact resistance model for studying thermal properties of press pack IGBT," Power Electron., vol. 52, no. 8, pp. 34–37, 2018.

[76] Zhang, Y., Deng, E., Zhao, Z., Chen, J., Zhao, Y., Guo, J. and Cui, X., 2020. Sequential V ce (T) Method for the Accurate Measurement of Junction Temperature Distribution Within Press-Pack IGBTs. *IEEE Transactions on Power Electronics*, *36*(4), pp.3735-3743.

[77] TUNÇALP, K. and TAŞKIN, S., A safety test for traveller bus using strain gauges.

[78] Strain gauge measurement – National Instruments application note 078

[79] Tennyson, R.C., Banthia, N., Rivera, E., Huffman, S. and Sturrock, I., 2007. Monitoring structures using long gauge length fibre optic sensors. *Canadian Journal of Civil Engineering,* 34(3), pp.422-429.

[80] Dufour, M.L., Lamouche, G., Detalle, V., Gauthier, B. and Sammut, P., 2005. Low-coherence interferometry–an advanced technique for optical metrology in industry. *Insight-Non-Destructive Testing and Condition Monitoring*, *47*(4), pp.216-219.

[81] Rodrigues, C., Inaudi, D. and Glišić, B., 2013. Long-gauge fibre optic sensors: performance comparison and applications. *International Journal of Lifecycle Performance Engineering 4*, *1*(3), pp.209-233.

[82] Xiao, G.Z., Adnet, A., Zhang, Z., Sun, F.G. and Grover, C.P., 2005. Monitoring changes in the refractive index of gases by means of a fiber optic Fabry-Perot interferometer sensor. *Sensors and Actuators A: Physical,* 118(2), pp.177-182.

[83] Jiang, M. and Gerhard, E., 2001. A simple strain sensor using a thin film as a low-finesse fiber-optic Fabry–Perot interferometer. *Sensors and Actuators A: Physical*, *88*(1), pp.41-46.

[84] Aebersold, J., Walsh, K., Crain, M., Voor, M., Martin, M., Hnat, W., Lin, J., Jackson, D., and Naber, J.: Design, modeling, fabrication and testing of a MEMS capacitive bending strain sensor, *J. Phys. Conf. Ser.,* 34, 124–129, 2006.

[85] Aebersold, J., Walsh, K., Crain, M., Voor, M., Martin, M., Hnat, W., Lin, J., Jackson, D. and Naber, J., 2006, April. Design, modeling, fabrication and testing of a MEMS capacitive bending strain sensor. In *Journal of Physics: Conference Series* (Vol. 34, No. 1, p. 021). IOP Publishing.

[86] Tsouti, V., Mitrakos, V., Broutas, P. and Chatzandroulis, S., 2016. Modeling and development of a flexible carbon black-based capacitive strain sensor. *IEEE Sensors Journal*, *16*(9), pp.3059-3067.

[87] Zeiser, R., Fellner, T. and Wilde, J., 2014. Capacitive strain gauges on flexible polymer substrates for wireless, intelligent systems. *Journal of Sensors and Sensor Systems*, *3*(1), pp.77-86.

[88] S. M. Avery and R. D. Lorenz, "In Situ Measurement of Wire-Bond Strain in Electrically Active Power Semiconductors," *in IEEE Transactions on Industry Applications,* vol. 49, no. 2, pp. 973-981, March-April 2013.

[89] Yang, L., Xie, X., Zhu, L., Wu, S. and Wang, Y., 2014. Review of electronic speckle pattern interferometry (ESPI) for three-dimensional displacement measurement. *Chinese Journal of Mechanical Engineering*, *27*(1), pp.1-13.

[90] P. Aswendt, C. Schmidt, D. Zielke, and S. Schubert, "ESPI solution for non-contacting MEMS-on-wafer testing," Opt. Lasers Eng., vol. 40, no. 5/6, pp. 501–515, Nov./Dec. 2003.

[91] Y. Gao and J. Wang, "Testing failure of solder-joints by ESPI on board-level surface mount devices," in Proc. ICEPT-HDP, Aug. 2009, pp. 1256–1259.

[92] D. Pustan, M. Lapisa, M. Rieber, E. Zukowski, and J. Wilde, "Combination of modern test methods for thermo-mechanical deformation analysis in flip-chip-assemblies," in Proc. Electron. Syst. Integr. Technol. Conf., Sep. 2006, vol. 2, pp. 1103–1107

[93] B. Donohoe, D. Geraghty, G. E. O'Donnell and R. Stoney, "Packaging Considerations for a Surface Acoustic Wave Strain Sensor," *in IEEE Sensors Journal,* vol. 12, no. 5, pp. 922-925, May 2012.

[94] R. Stoney, D. Geraghty and G. E. O'Donnell, "Characterization of Differentially Measured Strain Using Passive Wireless Surface Acoustic Wave (SAW) Strain Sensors," in IEEE Sensors Journal, vol. 14, no. 3, pp. 722-728, March 2014, doi: 10.1109/JSEN.2013.2285722.

[95] Xu, H., Dong, S., Xuan, W., Farooq, U., Huang, S., Li, M., Wu, T., Jin, H., Wang, X. and Luo, J., 2018. Flexible surface acoustic wave strain sensor based on single crystalline LiNbO3 thin film. Applied Physics Letters, 112(9), p.093502.

[96] Q. Li et al., "Highly Sensitive Surface Acoustic Wave Flexible Strain Sensor," in IEEE Electron Device Letters, vol. 40, no. 6, pp. 961-964, June 2019, doi: 10.1109/LED.2019.2909320.

[97] Surface Preperation for Strain Gauge Bonding: Application Note B-129-8:2005 Vishay Precision Group.

[98] A. D. Kersey, M. A. Davis, H. J. Patrick et al., "Fiber grating sensors," *Journal of Lightwave Technology,* vol. 15, no. 8, pp. 1442–1462, 1997.

[99] G. Meltz, W. W. Morey, and W. H. Glenn, “Formation of Bragg gratings in optical fifibers by a transverse holographic method,” *Opt. Lett.,* vol. 14, p. 823, 1989.

[100] R. Kashyap, “Photosensitive optical fifibers: Devices and applications,” *Optic. Fiber Technol.,* vol. 1, p. 17, 1994.

[101] W. W. Morey, G. Meltz, and W. H. Glenn, “Fiber Bragg grating sensors,” in *Proc. SPIE Fiber Optic & Laser Sensors VII,* 1989, vol. 1169, p. 98.

[102] Xiong, Y., Cheng, X., Shen, Z.J., Mi, C., Wu, H. and Garg, V.K., 2008. Prognostic and warning system for power-electronic modules in electric, hybrid electric, and fuel-cell vehicles. *IEEE Transactions on Industrial Electronics*, *55*(6), pp.2268-2276.

[103] Lu, H., Bailey, C. and Yin, C., 2009. Design for reliability of power electronics modules. *Microelectronics reliability*, *49*(9-11), pp.1250-1255.

[104] Mishra, S., Pecht, M. and Goodman, D.L., 2002, April. In-situ sensors for product reliability monitoring. In *Design, Test, Integration, and Packaging of MEMS/MOEMS 2002* (Vol. 4755, pp. 10-19). SPIE.

[105] Pecht, M.G., 2010. A prognostics and health management roadmap for information and electronics-rich systems. *IEICE ESS Fundamentals Review*, *3*(4), pp.4_25-4_32.

[106] Pecht, M., Tuchband, B., Vichare, N. and Ying, Q.J., 2007, April. Prognostics and health monitoring of electronics. In *2007 International Conference on Thermal, Mechanical and Multi-Physics Simulation Experiments in Microelectronics and Micro-Systems. EuroSime 2007* (pp. 1-8). ieee.

[107] Lall, P., Hande, M., Bhat, C., More, V., Vaidya, R. and Suhling, J., 2008, May. Algorithms for prognostication of prior damage and residual life in lead-free electronics subjected to thermo-mechanical loads. In *2008 11th Intersociety Conference on Thermal and Thermomechanical Phenomena in Electronic Systems* (pp. 638-651). IEEE.

[108] Vachtsevanos, G.J. and Vachtsevanos, G.J., 2006. *Intelligent fault diagnosis and prognosis for engineering systems* (Vol. 456). Hoboken: Wiley.

[109] Bozhko, S.V., Blasco-Gimenez, R., Li, R., Clare, J.C. and Asher, G.M., 2007.

Control of offshore DFIG-based wind farm grid with line-commutated HVDC connection. *IEEE Transactions on Energy Conversion*, *22*(1), pp.71-78.

[110] Hottinger Bruel & Kjaer UK Ltd, 9999658483 quote, 2021.

[111] U.Scheuermann and R.Schmidt, "Investigations on the VCE(T)-Method to Determine the Junction Temperature by Using the Chip Itself as Sensor," *presented at the Intelligent Motion and Power Quality (PCIM) Europe,* Nuremberg, Germany, 2009.

[112] Z. Khatir and S. Lefebvre, "Boundary element analysis of thermal fatigue effects on high power IGBT modules," *Microelectronics Reliability,* vol. 44, pp. 929- 938, 2004.

[113] Farokhzad, "Method for early failure recognition in power semiconductor modules."

[114] I. Ka *et al*., "Instrumented chip dedicated to semiconductor temperature measurements in power electronic converters," *2016 IEEE Energy Conversion Congress and Exposition (ECCE)*, Milwaukee, WI, 2016, pp. 1-8, doi: 10.1109/ECCE.2016.7855208.

[115] E. R. Motto and J. F. Donlon, "IGBT module with user accessible on-chip current and temperature sensors," *2012 Twenty-Seventh Annual IEEE Applied Power Electronics Conference and Exposition (APEC)*, Orlando, FL, 2012, pp. 176-181, doi: 10.1109/APEC.2012.6165816.

[116] T. Poller, S. D'Arco, M. Hernes, A. Rygg Ardal, J. Lutz, Influence of the clamping pressure on the electrical, thermal and mechanical behaviour of press-pack IGBTs, *Microelectronics Reliability,* Volume 53, Issues 9–11, 2013

[117] Held, M., Jacob, P., Nicoletti, G., Scacco, P. and Poech, M.H., 1997, May. Fast power cycling test of IGBT modules in traction application. In *Proceedings of second international conference on power electronics and drive systems* (Vol. 1, pp. 425-430). IEEE.

[118] Pizano-Martinez, A., Fuerte-Esquivel, C.R., Ambriz-Pérez, H. and Acha, E., 2007. Modeling of VSC-based HVDC systems for a Newton-Raphson OPF algorithm. *IEEE Transactions on Power Systems*, *22*(4), pp.1794-1803.

[119] Brown, D.W., Abbas, M., Ginart, A., Ali, I.N., Kalgren, P.W. and Vachtsevanos, G.J., 2011. Turn-off time as an early indicator of insulated gate bipolar transistor

latch-up. *IEEE Transactions on Power Electronics*, *27*(2), pp.479-489.

[120] Entso-e (2022) Scheduled Commercial Exchanges, available at: https://transparency.entsoe.eu/dashboard/show (Accessed: 17 July 2022)